PROJECT #24: NEXT GENERATION OF ROBUST AND FIRE-RESILIENT LIGHT GAUGE STEEL SYSTEMS FOR MID-RISE BUILDINGS

SUB-PROJECT 1: DESIGN FOR RESISTING PROGRESSIVE COLLAPSE FOR MID-RISE LIGHT GAUGE STEEL BUILDINGS

FINAL REPORT

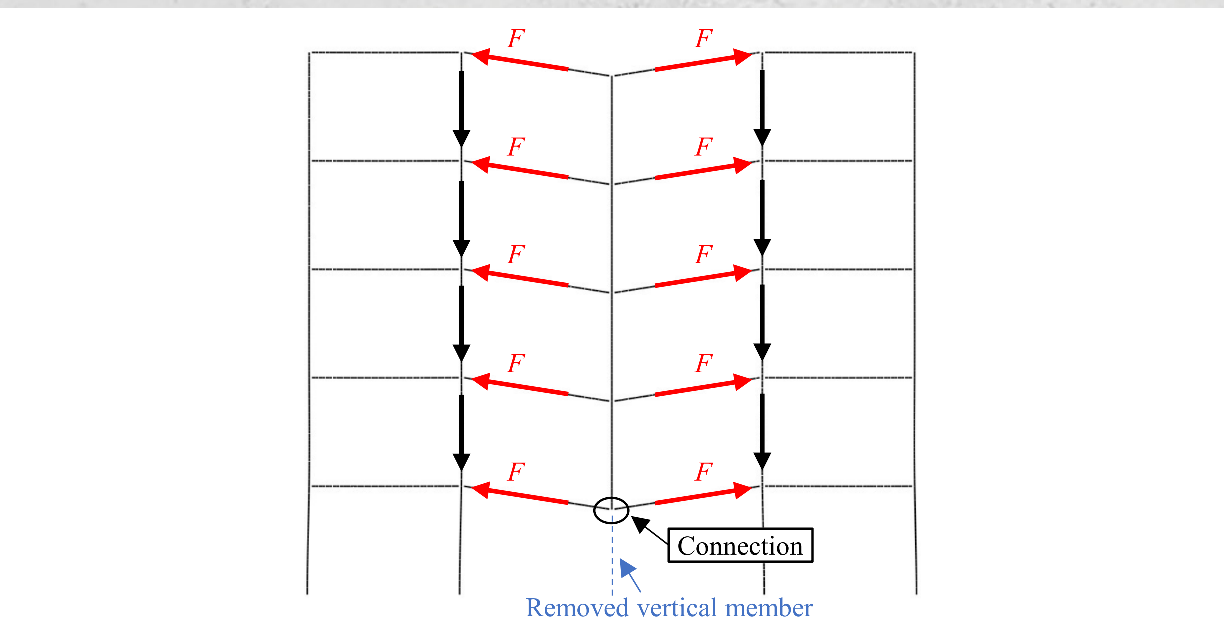

Australian Government
Department of Industry, Science and Resources
Cooperative Research Centres Program

CONTENTS

LIST OF TABLES

LIST OF FIGURES

CONFIDENTIAL:	☐ Yes X No
Author/s of this report:	Jingsheng Zhou, Huu-Tai Thai, Tuan Ngo
Date of this report:	09/09/2025
Project completion date:	30/06/2025
Program Leader reviewer:	Tuan Ngo
Project title:	**Project #24: Next Generation of Robust and Fire-resilient Light Gauge Steel Systems for Mid-Rise Buildings** **Sub-project 1 – Design for resisting progressive collapse for mid-rise light gauge steel buildings**
Project duration:	3 years
Partners:	• BlueScope • NASH National Association of Steel Framed Housing • The University of Melbourne
Project team members:	• The University of Melbourne: Prof. Tai Thai, Prof. Tuan Ngo, Dr. Jingsheng Zhou, Mrs. Lalita Lama, Mr. Tattukolla Kiran • BlueScope: Trevor Clayton, Sylvia Weber • NASH: Ken Watson
Ethics approval details (if relevant)	Not applicable

1. EXECUTIVE SUMMARY

Building collapses result in catastrophic losses of both human lives and economics and are often characterised by the propagation of initial local failures triggered by extreme or abnormal events. As the increasing frequency of extreme events and number of tall buildings, it is important to design the building to prevent progressive collapse. Given the globally increasing number of mid-rise light gauge steel (LGS) buildings, detailed design provisions for the building to increase its robustness, i.e. enhance the building strength to prevent progressive collapse, are particularly important.

The connection in mid-rise LGS building plays an important role in the load redistribution after several vertical members removal, e.g. stud wall in the building. The traditional connections are designed to resist shear and bending moment, thereby losing the resistance in tensile load. As appreciable tensile load is induced after stud wall removal, it is important to enhance the robustness of connections, i.e. the tensile resistance of connection, to prevent the premature damage that could lead to progressive collapse.

This project is working on the solution to solve above-mentioned problems, specifically, by increasing the robustness of both the connection and mid-rise LGS building. The connection behaviour was investigated experimentally, numerically and theoretically. A series of experiments were conducted to assess the robustness performance of both traditional (connections with clip angle assembled by self-drilling screws) and newly proposed connection configurations. Based on the test results, a new structural component, bottom plate, was introduced to connect the bottom flanges of adjacent joists. This element was found to significantly improve the tensile resistance and overall robustness of the connections in mid-rise LGS buildings. Finite element (FE) simulations were then performed to gain deeper insight into structural behaviours that are not observed during experiments. These simulations were based on a proposed simplified FE modelling approach designed to accurately represent the response of screws under both tension and shear loading. Additionally, a comprehensive parametric study to identify key factors influencing connection performance, thereby providing design optimisation strategies. Last, a theoretical/mechanical model was proposed to calculate the design robustness (tensile force resistance) of the new proposed connection. The model is suitable for both concentrated and distributed loads and can be conveniently implemented using hand calculations, providing practical benefits for engineering design.

The robustness of the entire building system was also investigated through numerical simulation and theoretical analysis. An 8-storey archetype mid-rise LGS building was first designed, considering vertical gravity and wind (leeward) loads. The building consists of eight stories, each comprising ten rooms connected by a central corridor. Numerical analysis of the archetype building was then performed under four stud wall removal cases, in accordance with the National Construction Code (NCC). Due to the complex configuration of the archetype building, a simplified FE model was developed to reduce computational costs while maintaining accuracy. This model incorporated simplified simulation methods for all connection types and structural members commonly used in mid-rise LGS buildings, as well as an appropriate damping ratio to simulate dynamic effects. The simulation results showed that the removal of a stud wall at the ledger can result in significant load transfer to the adjacent remaining studs. Additionally, the influence of the floor system and load-bearing walls on overall building robustness was examined. The findings suggested that while the floor system has a minor effect, while the presence of bearing walls increased the structural robustness. Based on the FE results, a theoretical framework was proposed to evaluate critical parameters including the dynamic affected area, dynamic increase factor, and the revised tributary area after stud wall removal.

Project #24: Sub-project 1 – Design for resisting progressive collapse for mid-rise light gauge steel buildings

The main outcomes of this project are summarised herein:

- The strength of the ledge-joist connection, specifically the screwed clip angle connection, was examined through tests on nine cold-formed steel ledger-joist connections. The parametric study was further conducted to investigate the influencing factors on the connection strength, using finite element (FE) simulations based on the validated model.
- A simplified FE simulation method was proposed to streamline the modelling of screws, reducing computational complexity.
- A new connection was introduced to enhance connection robustness. Its performance was evaluated using six sub-assembly specimens. Based on the experimental findings, a bottom plate was proposed as a new element for joist-to-joist connections to enhance tying force, termed the joist-to-joist bottom plate connection (JBPC).
- A hand calculation method was developed to determine the tying force of buildings, incorporating the newly proposed connection.
- The overall robustness of the building was assessed using a simplified FE model of a newly designed archetype load-bearing wall LGS building. Four distinct stud wall removal scenarios were analysed, and dynamic increase factors (DIFs) were proposed for each scenario with varying removal times.
- Based on the numerical analyses of the building, a hand calculation method was established for designing mid-rise load-bearing wall LGS buildings to resist progressive collapse.

.

2. PROJECT OVERVIEW

2.1 Introduction

LGS offers significant advantages over other construction materials, including high strength-to-weight ratio, prefabrication capability, faster construction times, non-combustibility, and resistance to rotting, shrinking, warping, and termite damage. However, the early planning phase for LGS structures lacks a clear understanding of the necessary tools and inputs required to establish LGS as a viable structural alternative to other conventional systems, particularly in mid-rise building applications. The key industry challenges involve addressing the barriers hindering the adoption of LGS in the mid-rise building market. To facilitate wider implementation, this project aims to develop a systematic design method to enhance the robustness of LGS mid-rise buildings.

2.2 Project Objectives and Scope

The project focuses on the robustness design of LGS mid-rise buildings. Commonly used robustness design approaches include the Specific Local Resistance (SLR) method, the Collapse Isolation (CI) method, the tying force (TF) method, and the alternate path (AP) method. The SLR method requires designing key or critical members to resist specific loads, such as blast or vehicle impact, thereby reducing the likelihood of the initial damage. The SLR method involves designing key or critical structural members to withstand specific loads, such as blasts or vehicle impacts, thereby minimising the likelihood of initial failure. The CI method aims to segment the building into independent parts to prevent progressive collapse when local failures exceed those anticipated in standard design provisions. This approach is particularly useful when the extent of initial damage is greater than what is typically accounted for in conventional design. Both the SLR and CI methods require customised designs for the specific purpose and size of a building, leading to a less universally applicable, whereby they are not the primary focus of this project.

Instead, this project focuses on the robustness of component and building, which are investigated through TF method and the AP method, respectively, as they have the potential to be widely implemented across various LGS mid-rise buildings. These methods focus on ensuring load redistribution and structural continuity after an initial failure, enhancing the overall robustness and resilience of LGS structures.

The TF method is defined as a part of AP method, which demonstrates the ability of the structure to bridge over loss of any member. Generally, traditional connections in mid-rise LGS buildings, screwed clip angle connection, are designed to resist appreciable shear forces (Ayhan and Schafer, 2019, Castaneda and Peterman, 2021) and bending moment (Lim and Nethercot, 2004, Zhang et al., 2016). The inadequate tensile force resistance for the screwed clip angle connection may lead to premature failure before transferring all loads to adjacent vertical members. It is evidenced by the linear elastic analysis for a three-story LGS structure (Bae et al., 2008). The analysis pointed out that the membrane (tension) force developed by catenary action after stud removal was more than five times higher than the design tying force of connection between two horizontal members. Therefore, it is essential to evaluate the capability of traditional ledger-to-joist connections in resisting significant horizontal tensile forces. Additionally, since no efficient structural element currently exists between adjacent bays to provide adequate horizontal tying force, introducing a new connection capable of sustaining the required tying force is necessary to resist the substantial membrane forces effectively.

The AP method, featuring advantages of threat independent and flexibility in implementation, is incorporated in current design provisions, which requires that the building be capable of bridging over a missing structural member, with the resulting extent of damage being localised. The AP method is commonly performed by advanced numerical method to capture the complex three-dimensional structural behaviour. Moreover, design provisions, GSA (2013a) and DoD (2016), recommended to employing hand calculations or spreadsheets for load-bearing wall buildings.

Moreover, most of the published research focuses on framed buildings and hot-rolled steel or composite materials, with LGS load-bearing wall buildings being studied only in Bae et al. (2008). However, Bae et al. (2008) is limited to a case study of a low-rise two-story building, and no design provisions are proposed. Therefore, the study also presents a comprehensive numerical analysis of mid-rise LGS load-bearing wall buildings under initial stud wall removal cases and proposes a hand calculation design approach for resisting progressive collapse.

In conclusion, this study has been carried out with the following objectives:

- Design and conduct tests on screwed clip angle connections subjected to either shear or tension to evaluate their structural response under gravity and membrane forces, respectively.
- Design and conduct tests on a newly proposed connection between two bays to investigate the effectiveness of two novel structural elements in increasing the tying force.
- Develop an FE modelling approach to accurately and efficiently simulate screws under both tension and shear, considering their widespread use in LGS buildings.
- Develop FE models for the tested screwed clip angle connections and the proposed new connection, followed by a parametric study to identify key influencing factors affecting their load resistance.
- Conduct FE modelling of a new proposed archetype mid-rise LGS building under four stud wall removal scenarios and analyse the effects of stud wall removal time on the dynamic effects.
- Propose design methods for calculating the tying force of the newly introduced connection and establish guidelines for redesigning mid-rise LGS buildings to enhance their resistance to progressive collapse.

2.3 Outline Project

Chapter 3 presents an in-depth study on the robustness of screwed clip angle connections under different loading conditions, using experimental and numerical methods. Three configurations are tested under tension and six under shear, revealing the connection's failure mechanisms and ductility limits. A simplified FE modelling method is proposed and validated for screws, significantly reducing computational effort while maintaining accuracy. This modelling approach becomes a critical tool used in the subsequent chapters.

Chapter 4 details the robustness of connection between adjacent bays, i.e. a newly proposed connection, through experimental and numerical studies. A new connection is proposed and studied through six sub-assembly tests involving combinations of stiffeners and bottom plates. The simplified FE model developed in Chapter 3 is adapted to simulate the response of the new connection. A parametric study is then conducted using a validated FE model to assess the factors affecting the ductility and resistance of the proposed connection.

Chapter 5 integrates the findings from both Chapter 3 and Chapter 4 into a full building-scale analysis. An eight-storey mid-rise LGS load-bearing wall building is designed as an archetype. The dynamic response of the building is assessed under four stud wall removal scenarios based on the National Construction Code (NCC). The proposed connections and modelling approaches from the earlier chapters are implemented within the FE model to assess their contribution to building robustness.

Chapter 6 presents the design methodology for the newly proposed connection introduced in Chapter 4 and outlines an approach for calculating force redistribution following stud wall removal scenarios discussed in Chapter 5. Design examples are provided for both methods to illustrate their practical application and integration into structural design practice.

3. SCREWED CLIP ANGLE CONNECTION

3.1 Introduction

The clip angle connection is widely used in mid-rise LGS building to connect two structural members, e.g. roof-purlin connections in roof systems, as well as joist-ledger and wall stud-ledger connections in floor systems. In roof systems, the connections are subjected to the uplifting loads leaded by wind loads. i.e. tension loads. Moreover, appreciable tensile loads are introduced after the sudden removal the stud walls. The vertical loads above the removed studs are redistributed through catenary action along the direction of horizontal members; the connections along such load transferring path are subjected to significant tension forces, including the clip angles connections in joist-ledger and wall stud-ledger connections. In contrast, the vertical loads normally applied to joists are transferred to wall studs via shear forces acting through the joist-ledger and wall stud-ledger connections.

Due to the advantages of ease of penetration through thin materials, self-drilling screws are commonly used to connect the clip angle and other structural members. Therefore, this section presents a comprehensive study on clip angle connections assembled using self-drilling screws. The connection behaviour under both tensile and shear loads is investigated through experimental testing and numerical simulations. A total of nine connections were tested, including three under tensile loading and six under shear loading. The connection behaviour is also captured by the numerical simulation with a proposed FE modelling method to simplify the efforts of model build and reduce the computational cost. A parametric study is then conducted to investigate the key factors influencing the connection response. The following sections provide a detailed discussion of the study.

3.2 Experimental investigations

Test specimens and setup

The ledger-to-joist screwed clip angle connections were tested under either tension or shear, as shown in Figure 1. The T-shaped specimen, Figure 1(a), were designed to study the tensile response of connections. The lipped C-channel was inserted into the unlipped C-channel, assembled through a clip angle. The short leg and long leg of the clip angle were screwed to the unlipped channel and the lipped C-channels, respectively. In tensile tests, adjacent structural members were assembled by 10-gauge self-drilling screws. The shear test specimen was designed as a H-shaped specimen, as shown in Figure 1(b). The ends of the lipped channel were inserted into the unlipped channel, assembled by two clip angles. Similar to the tensile specimen, the unlipped and lipped channels were assembled to the short and long legs of angles, respectively. In shear specimens, two types of specimens (with 10-gauge and 14-gauge screws) were used. A total of nine specimens, including three tensile and six shear specimens, were tested.

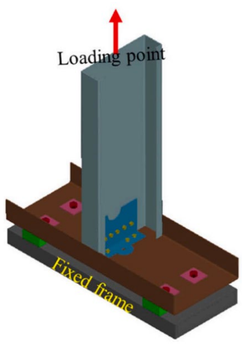

(a) tensile test setup

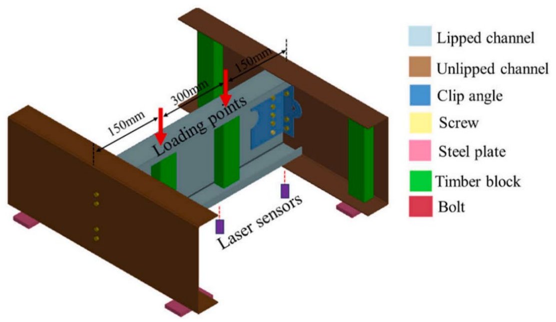

(b) shear test setup

Figure 1. Test setup for ledger-to-joist connections with clip angle

Two types of C-channels, lipped and unlipped, were used. Both channels were manufactured from a coil with thickness of 2.4 mm. The depths of the selected lipped and unlipped sections were 235 mm and 240 mm, respectively. The unlipped channel features a clear internal height without any lip that allow the lipped section to fit inside. A commercial CFS clip angle was used to connect the floor bearer (FB) with the floor joist (FJ). Detailed geometries of unlipped section, lipped section, clip angle and screws are shown in Figure 2 and Table 1, in which d_h, d_f, l_h, l_s, l_p, and p represent head diameter, screw diameter, head height, screw length, drill point length, and pitch, respectively.

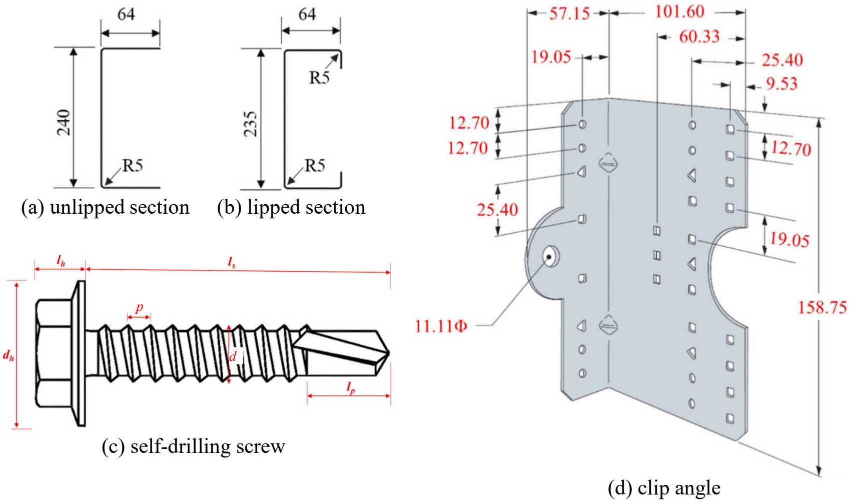

Figure 2. Geometries of each member and screw (unit: mm)

Table 1. Geometric parameters of self-driving screws

Screw type	Parameters						
	d (mm)	d_h (mm)	l_h (mm)	l_s (mm)	l_p (mm)	p (mm)	TPI
10-gauge	4.80	11.40	4.75	16	4.80	1.58	16
14-gauge	6.30	14.10	6.40	25	6.80	2.54	10

A summary of designed specimens name, dimensions, screw type, and number of screws on unlipped and lipped channels for both tension and shear tests is presented in Table 2. The schematic diagram of the test setups for applying tensile and shear loads to the designed connections are presented in Figure 1. A displacement-controlled tensile loading was applied at a rate of 5 mm/min.

Table 2. Summary of the tested CFS connection specimens

Test type	Specimen name	Screw type	Global dimensions (mm)	Screw distribution	
				Unlipped channel	Unlipped channel
Tension	FB4-FJ4	10-gauge	300 x 300	4	4
	FB6-FJ7	10-gauge	300 x 300	6	7
	FB8-FJ7	10-gauge	300 x 300	8	7
Shear	FB4-FJ7	10-gauge	600 x 600	4	7
	FB6-FJ5	10-gauge	600 x 600	6	5
	FB6-FJ7	10-gauge	600 x 600	6	7
	FB4-FJ7	14-gauge	600 x 600	4	7
	FB6-FJ7	14-gauge	600 x 600	6	7
	FB6-FJ12	14-gauge	600 x 600	6	12

Test results

The tested material property of two channel is shown in Appendix A (Bohara et al., 2024). Load-displacement curves for all specimens are shown in Figure 3. Regarding the three tensile tests, a linear relationship was observed between the applied load and displacement. A similar response was observed for all specimens before the displacement of 3.5 mm, regardless of the design specimen configurations. This similarity can be attributed to the comparable elastic stiffness of the clip angles used in all three specimens, as well as the identical geometries of FB and FJ components across the specimens. The inelastic behaviour of the clip angle started after the displacements of 3.5 mm, 7.0 mm, and 9.1 mm for specimens FB4-FJ4, FB6-FJ7 and FB8-FJ7, respectively, leading to the decreasing of stiffnesses. All three specimens failed by screw pull-out failure, leading to an abrupt drop of resistance, at the displacements of 19.1 mm, 30.1 mm and 41.3 mm, for FB4-FJ4, FB6- FJ7, and FB8-FJ7, respectively, with corresponding ultimate capacities of 10.22 kN, 18.80 kN, and 30.86 kN, respectively. The observed increase in stiffness and ultimate capacity of the tensile specimens correlates with the increasing number of screws on the FB. Moreover, the long leg of the clip angle, attached to the FJ, showed negligible deformation throughout the loading process, resulting in a minor effect on the overall response. In contrast, the short leg of the clip angle had a significant deformation, introducing appreciable geometrical and material nonlinearities, thereby providing a significant reduction in the specimen's stiffness. The stiffness of the specimens was enhanced by a greater number of screws on the shorter leg, of which provided greater constraint to the clip angle.

Regarding the six shear specimens, the load-displacement curves for specimens with 10-gauge and 14-gauge screws are shown in Figure 3(b) and (c), respectively. The ultimate load capacities of the specimens with 10-gauge screws, FB4-FJ7, FB6-FJ5, and FB6-FJ7 were 60.9 kN, 49.4 kN, and 70.2 kN, respectively, while those of specimens with 14-gauge screws, FB4-FJ7, FJ6-FJ7, and FJ6-FJ12, were 58.8 kN, 63.4 kN, and 88.2 kN, respectively. Notably, two FB4-FJ7 specimens with different screw sizes showed similar ultimate capacities, with only a 2.0 kN difference. Additionally, the FB6-FJ12 specimen with 14-gauge screws had the highest load capacity (88.15 kN) among all tested shear specimens. The failure modes varied by screw size: three specimens with 10-gauge screws failed by the shear rupture of the screw on either leg attached to FB or that contacted with FJ. In contrast, due to the increased screw size for specimens with 14-gauge screws, the specimens failed to the shear buckling of the clip angle.

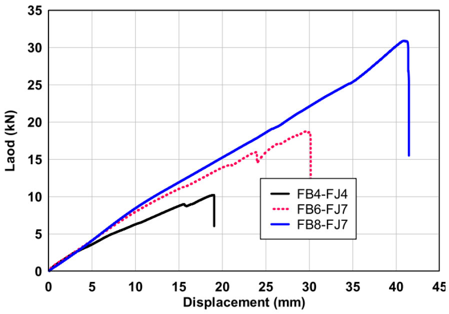

(a) tensile specimens

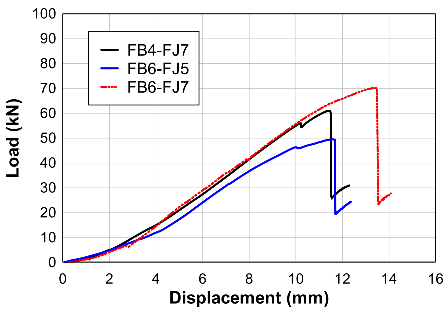

(b) shear specimens with 10-gauge screws

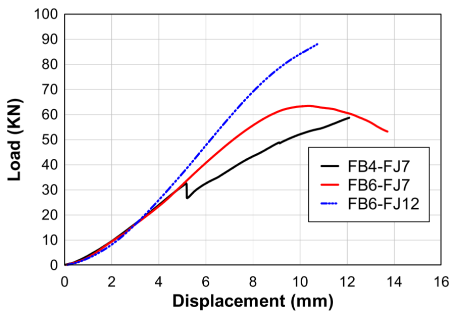

(c) shear specimens with 14-gauge screws

Figure 3. Test results for ledger-to-joist connections with clip angle

The failure modes of all tensile specimens are shown in Figure 4. All specimens failed by the screw pull-out on the unlipped channel, while screws on the lipped channel remained intact. The pull-out is led by the thread rupture in the screw, as shown in Figure 4(d). For specimens FB4-FJ4 and FB6-FJ7, the bending deformations around the line of screws were negligible. In contrast, a significant rotation of the shorter leg of the clip angle was observed in FB8-FJ7, as shown in Figure 4(c). The thread failure was observed across the three tensile specimens.

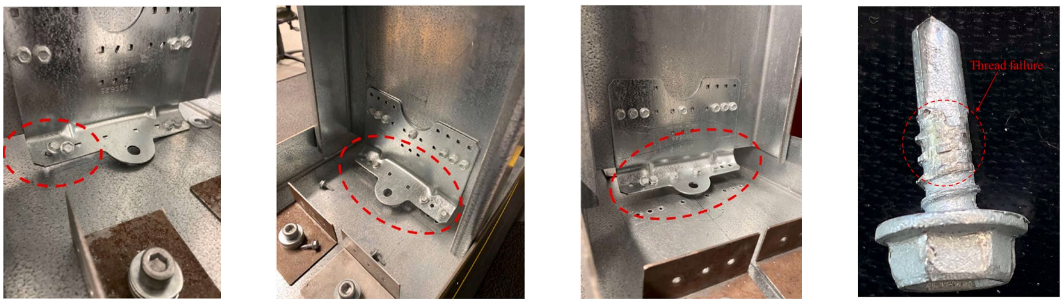

(a) FB4-FJ4 (b) FB6-FJ7 (c) FB8-FJ7 (d) screw

Figure 4. Failure modes of tensile specimens

The failure modes of the shear specimens are presented in Figure 5. The specimens with 10-gauge screws failed by shear ruptures of screws at either the shorter or longer leg. Regarding the specimen FB4-FJ7, the rupture was observed on the shorter leg (the unlipped channel section). With the increased number of screws on FB, the shear rupture shifts from FB to FJ, as the result of FB6-FJ5 and FB6-FJ7. For all specimens with 10-gauge screws, insignificant deformation was observed in the clip angle. In contrast, with the increase in screw size, the failure modes change to the shear buckling of the long leg of the clip angle, as shown in Figure 5(b). As the onset of out-of-plane bending of the clip angle, the lipped channel rotates in an out-of-plane direction, leading to a reduction in the specimen's resistance. Moreover, the shear buckling resistance increases with the screw number, which is attributed to that more screws provide more appreciable constraints on the connected leg.

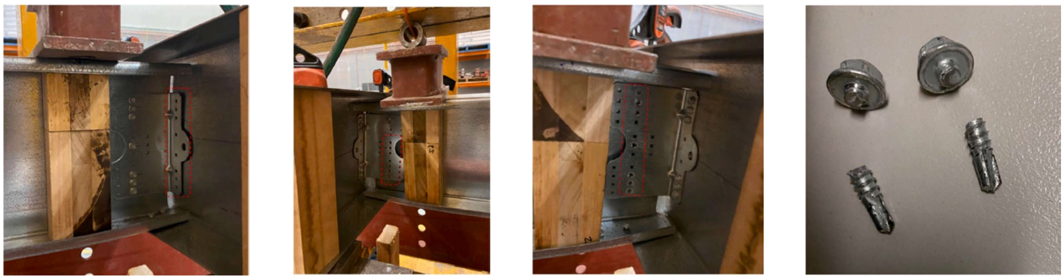

FB4-FJ4 FB6-FJ7 FB8-FJ7 screw

(a) specimens with 10-gauge screws

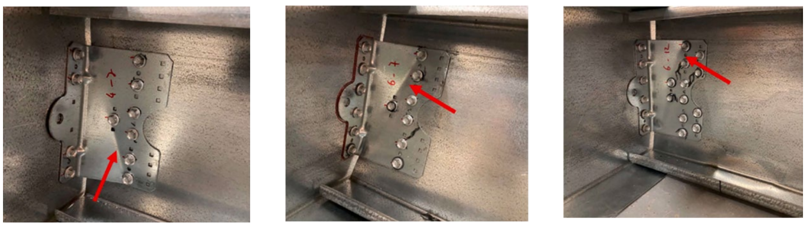

FB4-FJ7 FB6-FJ7 FB6-FJ12

(b) specimens with 14-gauge screws

Figure 5. Failure modes of shear specimens

3.3 Finite element analysis

FE model

An FE model was developed using the commercial software Abaqus. For both specimens under tension and shear, only half of the specimen was modelled, owing to the specimen symmetry. The boundary condition and applied displacement were selected following the half-model symmetry and experimental loading procedure.

The bearer and joist were cut from two types of CFS channel sections with measured Young's modulus of 207000 MPa, engineering yield stress of 547 MPa, engineering ultimate stress of 576 MPa, and corresponding engineering ultimate strain of 0.04. The true stress and true strain is calculated through

$$\varepsilon_{\mathrm{true}}=\ln\left(1+\varepsilon_{\mathrm{eng}}\right) \tag{1}$$

$$\sigma_{\mathrm{true}}=\sigma_{\mathrm{eng}}\left(1+\varepsilon_{\mathrm{eng}}\right) \tag{2}$$

in which σ_{true} is the true stress, $\varepsilon_{\mathrm{true}}$ is true strain, σ_{eng} is engineering stress, and $\varepsilon_{\mathrm{eng}}$ is the engineering strain.

The clip angle was manufactured from cold-formed steel (CFS) with a yield strength of 345 MPa. The Young's modulus, ultimate engineering stress, and corresponding strain were not directly tested. However, as the clip angle was made from AS350 steel, these mechanical properties were estimated as 205,000 MPa for Young's modulus, 450 MPa for ultimate engineering stress, and 0.15 for the corresponding strain. The ultimate engineering stress of the screw was assumed to be 900 MPa, based on coupon tests reported by Quan et al. (2021).

The measured displacement incorporated the deformation of the test rig. Therefore, an equivalent loading model, shown in Figure 46, is adopted in this paper to replicate the actual tests. This approach was previously applied to simulate the force-deformation curves of coped beams (Zhou et al., 2024) and bolts in tension (Yang et al., 2021) when the stiffnesses of the test setup or rig were unknown. Since the rig was designed to have a higher resistance than the connection itself, it is assumed to have behaved elastically during testing. As such, an elastic spring is introduced into the model to represent the rig's elastic deformation, with its stiffness k_{r} is estimated by

$$k_{\mathrm{r}}=\frac{1}{\dfrac{1}{k}-\dfrac{1}{k_{\mathrm{c}}}} \tag{3}$$

where k_{c} is the initial stiffness of the connection, and k is the initial stiffness of the experimentally obtained force-displacement curves.

Same rig was used for specimens FB6-FJ7 and FB8-FJ7; and hence, both specimens share the same value of k_{r}, which can be estimated using the FE model result, k_{c} = 1.21 kN/mm, and experimental result, k = 0.73 kN/mm, for specimen FB6-FJ7. Substituting the values of k = 0.73 kN/mm and k_{c} = 1.21 kN/mm into Eq. (3), the calculated value of k_{r} is equal to 1.8 kN/mm. Consequently, with the stiffness of the rig known, the FE force-displacement curve of the connection can be converted to the force-displacement curve of the connection with the effect of rig. The clip angle was connected to the strong sub-plate with the screw head contacting the sub-plate.

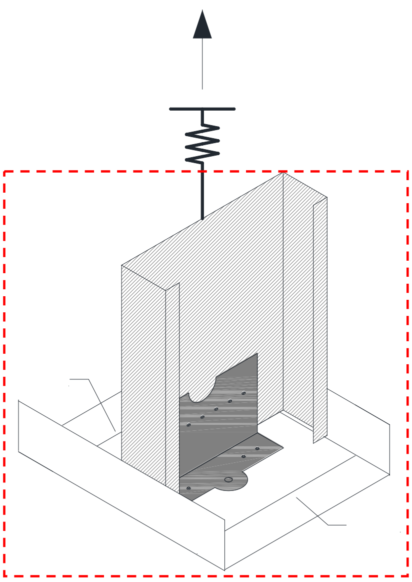

Figure 6. Equivalent loading model

Screw modelling method

The behaviour of screw under shear and tension is modelled through several connector elements, as shown in Figure 7. In

Figure 7(a), the screw hole is modelled by "Screw area" with the diameter D_{sa} of the outer screw thread diameter (d) for both sheets in touch and not in touch with the screw head/washer. Additionally, the screw head (or washer) is simplified by a "Screw circle" in Figure 7(b), with diameter, D_s, of either d_h or d_w, which are the diameters of screw head and washer, respectively, depending on whether the screw is used without or with a washer placed under the screw head. The geometric parameters of screw are shown in Figure 8. The elastic "Screw circle" is represented by elastic modulus of 205000 MPa, and the thickness is defined as the real thickness of screw head or screw head plus washer. The position of the screw circle is located exactly same as that of the screw head or wash, as shown in Figure 7(c).

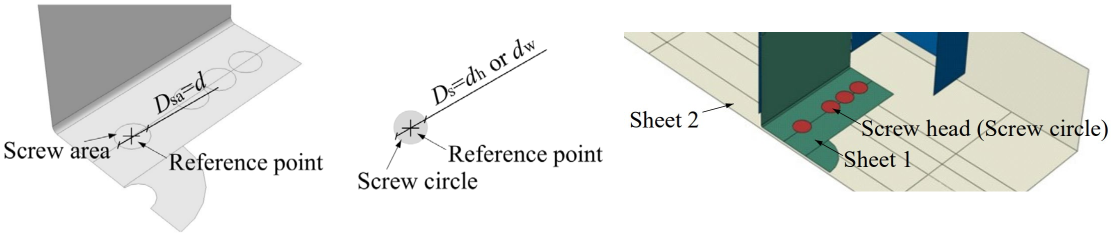

(a) sheet (b) screw (c) Schematic of the connection

Figure 7. Screw modelling technique

The screw hole wall and screw are represented by the reference points, which are created at the centre of the Screw area and the centre of the Screw circle, as shown in Figure 7(a, b). The reference point is coupled to the corresponding Screw area or Screw circle, using the "Coupling" function in Abaqus. One set of three connectors, i.e. one Axial-type connector and two Cartesian-type connectors, is used to model each transferred load (either tension or shear) between the two structural members, linking the corresponding reference points (RPa to RPb), as shown in Figure 9(a), and requiring an additional reference point (RPc) to bridge them together. Therefore, there are six connectors in total for modelling of one screw, including three for tension and three for shear.

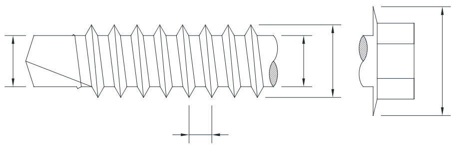

Figure 8. Geometric parameters of screw

The Cartesian-type connector establishes a connection between two reference points, enabling independent movement in three local Cartesian directions that align with the coordinate system at the first reference point. This setup is often used to decouple the forces between two components. For instance, consider a screw affixed to a sheet with a rigid boundary condition, as illustrated in Figure 9(b). The force transferred from the screw (RPa) to the sheet (RPb) can be decomposed into two components: a tensile force in the x-direction and shear forces in the y-z plane. The tensile force induces deformation of the screw along the x-axis. To isolate this effect, Cartesian-type connector 1 is assigned rigid stiffness in the x-direction while remaining flexible in the y- and z-directions, allowing RPc to move with RPa along the x-axis, as depicted by RPc (tension) in Figure 9(b). Meanwhile, Cartesian-type connector 2 is configured with rigid stiffness in the y- and z-directions and flexibility in the x-direction, restricting RPb and RPc to relative movement only along the x-axis. Additionally, an Axial-type connector, representing the tensile behaviour of the screw (blue curves in Figure 9(b)), is created between RPb and RPc. This connector establishes a link between two reference points, transmitting forces along the line connecting them.

In contrast, the shear force induces the corresponding deformation of the screw within the y-z plane. To capture this behaviour, Cartesian-type connector 1 is configured with rigid stiffness in the y- and z-directions while remaining flexible in the x-direction, and Cartesian-type connector 2 is assigned rigid stiffness in the x-direction but remains flexible in the y- and z-directions. An Axial-type connector, representing the shear characteristics of the screw, is established between RPb and RPc to sustain the shear force transferred between these reference points. It is important to note that RPc is positioned at the same location as RPb (not as depicted in the figures), ensuring that the elongation of the Axial-type connector aligns with the load direction.

With this force transfer approach, the screw modelling method for the CFS connection is illustrated in Figure 9(c), featuring a connection comprising two sheets and a screw. For forces in the x-direction, the load is initially transferred from Sheet 1 to the screw through the established contact between Sheet 1 and the screw circumference. The force is then transmitted to the screw area in Sheet 2 via a set of connectors designed to capture tension (indicated by the red dashed line). For shear forces in the y-z plane, the load is first transferred from Sheet 1 to the screw and then passed to Sheet 2 through two sets of connectors that model shear transfer, shown as the blue dotted and purple dot-dashed lines. Further details on the screw modelling method and the finite element (FE) model of the specimen can be found in Appendix A (Zhou et al. (2025a)).

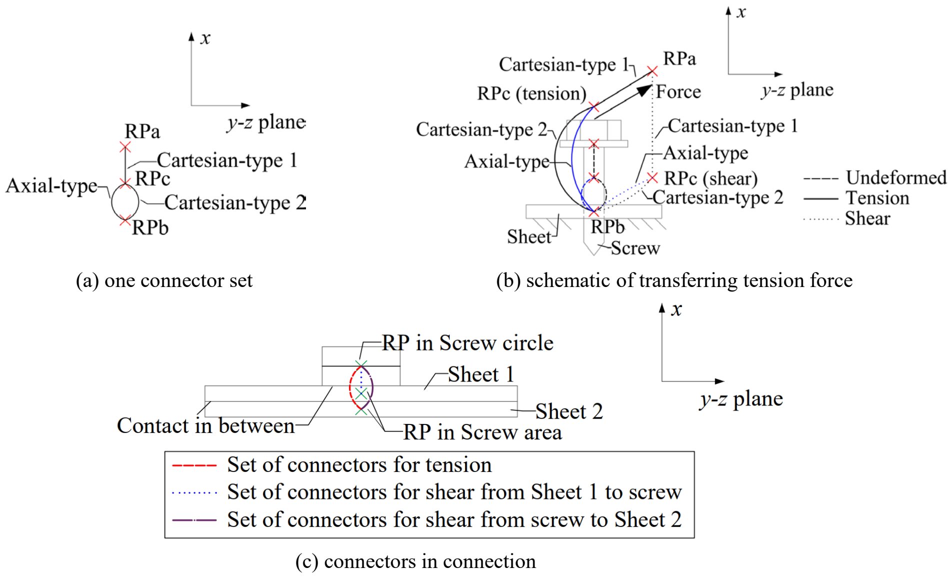

Figure 9. Modelling technique for load transferring

Figure 10 shows the force-deformation curves of all connections obtained from the proposed FE model and experiment. The predicted failure modes of the specimens with screws of 10-gauge are screw shear failure and those of specimens with screws of 14-gauge are the buckling of clip angle, which are consistent with the experimental observations. A deviation was observed at the beginning of loading, where soft initial stiffnesses were reported across all specimens. This behaviour is attributed to the loose contact between the test specimens and the loading rig during installation, which resulted in no load being effectively applied to the specimens at loading start.

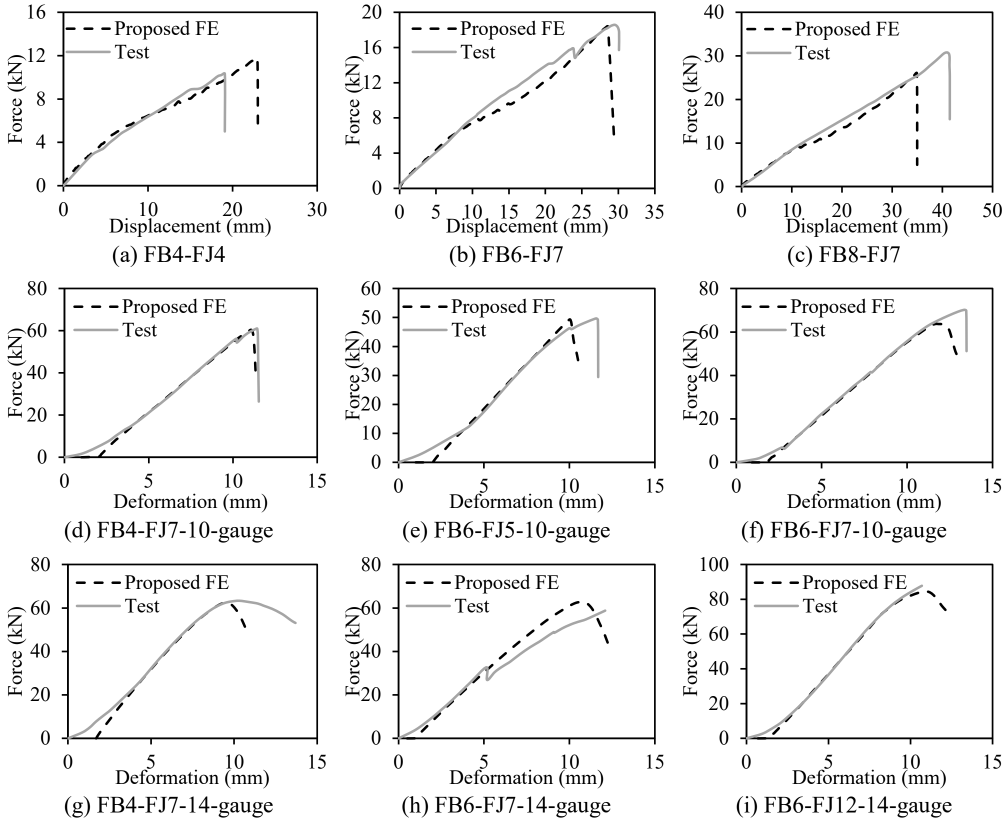

Figure 10. Force-deformation curves of ledger-to-joist specimens

Parametric study

The details of the parametric study of both specimens under shear and tension can be found in Appendix A (Zhou et al. (2025a)). The important observations are concluded herein:

- The orientation of screw installation showed minimal impact on the ductility and load-bearing capacity of the specimens, indicating that variations in drilling direction are negligible in connection performance.
- Tensile specimens with an increased lever-arm length (the distance between the angle heel and the screw line) demonstrated enhanced ductility. This improvement is attributed to the reduced constraint provided by the screws on the clip angle, allowing for more deformation before failure.
- For tensile specimens with same lever-arm lengths, the position of screws had a minor effect on the resistance and ductility. This indicates that lever-arm length is a more critical factor than screw placement in determining connection's performance.
- In shear specimens where clip angle buckling occurred prior to the screws reaching the ultimate capacity, an initial peak in resistance was observed at the onset of buckling. This was followed by a gradual decrease in resistance, then a recovery, and a subsequent increase until a second peak corresponding to screw shear failure, as shown in Figure 11.

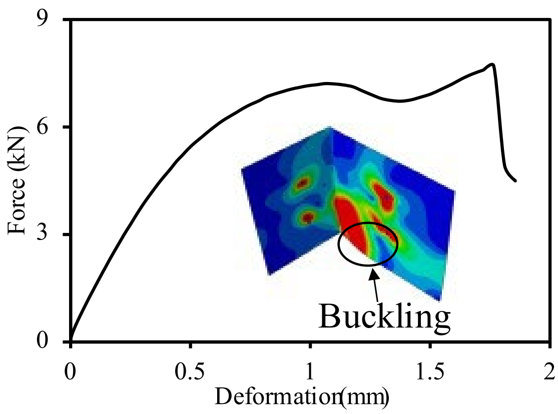

Figure 11. FE results for specimen failed by clip angle buckling

- The occurrence of clip angle buckling led to a non-uniform distribution of shear forces among all screws, resulting in a lower ultimate resistance compared to specimens with uniform shear force distribution.
- The edge distance of the screw significantly influenced the deformation behaviour of the clip angle. Smaller edge distances provided greater restraint to the clip angle, preventing buckling and enhancing the connection's capacity.

4. SUB-ASSEMBLY SPECIMEN

4.1 Introduction

Progressive collapse can occur when one or a few vertical structural members (such as columns or stud walls) fail, resulting from insufficient robustness in the remaining structure to sustain the redistributed loads. Once a vertical member fails, its original load is redistributed to adjacent members through catenary action, which is activated in horizontal members (e.g. beams, slabs, girders). The resulting significant tensile (membrane) force from catenary action demands adequate tensile strength from the connection above the removed vertical member to ensure effective load transfer and overall structural integrity. The capacity of a connection to resist this tension force is commonly referred to as the "tying force" (2016, Izzuddin and Sio, 2022, Arcuri et al., 2023). However, conventional connections between horizontal and vertical members, as well as between two horizontal members, are typically not designed to resist such large catenary-induced forces. This highlights the need to examine the tying force capacity of connections under vertical member removal scenarios.

Over the last three decades, research has primarily focused on assessing the tying force of connections through sub-assembly testing, involving horizontal members, damaged vertical members, and connections across two bays. Connections in mid-rise light gauge steel (LGS) buildings are generally designed to resist shear forces and bending moments. However, their limited tension capacity can result in premature failure, preventing effective load transfer to adjacent vertical members. This was demonstrated in the linear elastic analysis of a three-story cold-formed steel structure (Bae et al., 2008), which revealed that the membrane (tension) force generated by catenary action after stud removal exceeded the design tying force of the horizontal connections by more than five times. Therefore, to ensure reliable load redistribution to adjacent vertical members, it is essential to develop new connection designs that can provide sufficient tying force to resist these substantial membrane forces.

This section presents a new connection between two horizontal members, featuring simple geometry and easy fabrication. Six sub-assembly tests with different configurations were conducted to assess the tying force of the proposed connection. Additionally, a parametric study was performed based on the validated FE model to study the behaviour of the proposed connection under stud removal scenarios and its influencing factors. Lastly, a mechanical model was proposed for predicting the tying force requirement in robustness design codes, as an advantage by avoiding the complicated models for commonly used Component Method and FE method.

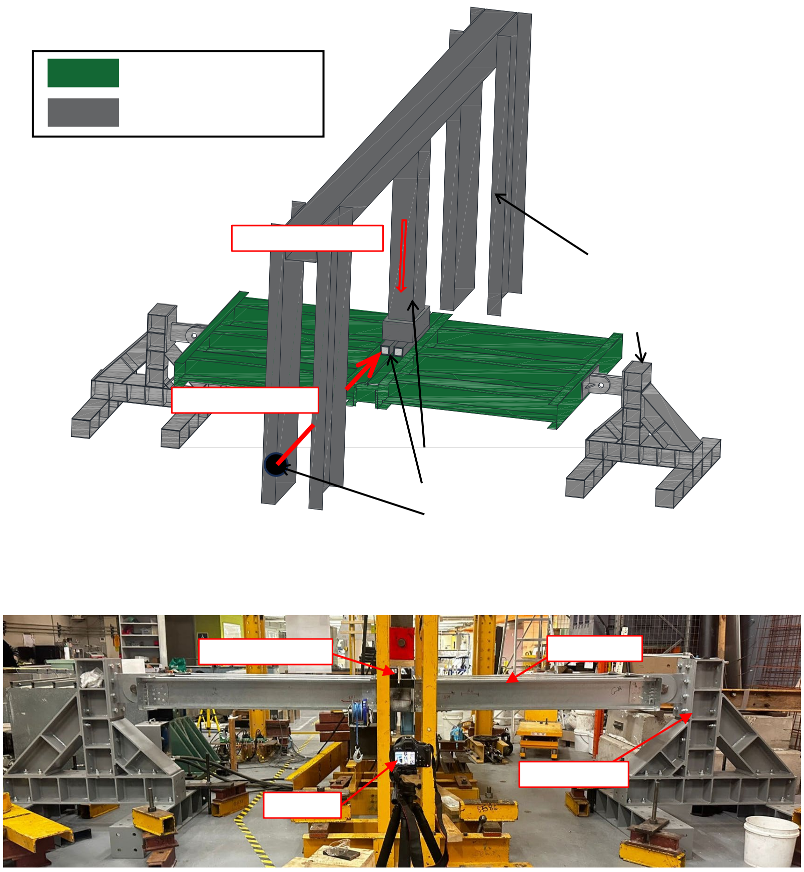

Figure 12. Test setup for all specimens

4.2 Experimental investigation

Test specimens and setup

A general layout of the test setup is presented in Figure 12, with detailed dimensions and geometries provided in Figure 13. Each sub-assembly specimen comprised three pairs of joists to account for scenarios where extreme events might damage multiple studs and affect joists over several spacings. This study adopted a standard joist spacing of 300 mm, as illustrated in Figure 13(b). After removing the stud walls between adjacent joists, identical ledger-to-joist connections were implemented at both ends of each joist, which led to the development of inflection points at the joist mid-spans. As a result, the specimens were designed with joists measuring half the span length and with idealised pinned supports at each end. In this study, a span of 3 m was used, giving a joist length of 1.5 m, as depicted in Figure 13. The central pair of joists in each specimen is referred to as the middle joists, while the other two pairs are designated as the side joists.

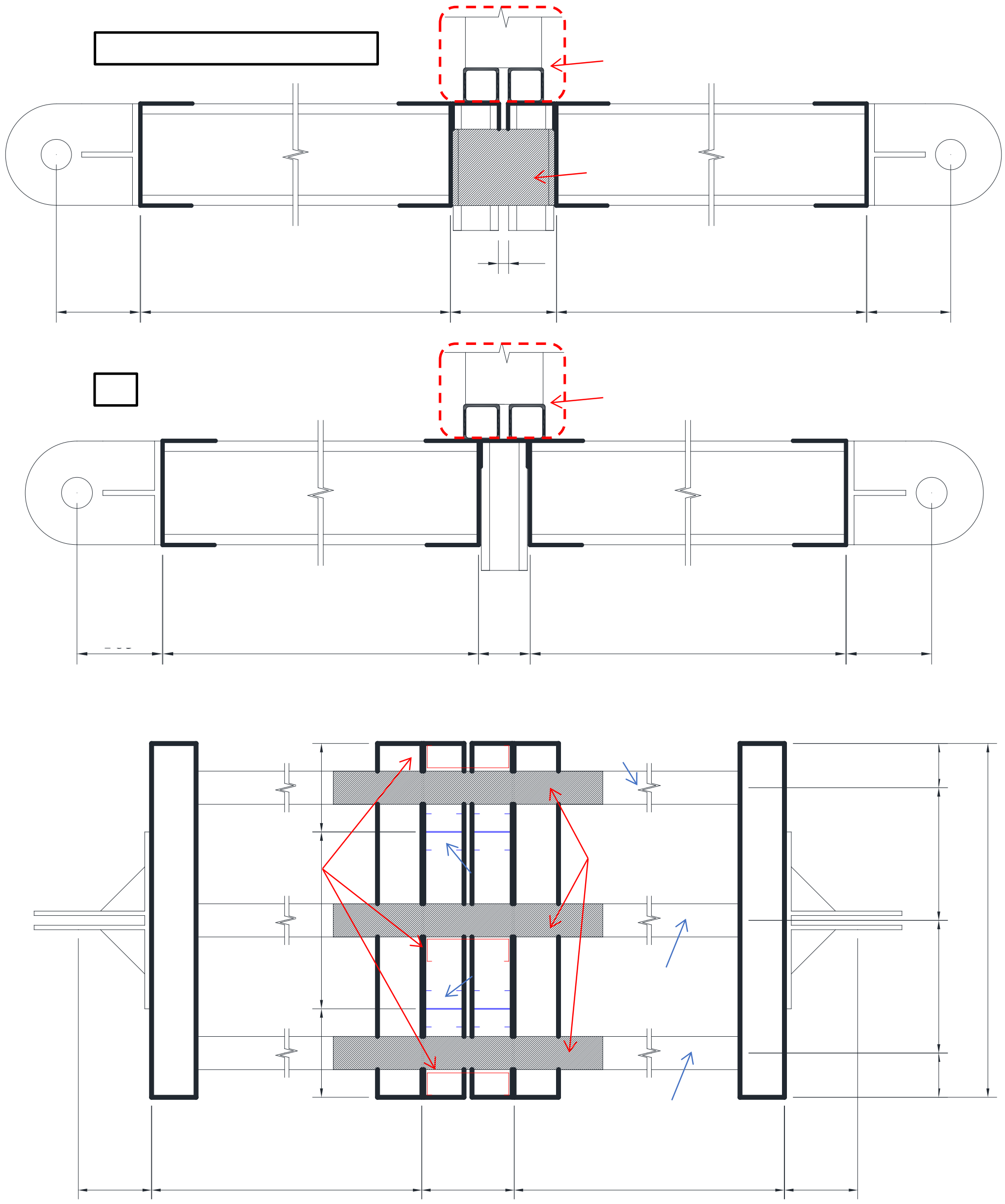

Figure 13. Schematic of test specimens (all dimensions in mm)

Two sets of studs were positioned at the midpoint between adjacent joists along the ledger direction. Typically, studs are either aligned directly above joists, placed adjacent to them, or situated midway between two joists. In this study, two new elements (which will be described later) were positioned both directly on and beside the joists. To prevent conflicts with these elements, the studs were located at the midpoint between two joists, maintaining a spacing of 300 mm. A double wall system was employed in this study, except for specimen S4 (to be discussed later), due to its acoustic benefits. Each set of studs in the double wall system was composed of two built-up members. It is important to note that in such double wall configurations, the walls and floors between adjacent bays are completely separated (2008), meaning there are no structural connections between them, resulting in zero tying force. Additionally, following standard ledger framing principles, top tracks were installed at the upper cross-sections of the studs.

Each specimen was pinned at both ends to horizontal supports, where the distance from the pin's rotation center to the surface of the ledger web was set at 165 mm. The pin supports were designed to permit rotation only along the direction of joist spacing. This constraint, combined with a symmetric loading configuration and test setup, effectively eliminated out-of-plane deformation of the specimens. To transfer the vertical load from the hydraulic actuator, which was braced against a reaction frame, two loading beams were employed. These beams were placed directly atop the top tracks of the specimen. The substantial normal contact force generated at the interface between the top track and the loading beams prevented any slippage. Without the loading beams, the actuator's relatively small bottom surface would have been in direct contact with the specimen's top surface. However, as the specimens undergo large vertical displacements, significant rotations occur, reducing the contact area and potentially compromising test accuracy. The use of loading beams, with a larger contact area, ensured uniform and consistent load distribution during testing, thereby minimising the risk of concentrated loads and potential inaccuracies due to reduced contact surfaces during significant specimen rotations.

Two elements were designed to resist the significant membrane forces generated by catenary action following the removal of stud walls: the stiffener and the bottom plate, as illustrated in Figure 14. Their placements are depicted in Figure 13. The bottom plate spans across two bays, connecting the bottom flanges of two joists with multiple self-drilling screws. To avoid brittle failure from screw shear, the combined strength of the screws was designed to exceed the strength of the bottom plate itself. Stiffeners are installed adjacent to each joist, linking the two ledger webs with several self-drilling screws.

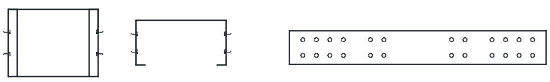

Figure 14. Schematic of two new elements

A total of six specimens were designed and tested, with specimen S1 serving as the baseline model. The key characteristics of each specimen are summarised in Table 3. Variations among the specimens include differences in ledger-joist connection configurations, joist dimensions (specifically, joist height), and the number of stud walls, represented by specimens S2, S3, and S4, respectively. Specimen S2 featured a weaker ledger-joist connection, a critical component in transferring horizontal forces generated by catenary action. Specimen S3 incorporated a larger joist size, influencing the development of arch action. Specimen S4 was configured with a single-wall system to facilitate a comparison of the bottom plate's effect between double and single wall setups. Notably, the gaps between the two joists along the joist length direction were 90 mm for S4 and 200 mm for the other specimens, as illustrated in Figure 13 (a). Since the size of the stiffener depends on the joist gap, variations in stiffener dimensions could affect its contribution to the tying force, and as a result, no stiffener was included in S4. Additionally, two specimens were designed to isolate the influence of specific elements: specimen S5 included three stiffeners, while specimen S6 incorporated only bottom plates. For specimen S5, the ledger web height was 50 mm greater than the joist web height. The top flanges of the ledger and joist were designed to be in contact, leaving a 50 mm gap between their bottom flanges. Furthermore, a consistent 20 mm gap between the two stud walls was maintained across all specimens, except for S4, as shown in Figure 13 (a).

Table 3. Key features of six tested specimens

Specimen	Ledger-joist connection	Height of joist	Wall system	New elements
S1	Strong	150 mm	Double	Bottom plate and stiffener
S2	Weak	150 mm	Double	Bottom plate and stiffener
S3	Strong	200 mm	Double	Bottom plate and stiffener
S4	Strong	150 mm	Single	Bottom plate
S5	Strong	150 mm	Double	Stiffener
S6	Strong	150 mm	Double	Bottom plate

.Ledger-to-joist connection

Each specimen contained twelve ledger-joist connections (LJCs), with six positioned near the stud wall and the other six located near the pin supports. These were referred to as middle LJCs and end LJCs, respectively. Specimens S1, S3, S4, and S6 shared the same LJC design. In these specimens, both the top and bottom flanges of the ledger and joist were connected by two screws arranged along the joist length, while the ledger and joist webs were joined by a clip angle. This web connection, termed Type-1, utilised eight screws on the ledger web and ten screws on the joist web, as illustrated in (a). It is important to note that all ledger-joist connections were assembled using 14-gauge screws, which have a shear strength of 13.0 kN and a tensile strength of 20.4 kN, as specified in the mill certificate.

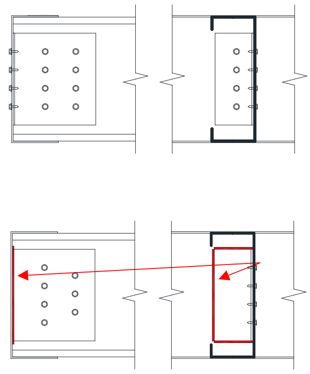

Figure 15. Schematics of web connections (screw numbers depends on specimen design)

In specimen S2, all LJCs feature the same flange connections as those in S1. However, a weaker web connection was introduced to examine its impact on specimen strength. Specifically, for all LJCs except the two end connections at the middle joists, the ledger and joist webs were joined by a clip angle secured with four screws on the ledger web and seven screws on the joist web. For the two end LJCs located at the middle joists, welding was used to attach the ledger leg of the clip angle to the ledger web, while the joist web and the clip angle's joist leg were connected using seven screws. This web connection is designated as web connection Type-2, as illustrated in Figure 15(b).

In specimen S5, no connection was designed between the flanges of the ledger and joist. The webs were joined using the Type-2 web connection, employing seven screws on the joist web. Notably, the exact positioning of screws in the LJCs required precise placement, significantly increasing assembly time and rendering the process impractical for efficient construction. To simplify assembly, the screws in the LJCs were instead positioned randomly.

Member

Table 4 summarises all the members used in each specimen, with detailed geometries illustrated in Figure 16. The ledgers, joists, and stiffeners were fabricated from grade G550 cold-formed steel (CFS) coils with a nominal thickness of 2.4 mm, while the clip angles were cut from G550 CFS coils with a nominal thickness of 2.0 mm. The studs were constructed by joining two C-sections with five 14-gauge screws. These C-sections were sourced from two types of G350 CFS with nominal thicknesses of 0.75 mm and 1.0 mm, and the corresponding studs were referred to as ST0.75 and ST1.0, respectively. A middle plate (MP) was designed to fill the gap between the bottom plate (BP) and the joist flange. Both BPs and MPs were cut from grade G450 CFS coils with a thickness of 2.4 mm. The BP, MP (or ledger flange), and joist flange were assembled using twenty-four 12-gauge screws (twelve per side), each with a shear strength of 10.6 kN and a tensile strength of 17.2 kN, as specified by the mill certificate.

Table 4. Members used in each specimen

Specimen	Ledger	Joist	Stud	S	BP
S1	FL200	FJ200	ST0.75	S150	BP680
S2	FL200	FJ200	ST0.75	S150	BP680
S3	FL250	FJ250	ST0.75	S200	BP680
S4	FL200	FJ200	ST1.0		BP570
S5	FL250	FJ200	ST0.75	S200	
S6	FL200	FJ200	ST0.75		BP680

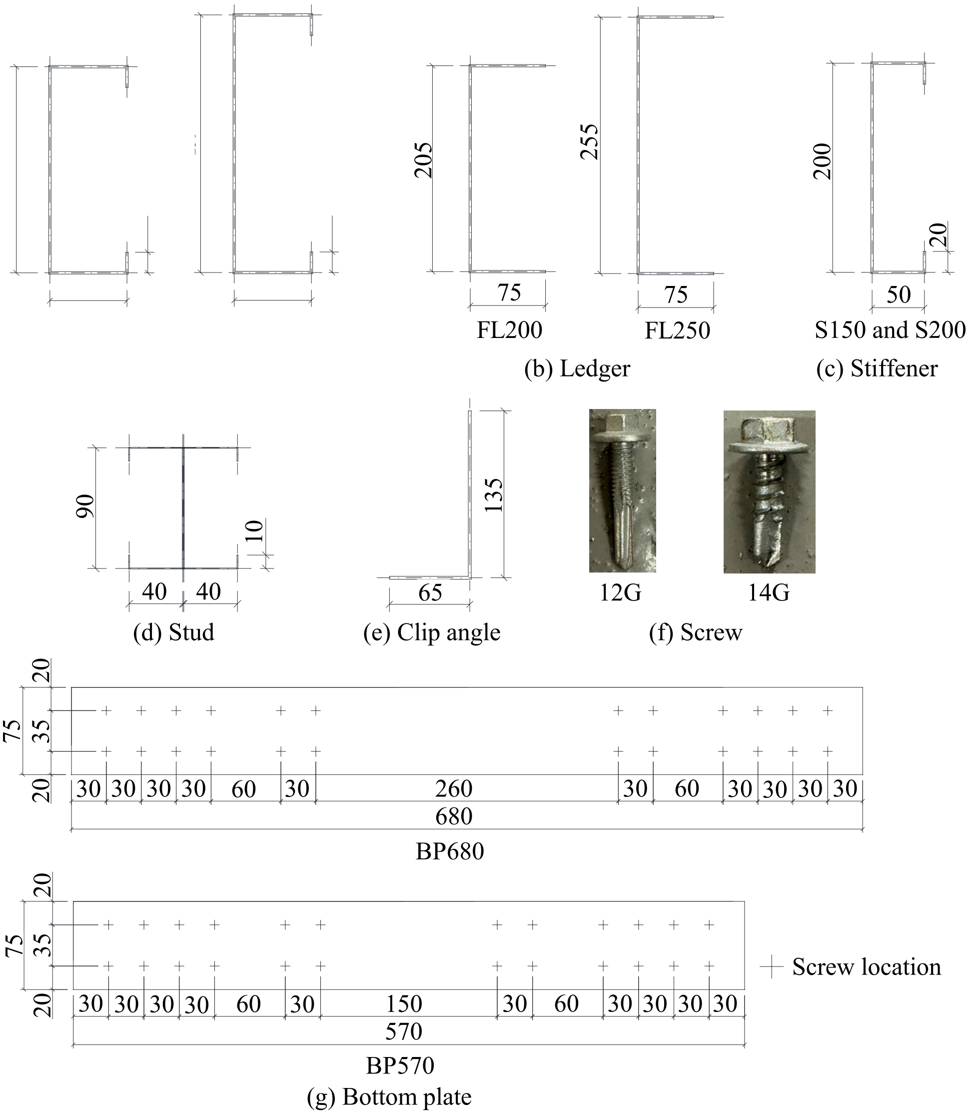

Figure 16. Geometry of each member (all dimensions in mm)

Test results

The test capacity (R_u), ductility (Δ_u), and ultimate horizontal force (R_{tu}, i.e. tying force) of all specimens are shown in Table 5. The test load-displacement curves of all specimens are shown in Figure 17.

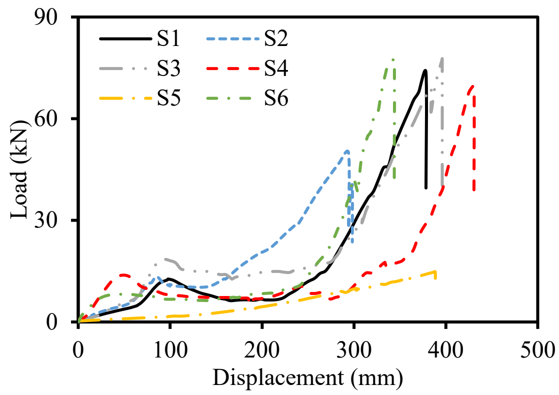

Figure 17. Load-displacement curve of sub-assembly tests

The ultimate tying force was not measured during the test but can be calculated through the load mechanism. All specimens except S5 share similar trend. The specimen reaches the first peak when the studs between two joists buckle, and hence a drop in resistance was observed. The resistances are recovered when an appreciable membrane action is activated. The load continuously increases until the final failure occurs.
As shown in Figure 18, the ultimate tying force can be calculated as:

$$R_{tu} = R_{mu} / 2\sin\theta_{mu} \tag{4}$$

in which R_{mu} is the ultimate measured vertical load, and θ_{mu} is ultimate rotation of joist. θ_{mu} can be calculated based on the specimen geometry and ultimate vertical displacement of specimen (Δ_{mu}):

$$\theta_{mu} = \tan^{-1}\left[\left(\Delta_{mu} - H/2\right)/\left(L - \Delta_p\right)\right] \tag{5}$$

in which H is the height of joist, L = 1500 mm + 165 mm = 1665 mm, which is the horizontal distance between load to the rotation centre, and Δ_p is the horizontal movement of pin support. The horizontal movement of pin support can be captured by a non-linear spring. The relationship between Δ_p and the horizontal component of R_{tu} ($R_{tu} \times \cos(\theta_{mu})$) is shown in Figure 18, thereby expressing their relationship by:

$$R_{tu}\cos\left(\theta_{mu}\right) = F_f + \frac{\Delta_p - \Delta_c}{k_o} \tag{6}$$

in which F_f, Δ_c and k_o are constant. The horizontal displacement of pin support can be calculated, which is

$$\Delta_p = \frac{R_{mu}L + 2\left(\Delta_{mu} - H/2\right)k_o\Delta_c - 2\left(\Delta_{mu} - H/2\right)F_f}{2\left(\Delta_{mu} - H/2\right)k_o + R_{mu}} \tag{7}$$

Accordingly, the ultimate tension force is calculated as:

$$R_{tu} = \frac{R_{mu}\sqrt{\left(L - \frac{R_{mu}L + 2\left(\Delta_{mu} - H/2\right)k_o\Delta_c - 2\left(\Delta_{mu} - H/2\right)F_f}{2\left(\Delta_{mu} - H/2\right)k_o + R_{mu}}\right)^2 + \left(\Delta_{mu} - H/2\right)^2}}{2\Delta_{mu} - H} \tag{8}$$

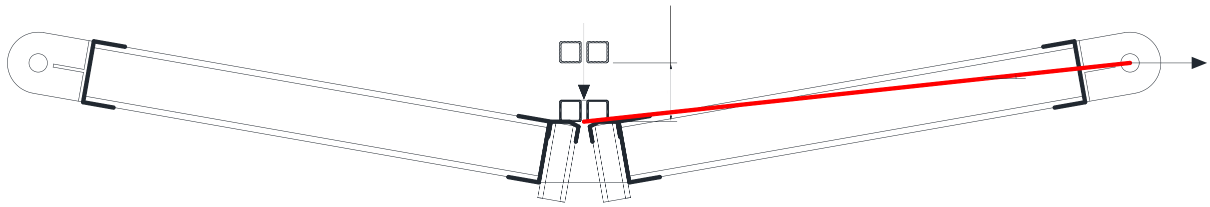

Figure 18. Load mechanism of the sub-assembly test specimen

All specimens exhibited similar capacity values, except for S2 and S5. Specimen S2, which featured weaker LJCs, demonstrated both lower capacity and ductility compared to S1, primarily due to the occurrence of brittle failure. The weaker LJCs in S2 were unable to sustain significant tensile forces, resulting in reduced horizontal load resistance. Furthermore, since the vertical force corresponds to the vertical component of the membrane force, a higher resistance to tension force leads to greater vertical load resistance. Consequently, S1 exhibited higher capacity than S2. The capacity of specimen S5 was 17.7 kN, significantly lower than that of S1. In S5, the stiffener exhibited minimal deformation, with most of the deformation concentrated at the middle LJCs.

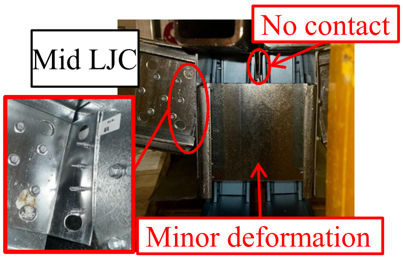

Figure 19. Failure mode of S5

Since the traditional double-wall system provides no tying force, the ultimate tying force measured for each specimen is considered as an enhancement to the tying capacity. Notably, specimen S5 (which incorporated only a stiffener) showed the lowest capacity at 17.7 kN, reflecting a 75.9% decrease compared to specimen S1. Conversely, specimen S6, which included only a bottom plate, demonstrated a tying force capacity similar to that of specimens S1, S3, and S4. Specifically, its capacity was just 0.3 kN (0.4%) lower than S3 and 3.9 kN (3.8%) higher than S1, indicating that the stiffener had minimal effect on improving resistance. Regarding ultimate tying force, specimen S5 recorded the lowest value at 35.4 kN, which was at least 110 kN lower than specimens that incorporated bottom plates.

Given the limited impact of stiffeners on improving tying force, a novel connection design is proposed. This design features a rectangular plate installed at the bottom flanges of two joists and is termed the joist-to-joist bottom plate connection (JBPC). Experimental results demonstrated that the JBPC exhibits high ductility (over 350 mm vertical displacement) and appreciable vertical load resistance (approximately 75 kN), significantly enhancing the design tying force and the overall robustness of cold-formed steel (CFS) structures. Moreover, the bottom plate offers superior ductility compared to screws under both tension and shear loading. Consequently, ledger-to-joist connections, which primarily fail due to screw failure, should be designed to provide greater tensile resistance than the JBPC to prevent brittle failure. The tensile resistance of ledger-to-joist connections can be determined using the recently proposed design methods (Obeydi et al., 2020b, Obeydi et al., 2020a, Zhang et al., 2018, Bohara et al., 2024). Failure modes of each specimen are concluded in Figure 20.

Table 5. Summary of the tested results of six sub-assembly specimens

Specimen	R_u (kN)	Δ_u (mm)	R_{tu} (kN)
S1	73.5	378	182.1
S2	49.8	294	166.0
S3	77.7	396	196.9
S4	69.4	431	148.4
S5	14.7	388	35.4
S6	77.4	344	214.3

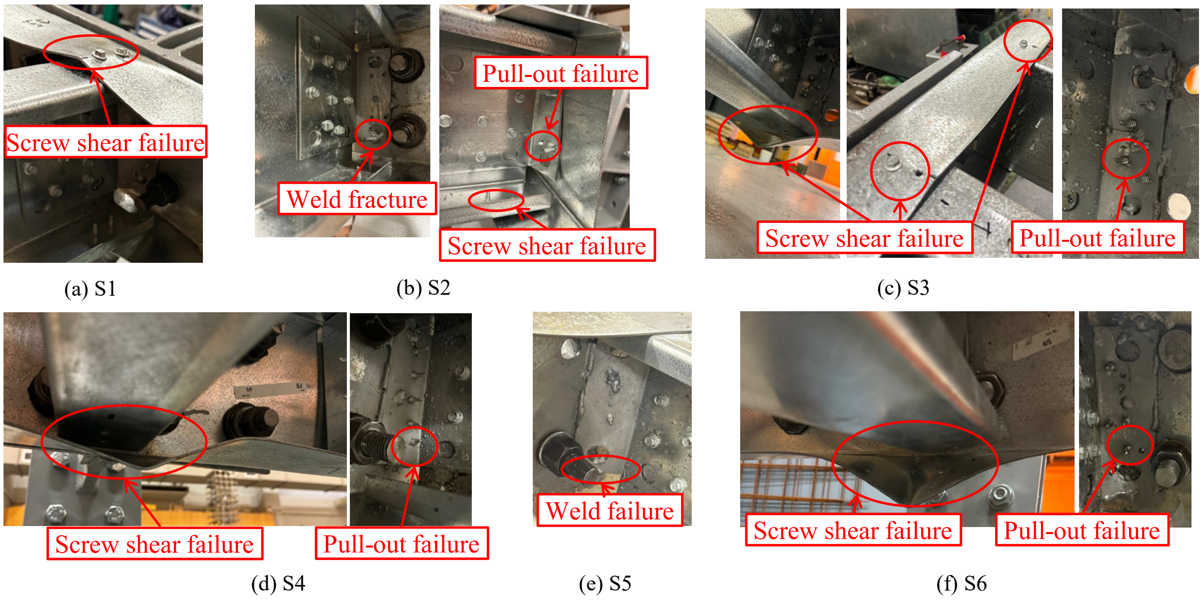

Figure 20. Failure modes of sub-assembly tests

4.3 Finite element analysis

FE model

A FE model was created using the commercial software Abaqus. All structural components were represented with four-node shell elements with reduced integration (S4R). To illustrate the modelling method, Figure 21 shows the FE model of specimen S1.

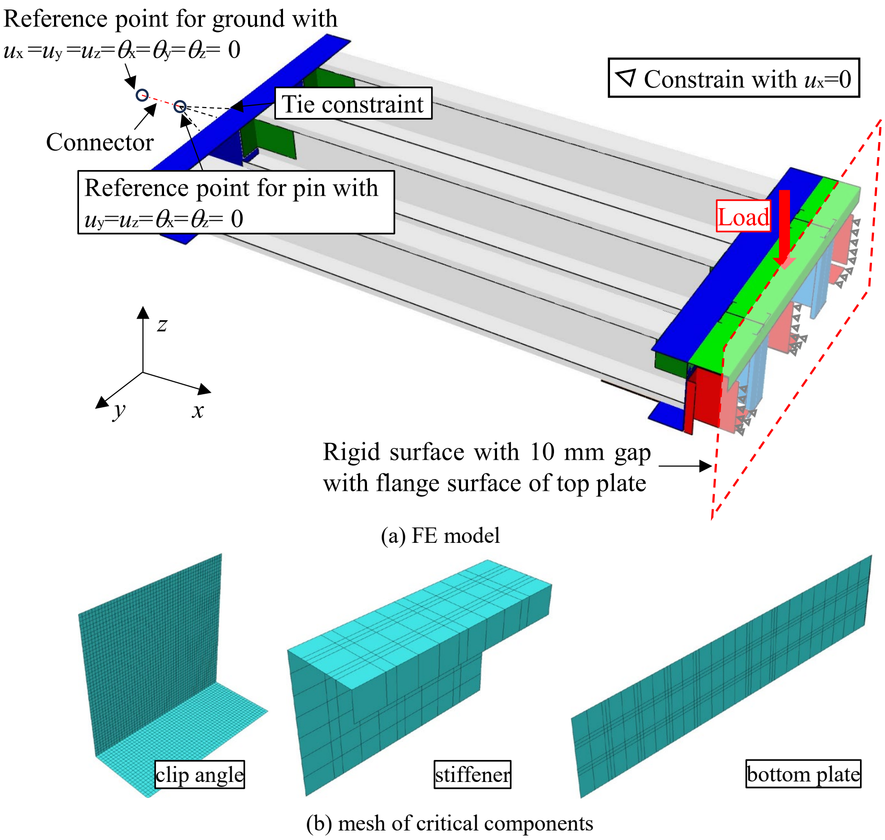

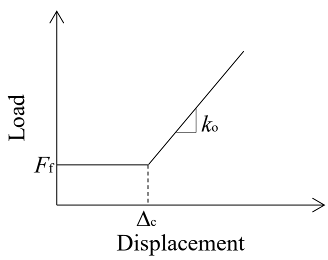

Figure 21. Load-displacement curve of axial-type connector to simulate slippage and overturning of pin support

Figure 22. FE model for specimen S1

Due to the specimen's symmetry, only half of the structure was modelled. Boundary conditions and applied displacements were selected to reflect both the half-model symmetry and the experimental loading setup. A rigid plate was placed 10 mm away from the stud flange surface to simulate contact between two stud walls during large deformations. The end ledger was linked to a reference point (RP), positioned 165 mm away from the web centreline in the x-direction, replicating the rotation centre of the pin support. The screws were modelled following the methodology outlined in Section 3.

The slippage and overturning of pin support are modelled by an axial connector between the reference point of pin and reference point of ground floor. The response of axial connector is shown in Figure 22. The initial movement of pin support, caused by overcoming the friction force (F_f), continues until the pin support firmly contacts the strong floor, and the corresponding displacement is denoted as Δ_c. The overturning is modelled with a linear response characterised by a stiffness of k_o. The F_f, Δ_c and k_o are calibrated through the FE model of specimen S1, which are 10 kN, 35 mm and 62.5 kN/mm, respectively。

FE results

The FE modelling results for all specimens are shown in Figure 24. T The proposed FE model is generally in good agreement with the test results, capturing all important phenomenon observed during the tests, *e.g.* the contact between two stud walls and buckling of studs. The mean FE-to-test ratios of R_u and Δ_u are 1.05 and 0.91, respectively.

The predicted failure modes of all specimens, along with the experimental results, are shown in Figure 24. All predicted failure modes are consistent with the experimental results, except for S2 and S5. Specifically, the predicted failure modes of S2 and S5 are the screw shear failure at flange connections and pull-out failure at web connections, respectively, rather than both weld fractures as observed experimentally. The discrepancies are due to the use of the "Tie" constraint in modelling the welds, which assumes infinite resistance. Therefore, this assumption results in an overestimation of the capacities of S2 and S5 by 37.6% and 25.9%, respectively. Given that the accurate prediction of load-displacement curves for specimens assembled using screws, the FE model is applicable to the proposed connection, which includes screws only.

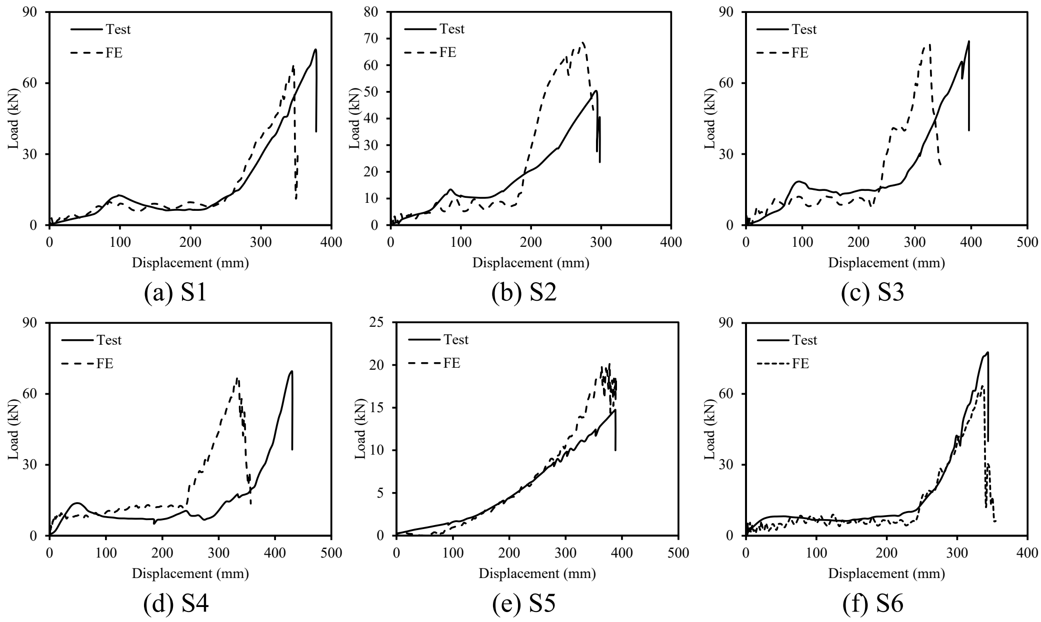

Figure 23. FE results of all specimens

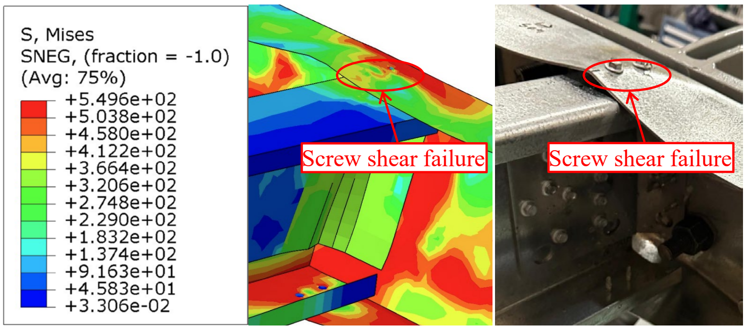

(a) S1

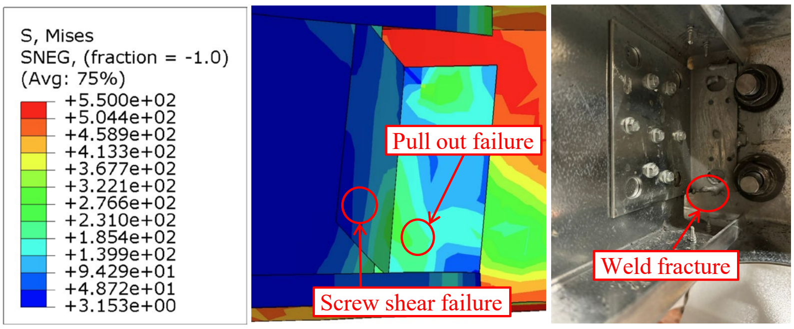

(b) S2

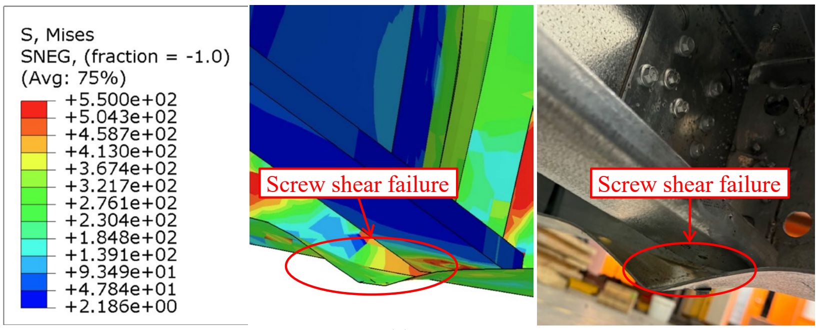

(c) S3

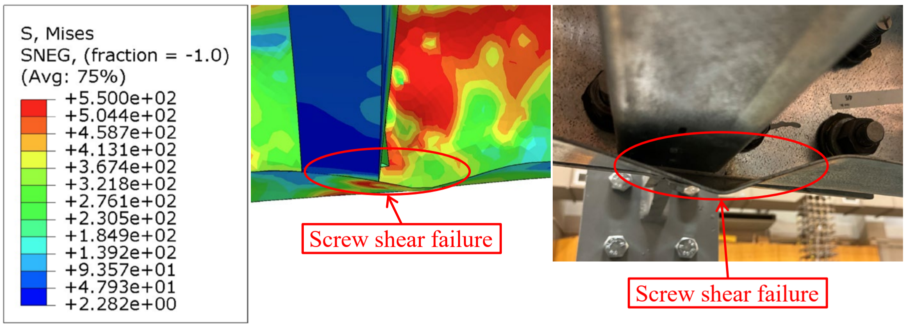

(d) S4

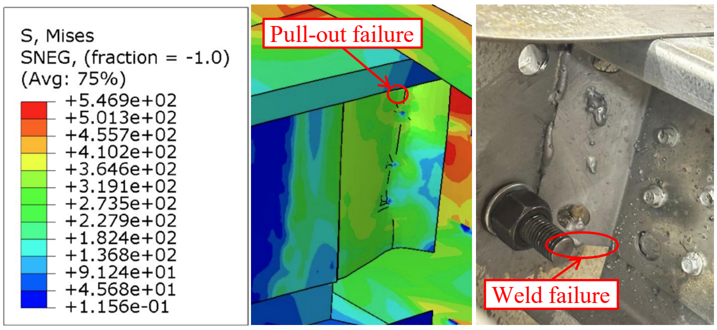

(e) S5

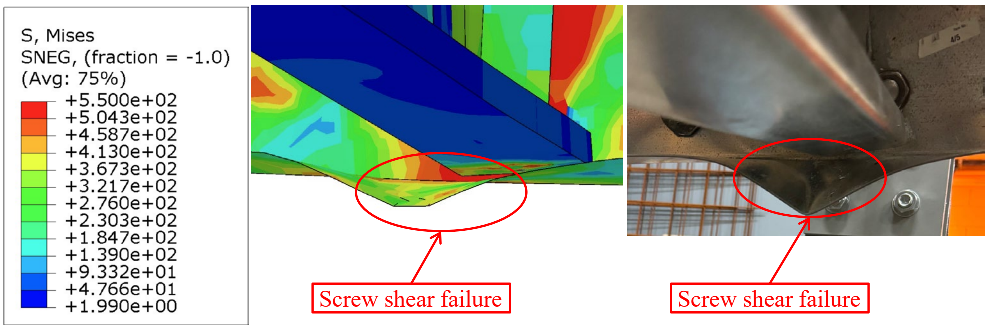

(f) S6

Figure 24. FE predicted failure modes of all specimens

Parametric study

The details of the parametric study of new proposed connection can be found in Appendix B. The important observations are concluded herein:

- The middle plate between joist flange and bottom plate has minor effect on the capacity of the new proposed connection.
- For specimens failed by plate in tension, the stiffness decreases as the screw number decreases. At a certain vertical displacement of joist, a specimen with a greater number of screws generates a larger membrane force due to a more appreciable tensile stiffness of specimen along joist length direction. As the vertical resistance is equal to the vertical component of membrane force, specimens with more screws show higher vertical resistances for a given vertical displacement. Regarding the capacities of specimens failed by plate in tension, the one, exhibited greater ductility, generates more significant catenary action, thereby leading to a higher capacity. Conversely, for specimens that fail due to screw shear, the capacity decreases with fewer screws, because of a reduced ultimate capacity on resisting membrane force.
- The capacity of connection increases proportionally with the width and thickness of BP. The increase is attributed to the enhanced tensile strength of BP that provides a greater membrane force.
- The negligible effect of the screw number in ledger flanges and distance between two first screw rows on the specimen’s response was observed.

5. BUILDING ANALYSIS TO RESIST PROGRESSIVE COLLAPSE

5.1 Introduction

The AP method, featuring advantages of threat independent and flexibility in implementation, is incorporated in current design provisions, which requires that the building be capable of bridging over a missing structural member, with the resulting extent of damage being localised. Most of the accordingly research focuses on framed buildings and hot-rolled steel or composite materials, with LGS buildings being studied only in Bae et al. (2008). However, Bae et al. (2008) is limited to a case study of a low-rise two-story building, and no design provisions are proposed. Given the globally increasing number of mid-rise LGS load-bearing wall buildings (Watson et al., 2024), detailed design provisions for the building to resist progressive collapse are particularly important.

This section presents a comprehensive analysis of mid-rise LGS load-bearing wall buildings under initial stud wall removal cases and proposes a hand calculation design approach for resisting progressive collapse. An archetype mid-rise building is introduced for the FE analysis, incorporating simplified FE methods proposed to accurately capture the responses of each load-bearing member and connection. The FE analysis involves three external and two internal stud wall removal cases. Additionally, a hand calculation design approach is developed based on the FE analysis results, including the methods that account for dynamic effects and tributary area. The approach may serve as a standardised and user-friendly procedure for designing of mid-rise LGS buildings to resist progressive collapse

5.2 Archetype mid-rise LGS load-bearing wall building

The 8-story residential building was designed as a mid-rise CFS load-bearing wall structure located in Melbourne, Australia. The building features a typical floor plan measuring 18,360 mm × 21,980 mm, as shown in Figure 25. It comprises nine rooms connected by a central corridor. The stairs and lifts are positioned between Rooms 2W and 4W, surrounded by core walls marked as the grey area in Figure 25(a). All walls separating two rooms are designed as double-wall systems with a 20 mm gap between the two walls. All other walls are designed as single-wall systems. The overall building design complied with current code provisions within AS1170 (2002) and AS 4600 (2018). The test building was designed to have a height of 24 m, as 3 m height for each story. The detailed design is shown in Appendix C.

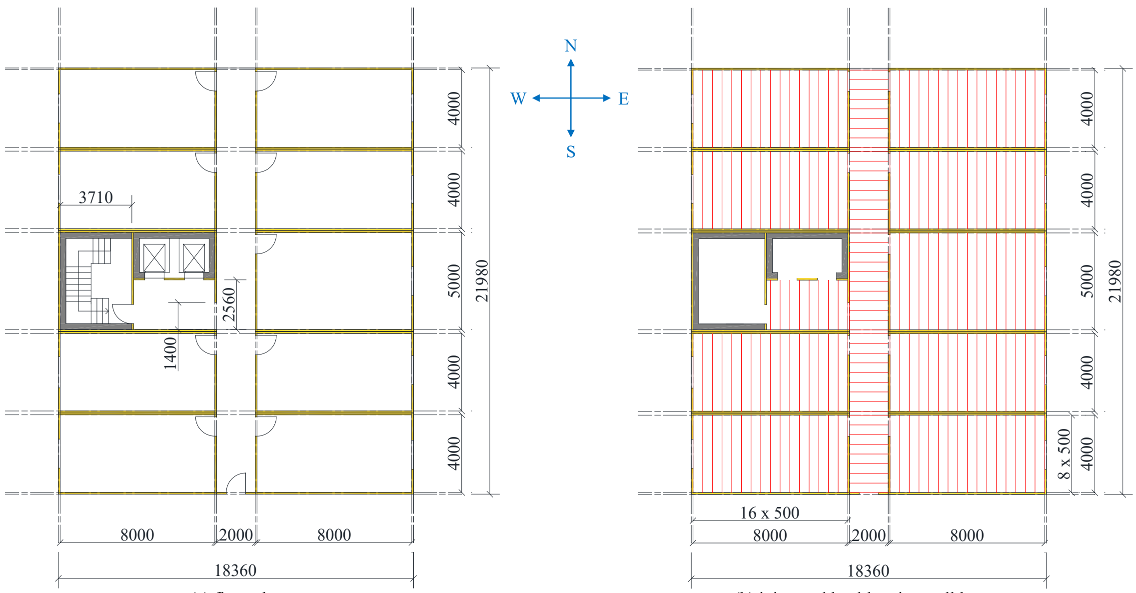

(a) floor plan (b) joists and load-bearing wall layout

Figure 25. Floor plan of the 8-story CFS building

5.3 FE modelling technics and validation

FE modelling technics

To simulate the response of the archetype building after extreme events, a simplified FE model is developed using Abaqus software. The model incorporates simplified modelling methods of each type of connection (including stud-to-track connection, ledger-to-stud connection, ledger-to-joist connection, and joist-to-joist bottom plate connection (JBPC), as shown in Figure 26) and member. The detailed simplified FE model is shown in Appendix C.

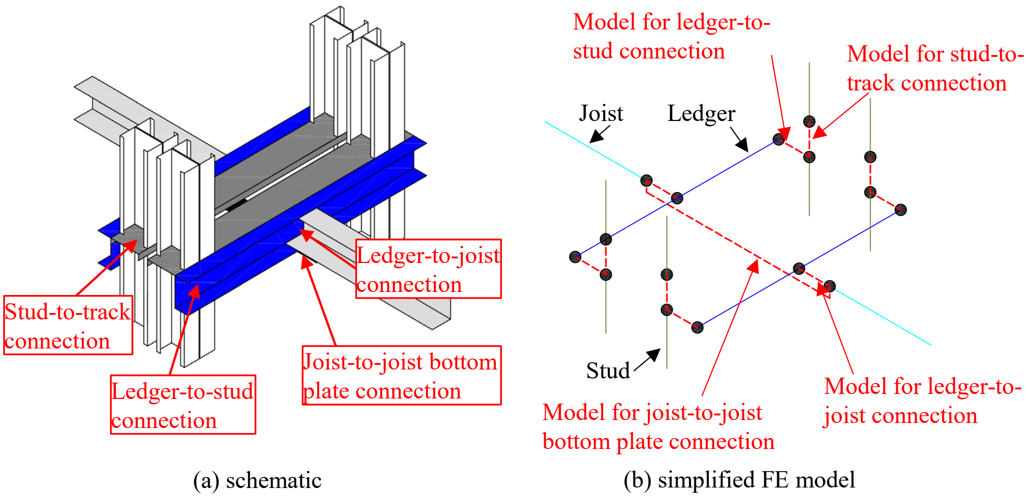

Figure 26. Schematic and simplified FE model of connections

Validation

The proposed method is validated by three different published test results.

Cantilever test

Cantilever tests were conducted in Ayhan and Schafer (2019), including one ledger-to-joist connection and two ledger-to-stud connections. Two configurations, representing small and large moment-to-shear ratios (*M*/*V*), used to validate the proposed simplified FE models. The major-axis rotational behaviour of the connector element in the ledger-to-joist connection is derived from an FE model using shell elements, as shown in Figure 27(a). The simplified FE model developed for the cantilever tests is shown in Figure 27(b).

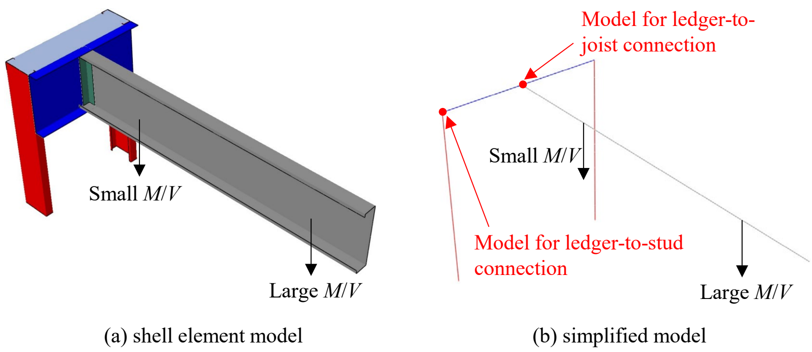

Figure 27. FE model of cantilever test

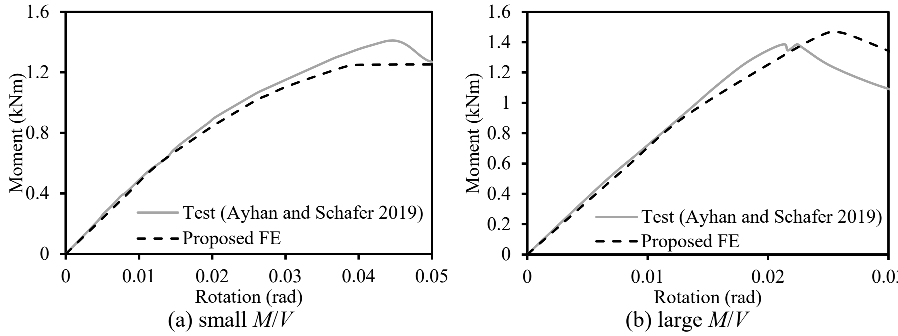

Figure 28. FE and test results of cantilever tests

Figure 28 shows the moment-rotation curves obtained from proposed simplified FE model and tests. The proposed simplified FE model shows good agreement with the test results, validating its applicability for further FE analysis of the archetype building.

Sub-assembly test

The sub-assembly test conducted in Section 4 includes the JBPC connection. The standard specimen in parametric study is used in this section for validation. Following the method provided in this study, the simplified FE model is developed, as shown in Figure 29. Figure 30 shows the load-displacement curves obtained from the proposed FE model and the model provided in Section 4. The proposed simplified FE model shows good agreement with the curve from Section 4, validating its applicability for further FE analysis of the archetype building.

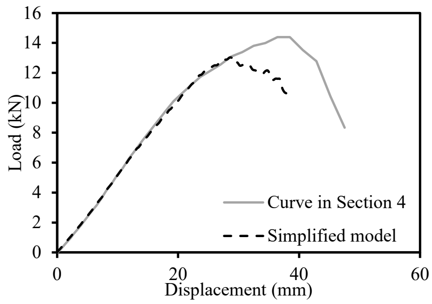

Figure 30. FE and test results of sub-assembly tests

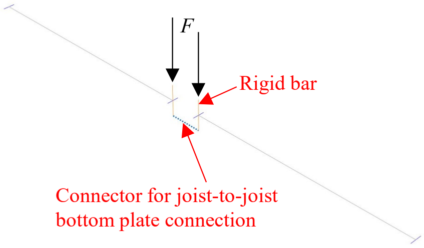

Figure 29. FE and test results of sub-assembly tests

Stud under compression

Two studs with plasterboards, tested in Vy and Mahendran (2022), WBC90-3000-300n-1s-1485 and WBC90-3000-300s-1s-1485, are used in this section for validation, in which the names of two specimens are kept the same as they were reported in the corresponding original papers. The FE modelling results are compared with the test results, as shown in Figure 31. The Figure shows good agreement between the simplified FE model and the test results. However, the proposed FE model slightly overestimates the stiffness of the stud after a displacement of 2 mm. The overestimation is attributed to the beam element's inability to capture localised deformation of the stud, non-uniform stress distribution on the cross-section, or both. Despite this limitation, the proposed method accurately predicts the ultimate capacities and initial stiffness of both specimens. Considering the balance between accuracy and computational efficiency, the proposed simplified FE model demonstrates its effectiveness for performing FE analyses of the archetype building.

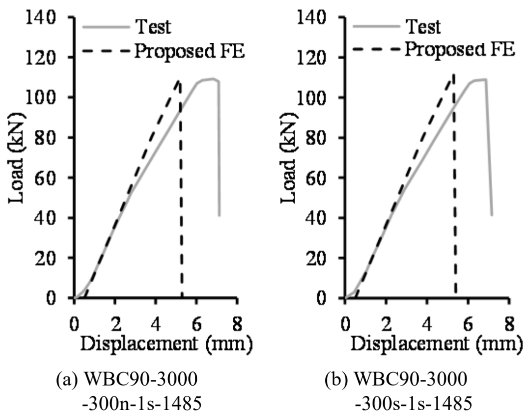

Figure 31. FE and test results of stud under compression

5.4 Case study of the archetype building

Figure 32 shows the FE model of archetype building, following the method proposed above-mentioned. The core walls have more appreciable stiffness and strength compared with other members and are therefore modelled with rigid boundary conditions. In the absence of shear strength design, the shear walls are modelled as rigid in-plane boundary conditions positioned at the locations of all load-bearing walls, effectively eliminating potential failures caused by shear forces. The material properties are represented using an elastic-perfectly plastic model based on isotropic von Mises plasticity. Note that the effects of the floors and plasterboard on load redistribution are not considered in this section.

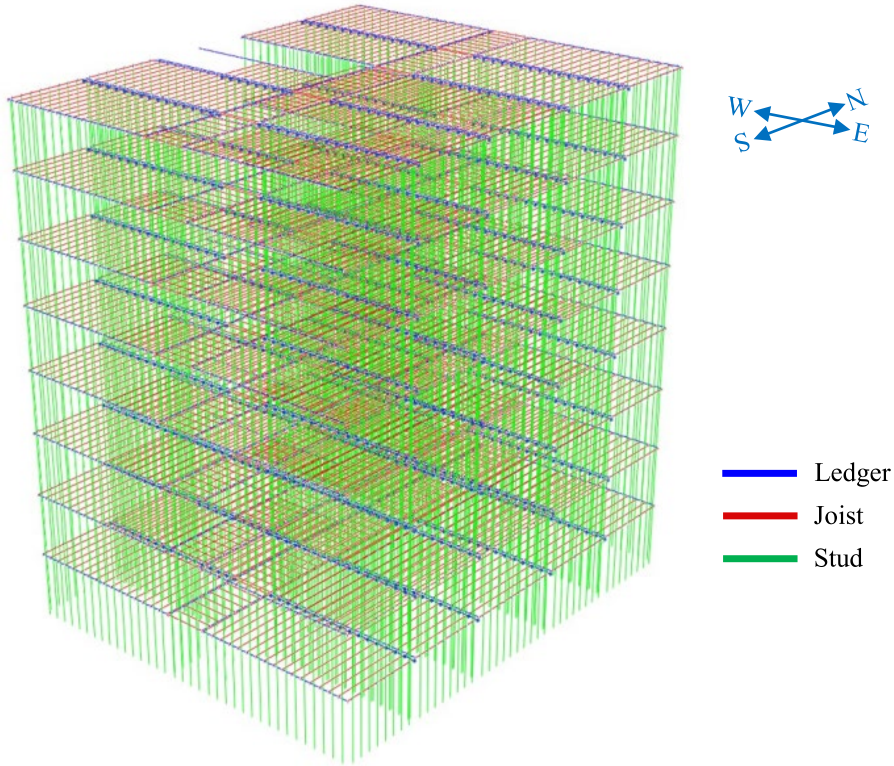

Figure 32. FE model of archetype building

Four analysis cases are considered, as shown in Figure 33. All cases are designed following the NCC guideline (2020), including three cases for external walls and two for internal walls, *i.e.* Case 1: external wall at the middle of the short side; Case 2: external wall at the middle of the long side; Case 3: external wall at Room 1E; Case 4: internal single wall at Room 3E. For all cases, a wall segment with a length equal to *H* is removed. The first two cases are the removal of studs on the joist, while the latter two cases are the removal of studs on the ledger. The removal time of 0.003 s and damping ratio of 0.4% are applied to all cases.

The detailed results are shown in Appendix C, a concise summary is shown as follows:

Table 6 concluded the critical studs along with their maximum axial forces (R_u), as well as the dynamic increase factors (DIFs). In Cases 1 and 2, the removal of the stud wall on the joist results in a relatively smaller increase in axial force on the adjacent stud. This is attributed to that the affected area is limited to a single joist, and the vertical gravity load is directly applied to the joist. In contrast, the removal of the stud on the ledger affects multiple joists, resulting in a greater influence on the vertical gravity load. This effect can be shown by the dynamic affected area, as shown in the theoretical model later. The affected joist in Case 4 is 1 m longer than that in Case 3, whereby the maximum axial force of stud C4W3W1 is 12.4 kN larger than C3W11W1.

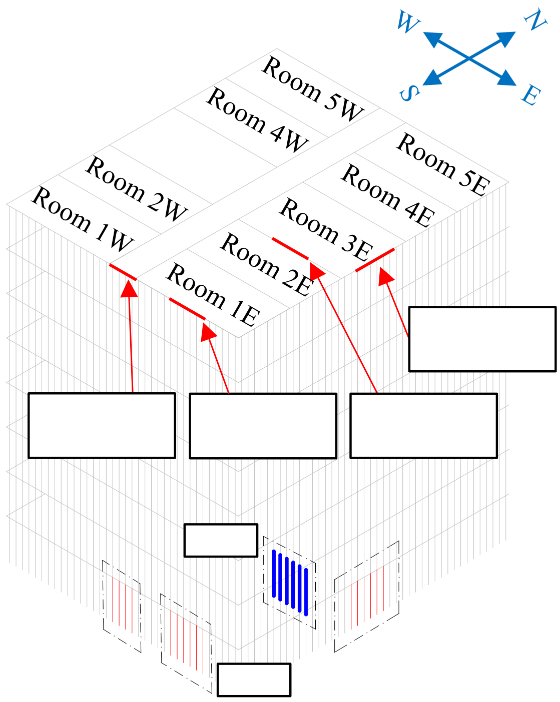

Figure 33. FE model of analysis Cases 1-4

The DIFs for cases with stud removal on the ledger are higher than those for cases with stud removal on the joist. A value of 1.8 is proposed for safety considerations.

Table 6. Summary of the FE analysis of four cases

Case	Critical stud	R_u (kN)	DIF
Case 1	C1SL1	16.3	1.63
Case 2	C2SL2	16.1	1.77
Case 3	C3W11W1	52.8	1.81
Case 4	C4W3W1	65.1	1.80

5.5 Effect of stud wall removal time on DIF

Extreme events, such as car crashes, explosions, and fires, can lead to the removal of studs. In the case of car crashes and explosions, the studs are abruptly removed within a short time, which is consistent with the previous case analysis where the removal time, t_r = 0.003s, results in a ratio of removal time to natural period (t_r/T_n) of 1%. In contrast, in fire scenarios, the studs gradually lose functionality over a longer period. Therefore, it is important to investigate the DIF under varying stud removal times. Theoretically, in elastic single degree of freedom system, the relationship between DIF and t_r can be calculated by

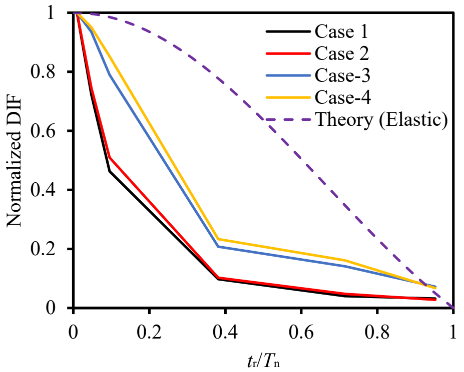

Figure 34. DIF with different stud removal time

$$\frac{u_o}{(u_{st})_o} = 1 + \frac{\left|\sin(\pi t_r / T_n)\right|}{\pi t_r / T_n} \tag{9}$$

in which u_o denotes the amplitude of oscillation and $(u_{st})_o$ denotes the static deformation for the building after stud wall removal.

However, due to the plasticity and non-linearity present in the complex LGS building, the relationship may differ from that expressed in Eq. (9). Figure 34 shows the relationship between the normalised DIF and t_r/T_n-ratio for all four cases, in which the normalised DIF is calculated as

$$\text{Normalized DIF} = \frac{\text{DIF} - 1}{\text{DIF}_{t_r=0} - 1} \tag{10}$$

in which $\text{DIF}_{t_r=0}$ is the DIF when stud removal time is zero.

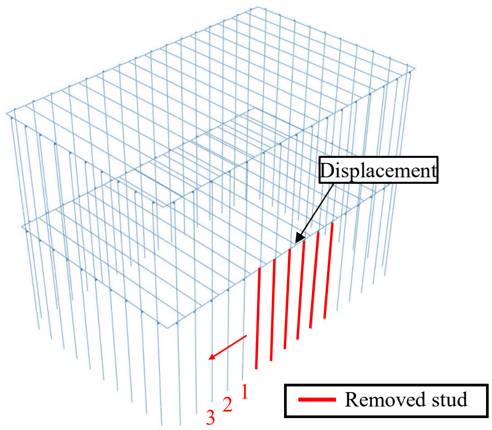

Figure 35. FE model for floor and plasterboard

As shown in Figure 34, the actual DIF is lower than the value calculated by Eq. (9). The DIF decreases rapidly as the t_r/T_n-ratio increases, particularly when this ratio is below 0.4. After the t_r/T_n-ratio exceeds 0.4, the normalised DIF stabilises at relatively low values, all below 0.22.

5.6 Effect of floor and plasterboard

The detailed model incorporating the floor and plasterboard is analysed in this section. Due to the complexity of the FE models of floor and plasterboard, a two-story building with the stud wall removal on ledger is analysed, as shown in Figure 35. The FE model (1) without floor and plasterboard, (2) with floor, and (3) with plasterboard, are referred to as “Original”, “Floor”, and “Plasterboard”, respectively. The REDtongue panels are used for flooring, with screws spaced at 250 mm intervals in the direction perpendicular to the removed stud wall, and 500 mm intervals in the directions parallel to the removed stud wall. Each REDtongue panel measures 750 mm x 2000 mm, while smaller panels at the edges have dimensions of 500 mm x 2000 mm, as shown in Figure 36.

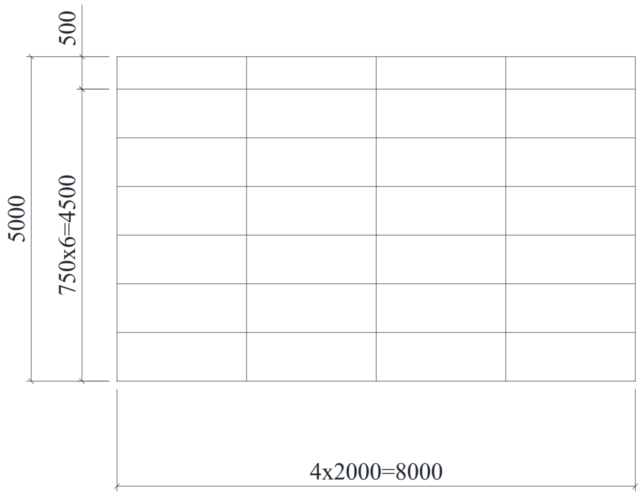

Figure 36. Location of REDtougues

Two layers of 16 mm plasterboards are used in an overlapping configuration, as illustrated in Figure 37 The layers are firmly connected, allowing them to act as a single composite board with a total thickness of 32 mm across the entire wall. The effective width of this composite board corresponds to the full width of the stud wall: 5000 mm for walls perpendicular to the removed stud and 8000 mm for walls parallel to the removed stud. The detailed finite element (FE) modelling methodology and corresponding results are presented in Appendix C.


Figure 37. Schematic of two layers of plasterboards

Table 7 presents the maximum axial forces in each stud surrounding the removed studs, with the nomenclature shown in Figure 35. Both the Original and Floor configurations show similar load distributions among the three studs adjacent to the removed ones. Most of the load is transferred to Stud 1, while only minor loads are distributed to Studs 2 and 3. This similarity is due to the commonly used floor material's specific size, which is insufficient to cover the entire level. The discontinuity of the floor prevents effective load transfer, thereby minimally influencing load redistribution. The load cannot be transferred continuously through floor under such case. In contrast, the plasterboard configuration significantly affects load redistribution due to its continuous coverage across the entire wall. The axial force (R_u) in Stud 1 is 11.8 kN, approximately 7 kN lower than in the Original and Floor cases. Conversely, Studs 2 and 3 experience relatively higher loads, about 1.7 kN and 2.3 kN more than those in Original and 'Floor,' respectively. Additionally, the plasterboard configuration results in lower displacement, indicating its effective constraint on the studs, which helps to restrain the structural movement. In conclusion, the plasterboard's continuous nature effectively reduces the maximum load in the critical stud, enhancing the structural robustness.

Table 7. Summary of the FE analysis of investigating the effects of floor and plasterboard

Case	R_u (kN)			Displacement (mm)
	Stud 1	Stud 2	Stud 3	
Original	18.9	5.2	3.2	6.1
Floor	19.4	5.3	3.3	5.8
Plasterboard	11.8	7.0	5.6	2.4

6. DESIGN RECOMMENDATIONS AND WORKED EXAMPLE

6.1 Introduction

This section provides design recommendations for the proposed new connection aimed at enhancing structural robustness. It also outlines guidance for calculating force redistribution following stud wall removal, using the Alternate Path method. A design example is included after each method to illustrate the application of the recommendations. Details are shown in the following sections.

6.2 Mechanical model for designing tying force (TF method)

Design capacity of membrane force

In JBPC, the BP is the only element bridging two horizontal members, thereby reasonably regarding its tensile capacity as the capacity of membrane force. The BP fails as a result of plate in tension or a group of screws in shear. Hence, the capacity of membrane force is calculated as

$$R_m = \min(N_t, V_w) \tag{11}$$

in which N_t is design tension capacity of BP, and V_w is the design shear capacity of a group of screws.

The design tensile capacity of the connected element is specified in AS 4600 (2018), as calculated by

$$N_t = A_n f_u \tag{12}$$

in which A_n is the net cross-section area, and f_u is the ultimate stress.

The capacity of a group of screws is assumed as the sum of the design capacity of each individual screw:

$$V_w = \sum V_s \tag{13}$$

in which V_s is the design capacity of each screw, which is provided in AS 4600 (2018), as calculated by

$$V_s = \min(V_b, V_{ss}, V_{fv}) \tag{14}$$

in which V_b, V_{ss} and V_{fv} are design capacities of titling and bearing, screw in shear, and screw limited by end distance, respectively, detailed in Sections 5.4.2.4 to 5.2.5.6 of AS 4600 (2018).

Generally, for a plate with a long distance between centres of two end fasteners, the nonuniform distribution of shear forces are observed among all fasteners, leading to a reduction in the overall strength. There is no established provision for defining the reduction in cold-formed steel. Therefore, the empirical method for bolted hot-rolled steel specified in Eurocode 3 (2024) is adopted for application to cold-formed steel in this study. The method accounts for the reduced capacity by introducing a reduction factor β_{LF}, which is applied to the BP. β_{LF} is calculated as:

$$\beta_{LF} = 1 - \frac{L_1 - 15d}{200d}, \text{ but } 0.75 \le \beta_{LF} \le 1 \tag{15}$$

in which L_1 is the distance between the centres of two end screws in each side of BP, and d is the nominal screw diameter.

Design capacity of vertical load

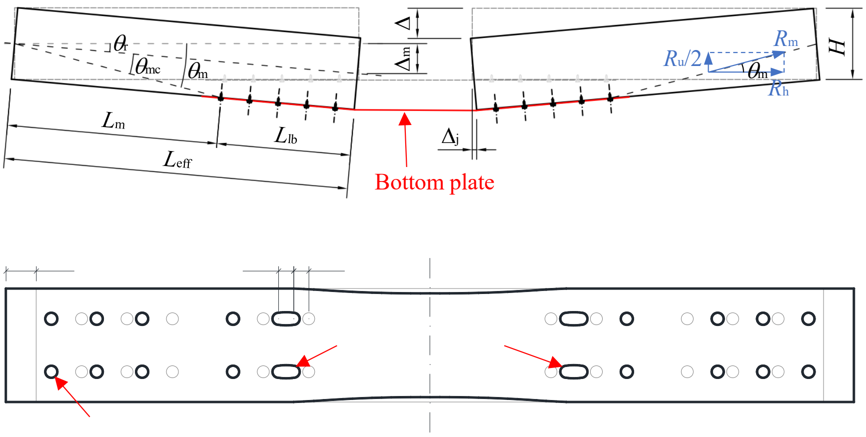

Figure 38. Theoretical model of calculating capacity

For the horizontal members with JBPC, the studs buckled at early stage, eliminating the effect of flexural action. The membrane force is the only force contributed to the capacity, which is calculated using Eq. (11). The membrane force in joist is transferred from the BP and is fully developed from the last screw row, whereby it is reasonable to assume the membrane force is transferred from the last screw row to the rotation centre of joist, as shown in Figure 38(a). Based on equilibrium, the ultimate capacity, R_u, can be calculated as

$$R_u = 2R_m \sin\theta_m \tag{16}$$

in which q_m is the angle of membrane force relative to horizontal, calculated by the rotation of centre line, q_r, plus the angle between membrane force and centre line, q_{mc}:

$$\theta_m = \theta_r + \theta_{mc} \tag{17}$$

q_r relates to the rotation of joist and can be calculated by the horizontal displacement of joist, D$_j$. The expression of q_r is derived from the compatibility of the deformed specimen in Figure 38(a), calculated as:

$$\theta_r = 2\tan^{-1}\left(\frac{\sqrt{-\Delta_j^2 + 2L_{eff}\Delta_j + H^2/4} - H/2}{2L_{eff} - \Delta_j}\right) \tag{18}$$

in which L_{eff} is the effective length of joist, and H is the height of joist.

θ_{mc} can be calculated by the geometry of specimen, through:

$$\theta_{mc} = \tan^{-1}\left(\frac{H/2}{L_m}\right) \tag{19}$$

in which L_m is the distance between end bolt row to rotational centre of specimen, as shown in Figure 38(a).

The joist is significantly stronger than the BP, and thus its elongation under membrane force at the point of BP failure is minimal and is reasonably neglected. Therefore, Δ_j is attributed to the bearing deformation of joist flange (Δ_{bf}), bearing deformation of BP (Δ_{bb}), shear deformation of screw (Δ_s), elongation of BP (Δ_{bp}), and horizontal movement of ledger under membrane force (Δ_{hs}), *i.e.* effect of k_{BC}, as calculated by

$$\Delta_j = \Delta_{bf} + \Delta_{bb} + \Delta_s + \Delta_{hs} + \Delta_{bp} = R_m\left(\frac{1}{k_{bf}} + \frac{1}{k_{bb}} + \frac{1}{k_s} + \frac{1}{k_{BC}}\right) + \Delta_{bps} + \Delta_{bpm} \tag{20}$$

in which k_{bf}, k_{bb} and k_s are the initial stiffnesses of joist flange in bearing, bottom plate in bearing and screw in shear, respectively; Δ_{bps} and Δ_{bpm} are the elongation of the first screw row and the half elongation of BP between the two first screw rows of two sides of BP, respectively, as shown in Figure 38(b).

k_{bf} and k_{bb} relate to the bearing deformation of steel plate, which is consistent to the definition of "bolts in bearing" component in Eurocode 3 (2024). Therefore, the values of k_{bf} and k_{bb} can be calculated based on the equation proposed for the initial stiffness of "bolts in bearing" component, calculated as

$$k_{\mathrm{bf}} \text{ or } k_{\mathrm{bb}} = \sum 12\, k_{\mathrm{d}}\, k_{\mathrm{t}}\, d\, f_{\mathrm{u}} \tag{21}$$

in which $k_t = 1.5t/d_{M16} \le 2.5$; t is the thickness of either joist flange or bottom plate; $k_d = \min(k_{d1}; k_{d2})$; $k_{d1} = 0.25e_1/d+0.5 \le 1.25$; $k_{d2} = 0.25p_1/d+0.375 \le 1.25$; p_1 is the spacing of screws in the loading direction; and e_1 is the distance from the end of the screw to the centre of the closest screw hole.

Similarly, the definition of k_s is consistent to that of "bolts in shear" component, and hence k_s can be calculated by:

$$k_{\mathrm{s}} = \sum \frac{8\, d^2 f_{\mathrm{ub}}}{d_{\mathrm{M16}}} \tag{22}$$

in which d_{M16} is nominal diameter of an M16 bolt, and f_{ub} is ultimate strength of the screw.

Regarding to Δ_{bps}, the strain of net cross-sectional area equals to the strain corresponding to ultimate stress, ε_u, when BP failed by plate in tension. Otherwise, the strain should be calculated according to the average stress of the net cross-section area. Therefore, Δ_{bps} is calculated as

$$\Delta_{\mathrm{bps}} = \begin{cases} \varepsilon_{\mathrm{u}} d & \text{for plate in tension failure} \\ d\left(\dfrac{R_{\mathrm{m}}/A_{\mathrm{n}} - f_{\mathrm{y}}}{E_{\mathrm{h}}} + \dfrac{f_{\mathrm{y}}}{E}\right) \ge d\,\dfrac{R_{\mathrm{m}}/A_{\mathrm{n}}}{E} & \text{for a group of screw failure} \end{cases} \tag{23}$$

in which f_y is the yield stress of plate, and $E_h = (f_u - f_y) / (\varepsilon_u - \varepsilon_y)$, represents the hardening modulus of the material.

Similarly, the strain at the cross-section between the two first screw rows of two sides of BP is calculated according to the average stress of the gross cross-section area. Therefore, Δ_{bpm} is calculated as

$$\Delta_{\mathrm{bpm}} = \frac{g}{2}\left(\frac{R_{\mathrm{m}}/A_{\mathrm{g}} - f_{\mathrm{y}}}{E_{\mathrm{h}}} + \frac{f_{\mathrm{y}}}{E}\right) \ge g\,\frac{R_{\mathrm{m}}/A_{\mathrm{g}}}{2E} \tag{24}$$

in which g is the distance between two first screw rows at two sides of bottom plate, and A_g is the gross area of BP.

The capacity of connection is calculated through Eqs. (16) to (24).

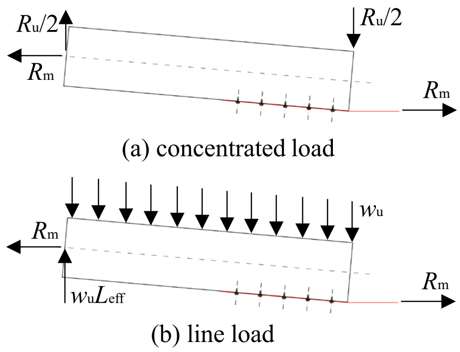

Figure 39. Free-body diagram for both concentrated load and line load

Design capacity of vertical line load

The proposed mechanical model is premised on the assumption that the concentrated load is applied to the ledger flange. To extend the model to practical applicability, the expression of ultimate capacity of line load is derived in this section. According to the equilibrium (Figure 39) and compatibility (Figure 38(a)), the capacity of line load is calculated as:

$$w_u = \frac{2R_m \sin\theta_m}{L_{eff}} \tag{25}$$

With the above-mentioned equations in hand, the design capacities for both concentrated and line loads can be calculated. There are two methods to design the proposed JBPC, as shown in Figure 40.

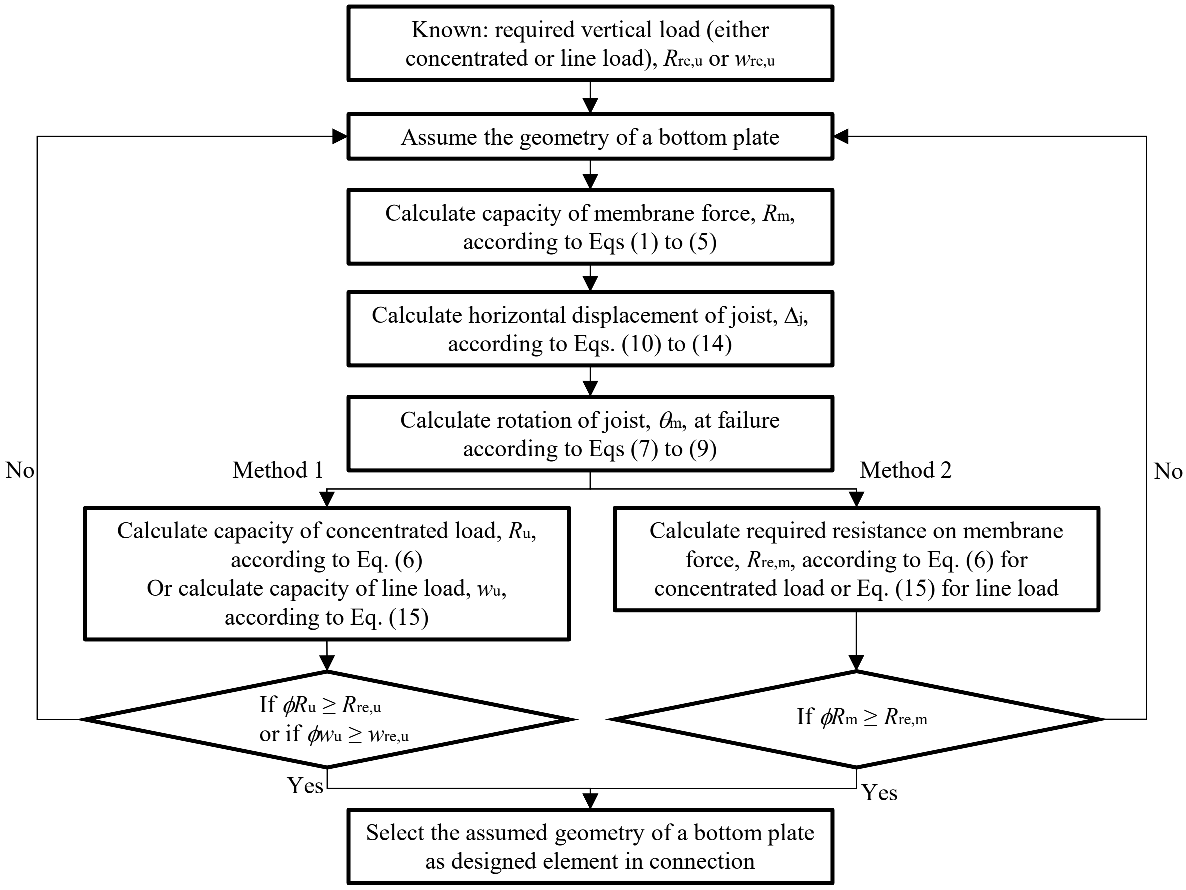

Figure 40. Two methods of designing tying force

Design example

Geometrical parameters:

Joists: L_{eff} = 1500 mm, H = 200 mm.

Bottom plate: W = 75 mm, g = 260 mm, t = 2.4 mm, L_1 = 180 mm, L_m = 1290 mm.

Screw: 12 on each joist, d = 5.5 mm, V_s = 10.6 kN, tensile strength = 17.2 kN.

Material properties:

E = 200,000 MPa, E_h = 500 MPa, f_y = 450 MPa, f_u = 480 MPa, f_{ub} = 17.2×4/5.5^2/π = 724 MPa.

Definition of each geometrical parameters:

1. Design capacity of membrane force

N_t = (75 – 2×5.5)×480 = 73.7 kN, according to Eq. (12).

V_s = 10.6 kN, according to Eq. (14).

V_w = [1 – (180 – 15×5.5) / (200 × 5.5)]×10×10.6 = 115.9 kN, according to Eqs. (13) and (15).

R_m = min (73.7, 115.9) = 73.7 kN, according to Eq. (11).

2. Horizontal displacement of joist, Δ_j

k_{bb} = 10×12×k_d×k_t×5.5×480/1000 = 106.9 kN/mm, in which k_d = min [(0.25×30/5.5 + 0.5), (0.25×30/5.5 + 0.375), 1.25] = 1.25, and k_t = min (1.5×2.4/16, 2.5) = 0.225, according to Eq. (21).

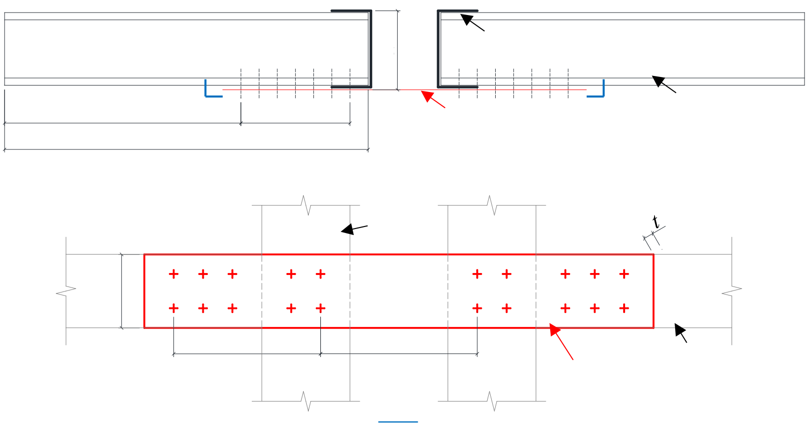

Figure 41. Failure modes of sub-assembly tests

k_{bf} = 12×12×k_d×k_t×5.5×480/1000 = 106.9 kN/mm, in which k_d = min [(0.25×30/5.5 + 0.5), (0.25×30/5.5 + 0.375), 1.25] = 1.25, and k_t = min (1.5×2.4/16, 2.5) = 0.225, according to Eq. (21).

k_s = 12×8×5.5^2×724/16/1000 = 131.4 kN/mm, according to Eq. (22).

$k_{BC} = \infty$.

Δ_{bps} = 0.06×5.5 = 0.33 mm, according to Eq. (23).

$$\Delta_{\mathrm{bpm}} = \frac{260}{2}\left(\frac{73.7/75/2.4\times1000-450}{500}+\frac{450}{200000}\right) = -10.2\ \mathrm{mm} < 260\left(\frac{73.7/75/2.4\times1000}{2\times200000}\right) = 0.27\ \mathrm{mm}$$

, and hence, Δ_{bpm} = 0.27 mm, according to Eq. (24).

$$\Delta_{\mathrm{j}} = 0.27+0.33+73.7\left(\frac{1}{106.9}+\frac{1}{106.9}+\frac{1}{131.4}+\frac{1}{\infty}\right) = 2.54\ \mathrm{mm}$$, according to Eq. (20).

3. Rotation of joist at failure, θ_m

θ_{mc} = tan^{-1}(200/2/1290) = 0.077 rad, according to Eq. (19).

$$\theta_{\mathrm{r}} = 2\tan^{-1}\left(\frac{\sqrt{-2.54^2+2\times1500\times2.54+200^2/4}-200/2}{2\times1500-2.54}\right) = 0.022\ \mathrm{rad}$$, according to Eq. (18).

θ_m = 0.077+0.022 = 0.099 rad, according to Eq. (17).

Method 1:

4. Design capacity of concentrated load, R_u

R_u = 2×73.7×sin(0.099) = 14.6 kN, according to Eq. (16).

5. Design capacity of line load, w_u

w_u = 2×73.7×sin(0.099)/1500×1000 = 9.7 kN/m, according to Eq. (25).

Method 2:

$R_{\mathrm{re,m}} = \dfrac{R_{\mathrm{re,u}}}{2\sin\theta_{\mathrm{m}}}$ according to Eq. (16), or $R_{\mathrm{re,m}} = \dfrac{w_{\mathrm{re,u}}L_{\mathrm{eff}}}{2\sin\theta_{\mathrm{m}}}$ according to Eq. (25).

6.3 Design method of ALP method

Dynamic effects

In both design criteria, UFC (2016) and GSA (2013a), the dynamic effects are considered by the load increase factor, DIF or Ω_{LD}, and dynamic affected area. Based on the FE analysis of the four wall removal cases, the value of Ω_{LD} is proposed as 1.8.

Dynamic affected area is defined as the area with increased gravity loads above removed wall to those bays immediately adjacent to the removed member and at all floors above them. Both provisions provide approximate methods for determining dynamic affected areas in scenarios involving the removal of an entire external or internal wall within one bay. However, the methods omit the distinct effects of stud wall removal on joists versus ledgers, as well as scenarios of removing partial walls. Figure 42 shows the proposed method for defining the dynamic affected area. Since gravity loads are directly applied to the joists, the dynamic affected area is considered as the deformed joists adjacent to the removed stud wall and at all floors above them, shown as the red lines in Figure 42 for both external and internal stud wall removal cases.

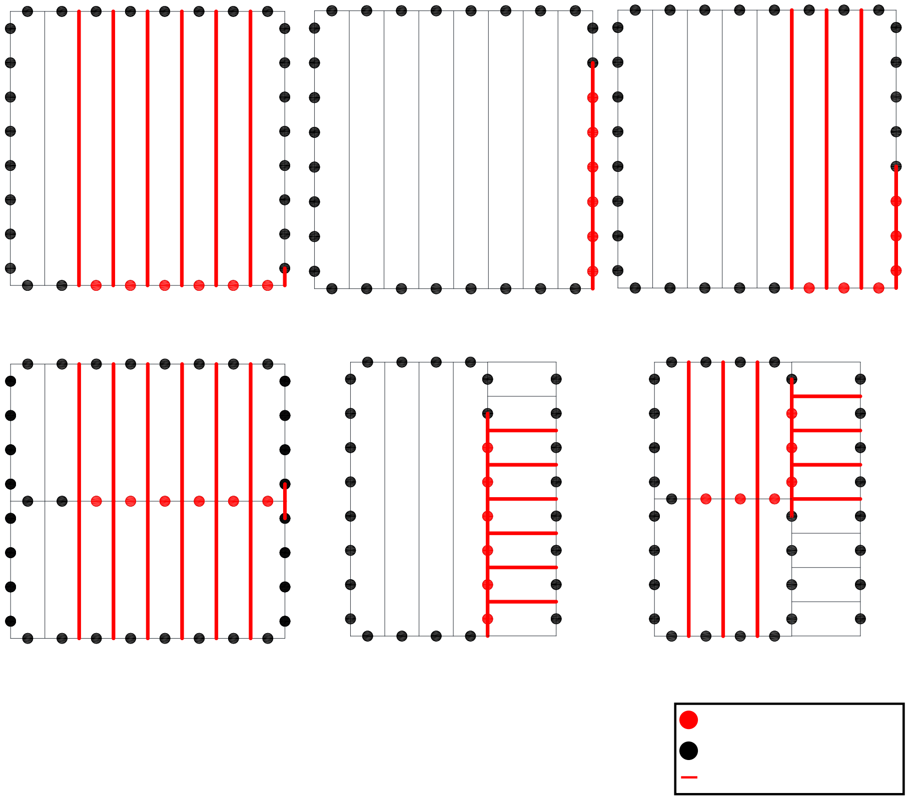

Figure 42. Schematics of dynamic affected area

Tributary area

As the gravity loads are directly applied to the joist instead of floor, the conventional method for calculating tributary area, which attributes the area to the closest stud wall, is not applicable to CFS load-bearing wall buildings. Figure 43(a) shows the tributary area for two critical studs using the conventional method. However, due to the line loads on the joists (indicated in blue) being supported by the adjacent stud instead of Critical stud 2, the conventional method overestimates the size of tributary area. A revised definition of tributary area is proposed to address this issue, as shown in Figure 43(b). In the proposed method, the load in joist is assigned to the closest stud based on the total distance, *i.e.* the sum of distance

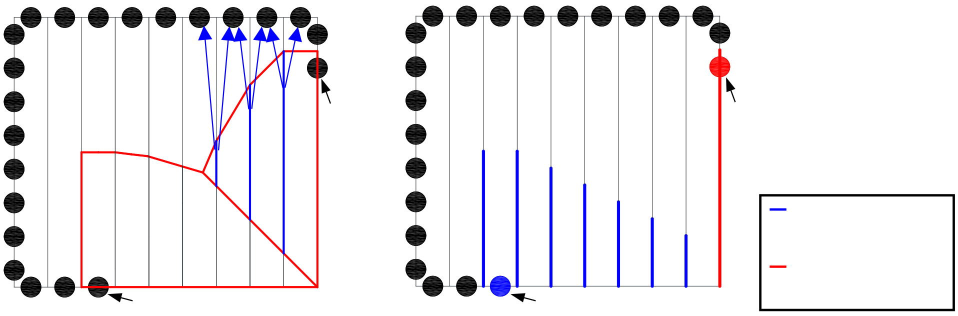

Figure 43. Schematics of conventional and proposed tributary area

in two perpendicular directions, rather than the straight-line distance. Note that if the load has the same total distance to two studs, each stud is assigned half of the load.

In a double-stud wall system, the JBPC connection is the sole element connecting the two bays and is specifically designed to transfer vertical loads using catenary action. Under the tributary area schemes, the load is majorly transferred through bearing rather than catenary action. Since no element transfers vertical loads between two bays, the tributary area does not extend across adjacent bays in the double-wall system.

Calculation method of axial force in stud after stud removal

For each building level (denoted as Level *a*), the design axial force capacity of stud shall be increased to overcome the increased required axial force strength, $R_{u,e,a}$, calculated as

$$R_{\mathrm{u,e},a} = \Omega_{\mathrm{LD}} \sum_{k=a}^{m} w_k L_{\mathrm{t},k} \qquad (26)$$

in which $L_{t,k}$ is the total length of joist within the tributary area for the calculated stud in Level *k*; subscript "*k*" denotes the building level, ranging from *a* to *m*; *m* is the total number of building levels; and w_k is the applied line load on joists in Level *k*.

Validation

Table 8 compares the predicted and FE axial forces in the critical studs for all cases. In all cases, the predicted values are higher than the FE results, ensuring a safe design. Most cases show a prediction/FE-ratio close to one, except for Case 1. The overestimation in Case 1 is due to its DIF of 1.63, which is lower than the proposed value of 1.8. Overall, the proposed hand calculation method for designing buildings against progressive collapse demonstrates high accuracy and low computational cost, making it suitable for practical applications.

Table 8. FE and prediction axial forces in the critical studs for all cases

Case	Critical member	FE (kN)	Prediction (kN)	Prediction/FE
Case 1	C1SL1	16.3	22.4	1.38
Case 2	C2SL1	16.1	16.5	1.02
Case 3	C3W11W1	52.8	56.1	1.06
Case 4	C4W3W1	65.1	72.6	1.12
			Mean	1.14

Design example of Case 3

Loads:

Levels 1 to 7: Q = 1.5 kPa, G = 0.72 kPa

Roof (Level 8): Q = 0.25 kPa, G = 0.42 kPa

Load on joists in Levels 1 to 7: $G + 0.4Q$ = 1.32 kPa

Load on joists in Levels 1 to 7: $G + 0.4Q$ = 0.52 kPa

Dynamic effects:

DIF or Ω_{LD} = 1.8

Dynamic affected area: Figure 44(a)

Tributary area: Figure 44(b)

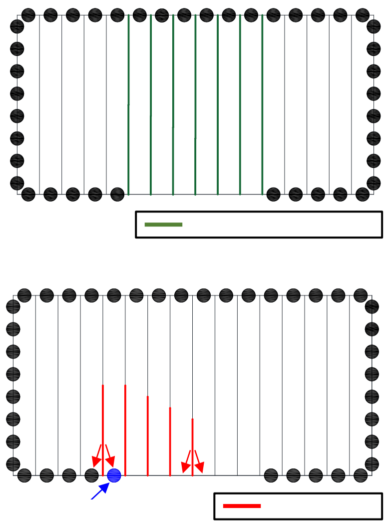

Figure 44. Dynamic affected area and tributary area of the critical stud C3W11W1

For Levels 1 to 7,

Within dynamic affected area: $L_{t,d}$ = (2000 + 1750 + 1500 + 1250/2) / 1000 = 5.875 m

Within static area: $L_{t,s}$ = (2000/2)/1000 = 1 m

For roof (Level 8),

Within dynamic affected area: $L_{t,d}$ = (2000 + 1750 + 1500 + 1250/2) / 1000 = 5.875 m

Within static area: $L_{t,s}$ = (2000/2)/1000 = 1 m

Axial load in C3W11W1

For Levels 1 to 7,

Within dynamic area: $R_{u,e}$ = 1.8 x 1.32 kPa x (500 mm / 1000 mm) x 5.875 = 7.0 kN

Within static area: $R_{u,e}$ = 1.32 kPa x (500 mm / 1000 mm) x 1 = 0.66 kN

For roof (Level 8),

Within dynamic area: $R_{u,e}$ = 1.8 x 0.52 kPa x (500 mm / 1000 mm) x 5.875 = 2.75 kN

Within static area: $R_{u,e}$ = 0.52 kPa x (500 mm / 1000 mm) x 1 = 0.26 kN

Total axial load in C3W11W1 = (7.0+0.66) x 7 + (2.75 + 0.26) = 56.1 kN

7. CONCLUSION AND FUTURE RESEARCH PLANS

7.1 Introduction

The key findings of this project are summarised in this section. While this project aimed to address a broad range of topics related to the robustness design of light-gauge steel buildings, there are several limitations to the work presented. Additionally, several journal articles have been published, and more manuscripts are currently in preparation.

7.2 Conclusion

In this section, robustness of both element and building was investigated for the load-bearing wall light-gauge steel building. The tying force and alternate path methods were used to identify the robustness of element and building, respectively. The brief summary is shown below:

Regarding robustness of element, the strength of ledger-to-joist connection, i.e. the screwed clip angle connection, was evaluated experimental and numerical analyses. Nine cold-formed steel (CFS) ledger-to-joist connections with screwed clip angles were tested under either tension or shear loads to evaluate their behaviour under catenary action and gravity loads, respectively. The test results revealed that using 14-gauge screws significantly enhances connection strength under tension. For connections under shear loads, this configuration led to a more ductile failure mode, specifically clip angle buckling. Numerical analyses were conducted to model the connections, proposing a simplified finite element (FE) modelling approach for screws under both tension and shear loads. Parametric studies investigated various connection configurations to identify the influencing factors on connection strength and ductility. Key findings include:

- The screw drilling direction had a negligible impact on the load response and can be reasonably disregarded.
- Variations in clip angle geometry minimally affected ultimate resistance under tension but significantly impacted resistance under shear forces.
- Connections that failed by screw shear rupture showed that increasing the distance between the screw centre and the clip angle root caused out-of-plane deformation of the clip angle leg. This led to a non-uniform shear force distribution in the screws, reducing ultimate resistance.
- Increasing the clip angle thickness did not enhance connection shear resistance in cases of screw shear failure but did reduce the deformation capacity.
- The location of screws influenced shear resistance in connections that failed by clip angle buckling. Specifically, a greater distance between the first and last screws on one leg resulted in a longer effective shear area width, thereby increasing resistance.

Next, to address the lack of tying force (robustness) between adjacent bays, six sub-assembly specimens were tested, incorporating two newly proposed elements: a stiffener and a bottom plate, to enhance the tying force for effective load transfer. The results showed that the stiffener had a minimal effect on vertical load resistance, whereas the bottom plate significantly enhanced connection strength under vertical loads. Therefore, the bottom plate was proposed as a new element in the joist-to-joist connection to enhance tying force, referred to as the joist-to-joist bottom plate connection (JBPC). A numerical parametric study was conducted using the validated FE model, revealing the following key findings:

- The middle plate, which fills the gap between the joist bottom flange and the bottom plate, had a minor effect on connection capacity. Specifically, the capacity of the specimen with the middle plate was only 4.9% lower than that without it.
- For connections failing due to plate tension, capacity increased as the number of screws decreased. Conversely, for connections failing due to screw shear, capacity decreased with fewer screws due to reduced membrane force resistance.

Based on experimental and numerical results, a hand calculation design method was proposed for determining the tying force of the building for the newly proposed connection. Key components of this design method include:

- Equations for calculating membrane force capacity, based on two typical failure modes: bottom plate in tension and a group of screws in shear.
- A method for calculating the vertical load capacity, establishing a relationship between vertical load and membrane force.
- Consideration of deformations in the bottom plate under tension, screws in shear, and screw holes under bearing to calculate horizontal displacement of the joist at the point of reaching vertical capacity.
- An expression for line load capacity to extend the model's practical applicability.

The proposed model is applicable to the newly developed connection when combined with a strong ledger-to-joist connection and joists that resist bending moments, ensuring failure occurs due to bottom plate tension or screw shear.

The robustness of building was evaluated using a simplified FE model for a newly designed archetype load-bearing wall LGS building. Four distinct stud wall removal scenarios were analysed, and dynamic increase factors (DIFs) were proposed for each scenario with varying stud wall removal times. Based on numerical analysis, a hand calculation approach was developed for designing mid-rise load-bearing wall LGS buildings to resist progressive collapse. This method incorporated dynamic effects by:

- Recommending load increase factors for the removal of stud walls at joists and ledgers.
- Defining the dynamic affected area as the deformed joists adjacent to the removed stud wall, including all floors above them.
- Introducing a definition for the tributary area, where the load on a joist is assigned to the nearest stud based on the total distance (sum of distances in two perpendicular directions).

7.3 Opportunities for further research

Both experimental tests and numerical parametric studies indicate that clip angle buckling is a common failure mode when the connection is subjected to shear. However, no specific design provision exists to predict its ultimate capacity, which may lead to an overestimation of the connection's strength. Further research is needed to investigate the influence of screws locations on the effective width and length of the clip angle, thereby affecting its ultimate buckling capacity.

The proposed joist-to-joist bottom plate connection enhances the tying force between two bays. However, the traditional ledger-to-joist and ledger-to-stud connections are not designed to resist high tension forces induced by catenary action. Therefore, its tension capacity requires further investigation.

Additionally, the observed effect of plasterboard on load redistribution highlights the importance of studying its effects on mid-rise LGS buildings. Hand calculation design provisions should also be developed to account for its influence on load redistribution.

7.4 Manuscripts planned for publication

Two papers have already been published in *Structures*, titled "An experimental study of cold-formed steel connections with screwed clip angle under tension and shear loads" (https://doi.org/10.1016/j.istruc.2024.106908) and "Simplified finite element model for screwed connections with clip angle" (https://doi.org/10.1016/j.istruc.2025.108479). Additionally, two more journal articles are currently in preparation, covering the research presented in Sections 4 and 5, separately.

REFERENCES

2002. AS/NZS 1170. *Structural design actions.* Standards Australia, Sydney.

2005. EN 1993-1-1. *Eurocode 3: Design of steel structures - Part 1-1: General rules and rules for buildings.* CEN, Brussels.

2008. Acoustic detailing for steel construction. *SCI P372.* Ascot, United Kingdom: The Steel Construction Institute.

2010. EN 1993-1-8. *Eurocode 3, Design of steel structures. Part 1-8, Design of joints.* CEN, Brussels.

2013a. GSA. *General services administrfation alternate path analysis and design guidelines for progressive collapse resistacne.*

2013b. ISO 898-1. *Mechanical properties of fasteners made of carbon steel and alloy steel Part 1: Bolts, screws and studs with specified property classes — Coarse thread and fine pitch thread.* Geneva, Switzerland.

2016. Department of Defense (DoD). *UFC 4-023-03: Design of buildings to resist progressive collapse.*

2018. AS 4600. *Cold-formed steel structures.* Sydney, Australia.

2023. ISO 724. *ISO general purpose metric screw threads — Basic dimensions.* Switzerland.

2024. EN 1993-1-8. *Eurocode 3, Design of steel structures. Part 1-8, Design of joints.* CEN, Brussels.

ABEYSIRIWARDENA, T., PEIRIS, M. & MAHENDRAN, M. 2021. Local in-plane strength and stiffness of stud-to-sheathing fastener connections in LSF wall panels. *Thin-Walled Structures,* 160**,** 107383.

ARCURI, D., MAGATELLI, S. & MARTINELLI, P. 2023. Application of the tying force method in the design of alternative load paths in post-and-beam timber structures: A case building. *Journal of Building Engineering,* 78**,** 107577.

AYHAN, D. & SCHAFER, B. W. 2019. Cold-formed steel ledger-framed construction floor-to-wall connection behavior and strength. *Journal of Constructional Steel Research,* 156**,** 215-226.

BAE, S.-W., LABOUBE, R. A., BELARBI, A. & AYOUB, A. 2008. Progressive collapse of cold-formed steel framed structures. *Thin-Walled Structures,* 46**,** 706-719.

BAUCHAU, O. A. & CRAIG, J. I. 2009. *Structural Analysis,* Dordrecht, Springer Netherlands.

BEER, F. P. 2012. *Mechanics of materials,* New York, McGraw-Hill.

BOHARA, R. P., LE, T., THAI, H.-T. & NGO, T. 2024. An experimental study of cold-formed steel connections with screwed clip angle under tension and shear loads. *Structures,* 66**,** 106908.

CAI, K. & YUAN, H. 2023. Testing, numerical and analytical modelling of self-drilling screw connections between thin steel sheets in shear. *Thin-Walled Structures,* 182**,** 110292.

CASTANEDA, H. & PETERMAN, K. D. 2021. Moment-rotation response of cold-formed steel joist-to-ledger connections with variable-finishes in ledger-framed construction. *Journal of Constructional Steel Research,* 176**,** 106396.

CHARNEY, F. A., IYER, H. & SPEARS, P. W. 2005. Computation of major axis shear deformations in wide flange steel girders and columns. *Journal of Constructional Steel Research,* 61**,** 1525-1558.

CODE, N. C. 2020. Handbook: Structural robustness Australia: Australian Building Codes Board.

CRAMER, S. M., FRIDAY, O. M., WHITE, R. H. & SRIPRUTKIAT, G. 2003. Mechanical properties of gypsum board at elevated temperatures. *Fire and materials 2003 : 8th International Conference.* San Francisco, CA, USA: London : Interscience Communications Limited, c2003.

HENCKY, H. 1924. Zur Theorie plastischer Deformationen und der hierdurch im Material hervorgerufenen Nachspannungen. *Zeitschrift für angewandte Mathematik und Mechanik,* 4**,** 323-334.

IZZUDDIN, B. A. & SIO, J. 2022. Rational horizontal tying force method for practical robustness design of building structures. *Engineering Structures,* 252**,** 113676.

LIM, J. B. P. & NETHERCOT, D. A. 2004. Stiffness prediction for bolted moment-connections between cold-formed steel members. *Journal of Constructional Steel Research,* 60**,** 85-107.

LIU, W., DENG, L., ZHONG, W. & YANG, Y. 2023. Parametric study on the pull-out performance of screw connections in cold-formed thin-walled steel structures. *Engineering Structures,* 274**,** 115007.

OBEYDI, M., DAEI, M. & ZEYNALIAN, M. 2020a. Stiffness and strength characteristics of cold-formed steel clip angles subjected to pull-through failures. *Thin-Walled Structures,* 150**,** 106666.

OBEYDI, M., ZEYNALIAN, M. & DAEI, M. 2020b. An experimental study of screw pull-out in load bearing cold-formed-steel clip angles. *Journal of Constructional Steel Research,* 166**,** 105931.

POSSIDENTE, L., FREDDI, F. & TONDINI, N. 2024. Dynamic increase factors for progressive collapse analysis of steel structures considering column buckling. *Engineering Failure Analysis,* 160**,** 108209.

QUAN, G., YE, J. & LI, W. 2021. Computational modelling of Cold-formed steel lap joints with screw fasteners. *Structures,* 33**,** 230-245.

RENTON, J. D. 1991. Generalized beam theory applied to shear stiffness. *International journal of solids and structures,* 27**,** 1955-1967.

SHI, G., SHI, Y., WANG, Y. & BRADFORD, M. A. 2008. Numerical simulation of steel pretensioned bolted end-plate connections of different types and details. *Engineering Structures,* 30**,** 2677-2686.

SIVAPATHASUNDARAM, M. & MAHENDRAN, M. 2018. New pull-out capacity equations for the design of screw fastener connections in steel cladding systems. *Thin-Walled Structures,* 122**,** 439-451.

STRONG-TIE, S. 2023. Catalog: Connectors for Cold-Formed Steel Construction (SSC Steel-Stud Connector).

TEH, L. H. & UZ, M. E. 2015. Ultimate shear-out capacities of structural-steel bolted connections. *Journal of Structural Engineering,* 141**,** 4014152.

VY, S. T. & MAHENDRAN, M. 2022. Design of built-up back-to-back CFS channel compression members sheathed with gypsum plasterboards. *Journal of Constructional Steel Research,* 199**,** 107607.

WATSON, K., AMIRSARDARI, A., PHAM, L., ZHANG, C. & CHOUW, N. 2024. Cold-formed steel for mid-rise construction-conceptual design. Singapore: Springer Nature Singapore.

YANG, F., VELJKOVIC, M. & LIU, Y. 2021. Fracture simulation of partially threaded bolts under tensile loading. *Engineering Structures,* 226**,** 111373.

ZHANG, W., MAHDAVIAN, M., YOUSOF, M. & CHENG, Y. 2018. Testing and design of cold-formed steel clip angles in tension: Pull-over and serviceability. *Thin-Walled Structures,* 124**,** 13-19.

ZHANG, X., RASMUSSEN, K. J. R. & ZHANG, H. 2016. Experimental investigation of locally and distortionally buckled portal frames. *Journal of Constructional Steel Research,* 122**,** 571-583.

ZHOU, J., RASMUSSEN, K. J. R., YAN, S., DEIERLEIN, G. G. & ZHANG, H. 2024. Generalised component method for bolted bearing type connections incorporating block shear failure *Journal of Constructional Steel Research,* 220**,** 108849.

ZHOU, J., THAI, H.-T. & NGO, T. 2025a. Simplified finite element model for screwed connections with clip angle. *Structures,* 74**,** 108479.

ZHOU, J., YAN, S., RASMUSSEN, K. J. R. & ZHANG, M. 2025b. Test-and-FE-based method for obtaining complete stress-strain curves of structural steels including fracture *Journal of Constructional Steel Research,* 25**,** 109095.

APPENDIX A ADDITIONAL INFORMATION FOR SECTION 3

A.1 Material property

The manufacturer's recommended yield strength of the clip angle was 345 MPa. Moreover, three standard dog bone specimens with same geometry were conducted to measure the constitutive relationship of the used G550 CFS coil with the nominal thickness of 2.4 mm. The coupons' geometries and test results are shown in Figure 45. Both ends of the dog-bone specimen were gripped with an Instron universal testing machine (UTM) of 50 kN capacity. The lower end of the specimen was fixed, and a displacement-controlled tensile load was applied from the upper end at a rate of 5 mm/min. Moreover, the displacement was measured using an extensometer with a gauge length of 50 mm. A consistent stress-strain behaviour and failure mode can be observed in each tested specimen. The tensile tests showed the average yield strength and ultimate strength of the selected CFS section were 547 MPa and 576 MPa, respectively. The Young's modulus of the tested G550 CFS coil was 207 GPa.

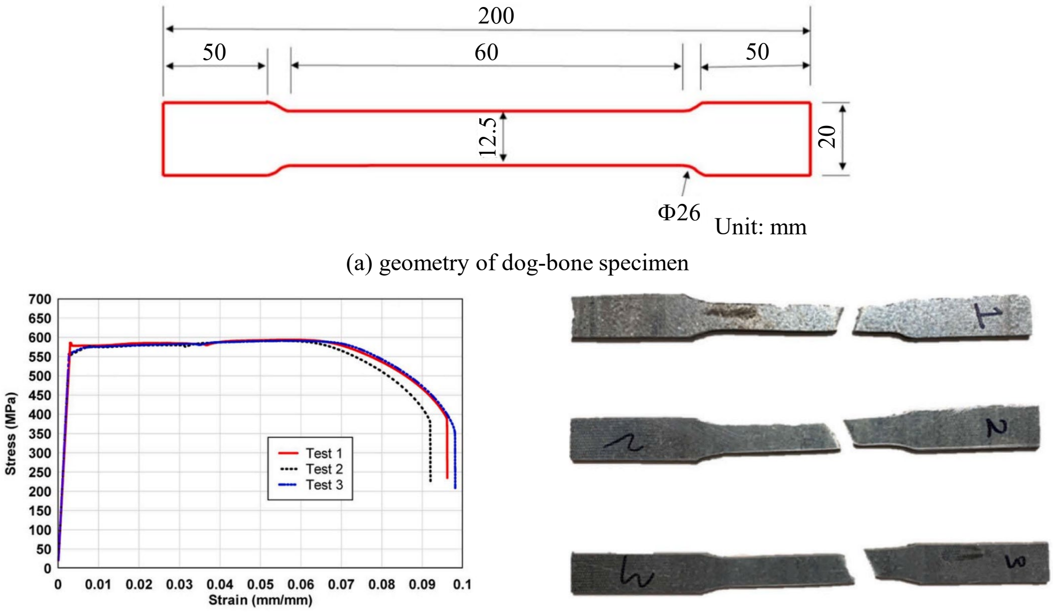

(a) geometry of dog-bone specimen

(b) tested stress-strain curves

(c) failure modes

Figure 45. Tensile test results of the dog-bone specimen

A.2 Simplified FE model of screws

Constitutive law for Axial type connectors.

A key component of the simplified FE model involves characterising the force-deformation response for each Axial-type connector. This section introduces models that determine the force-deformation curves for two types of Axial-type connectors, representing the behaviour of screws under tension and shear. These models also incorporate the failure deformations of each Axial-type connector, which can be used to estimate the ultimate deformation capacity of the connection.

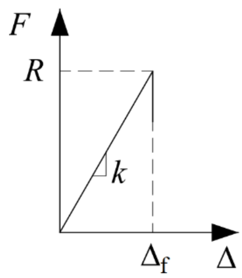

Figure 46. Characteristics of Axial-type connector

Drawing from the findings of Sivapathasundaram and Mahendran (2018) and Liu et al. (2023), the tensile and shear responses of screws exhibit an approximately linear behaviour up to failure. Consequently, a bi-linear curve is adopted to represent their constitutive behaviour. Figure 46 illustrates the key characteristics of this model: *k* is the initial stiffness, R is the resistance and Δ_f is the corresponding deformation (failure deformation).

Axial-type connector for Screw in tension

Screw in tension fails due to, pull-out, pull-over or tension failure, and the resistance (R_t) is defined as the minimum capacity of the three limit states, which is

$$R_{t} = \min\left(R_{ou}, R_{ov}, R_{ts}\right) \tag{27}$$

where R_{ou} is the pull-out resistance; R_{ov} is the pull-over resistance; and R_{ts} is the tensile resistance of screw.

The pull-out capacity has been studied in Sivapathasundaram and Mahendran (2018), and an empirical equation based on 779 pull-out tests including the screw thread outer diameters ranging from 4.67 mm to 6.39 mm and thicknesses of sheets ranging from 0.38 mm to 1.52 mm, which is

$$R_{ou} = 1.65 t_2^{1.3} d^{0.7} f_{u2} \left(\frac{d - d_1}{p}\right)^{0.3} \tag{28}$$

where t_2 is the thickness of the sheet not in contact with the screw head; d is the thread outer diameter; f_{u2} is the tensile strength of the sheet not in contact with the screw head; d_1 is the minimum of thread inner diameter (d*) and drill point diameter (DD); and p is the pitch length. All geometric diameters of screw are shown in The screw hole wall and screw .

The pull-over capacity is introduced in AS 4600 (2018), considering the material and thickness of the sheet in contact with the screw head:

$$R_{ov} = 1.5 t_1 d_{w}^{'} f_{u1} \tag{29}$$

where d'_w is the effective pull-over diameter determined in AS 4600 (2018); t_1 is the thickness of the sheet in contact with the screw head; and f_{u1} is the tensile strength of the sheet in contact with the screw head.

The tension failure of screw occurs in the thread parts, thereby calculating its resistance by:

$$R_{ts} = A_f f_{us} \tag{30}$$

where f_{us} is the tensile strength of the screw; and A_f is the nominal stress area of screw calculating according to ISO 898-1 (2013b), which is

$$A_f = \frac{\pi}{4}\left(\frac{d_2 + d_3}{2}\right)^2 = \frac{\pi}{4} d_f^{\,2} \tag{31}$$

where d_2 is the basic pitch diameter of external thread in accordance with ISO 724 (2023) = d–3H/4; d_3 is the minor diameter of external thread in accordance with ISO 724 (2023) = d–17H/12; H=(d–d*)/2, d_f is the nominal screw diameter.

The stiffness of the screw under tension is given by the expression,

$$k_{\mathrm{st}} = \frac{F}{\Delta_{\mathrm{t}}} = \frac{A_{\mathrm{f}}\sigma}{l_{\mathrm{e}}\varepsilon} = \frac{A_{\mathrm{f}}E}{l_{\mathrm{e}}} \tag{32}$$

where F is the tensile force transferred through screw; Δ_{t} is the elongation of screw under tension; E is the Young's modulus; and l_{e} is the effective screw elongation length, taken as equal to the grip length (total thickness of Sheet 1, t_1, and washers, t_{w}), plus half the sum of the screw head, t_{h}, and the thickness of Sheet 2, t_2, as shown in Figure 47. Notably, the l_{e} is defined based on the definition for the effective length of bolt in tension in Eurocode 3 (2010). The effective length of bolt in tension (2010) is defined as the grip length (total thickness of materials and washers), plus half the sum of the bolt head and the height of the nut. In screw in tension, the Sheet 2 plays the similar rule as nut, thereby replacing height of the nut by the thickness of Sheet 2.

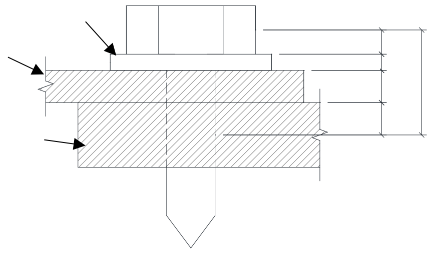

Figure 47. Definition of effective screw elongation length

As demonstrated by the pull-out limit state, the deformation of a screw under tension is not solely due to its elongation; it also results from the plastic deformation of the contact area between Sheet 2 and the screw thread, highlighted by the red-square region in Figure 48(a). The deformed shape of this region is illustrated in Figure 48(b). In this area, the plate and screw are tightly engaged, with the screw thread and the surrounding wall of the threaded hole deforming together, effectively behaving as a unified body. Based on the observed deformation pattern, the deformation of this region can be calculated using:

$$\Delta_{\mathrm{fth}} = \gamma\left(d - d_1\right) = \left(\varepsilon_{12} + \varepsilon_{21}\right)\left(d - d_1\right) \tag{33}$$

where γ is the engineering strain, ε_{12} and ε_{21} are the strain tensor components in the (1,2)-plane.

The equivalent strain of the red area is defined as (Hencky, 1924)

$$\varepsilon_{\mathrm{eq}} = \varepsilon_{\mathrm{sf}} = \sqrt{\frac{2}{3}\varepsilon_{\mathrm{ij}}\varepsilon_{\mathrm{ij}}} = \frac{\gamma}{\sqrt{3}} \tag{34}$$

where $\varepsilon_{\mathrm{ij}}\,\varepsilon_{\mathrm{ij}}$ is the sum of products of strain tensor components, of which, for pure shear in the (1,2)-plane, the only non-zero strains are $\varepsilon_{12} = \varepsilon_{21} = \gamma/2$, and $\varepsilon_{\mathrm{sf}}$ is the pure shear equivalent fracture strain.

In general, $\varepsilon_{\mathrm{sf}}$ is defined as the minimum value obtained from pure shear tests of both sheet material and screw, which is not commonly performed, and therefore, a $\varepsilon_{\mathrm{sf}}/\varepsilon_{\mathrm{tf}}$-ratio was sought for determining $\varepsilon_{\mathrm{sf}}$ in terms of the more commonly available parameter, pure tension fracture strain, $\varepsilon_{\mathrm{tf}}$. An expression of $\varepsilon_{\mathrm{sf}}/\varepsilon_{\mathrm{tf}}$-ratio, which is applicable to the full range of commonly used structural steels, is proposed in Zhou et al. (2025b), calculated as

$$\frac{\varepsilon_{\mathrm{sf}}}{\varepsilon_{\mathrm{tf}}} = 3.4\exp\left(-\varepsilon_{\mathrm{tf}}^{\ 0.7}\right) > 0 \tag{35}$$

Invoking the experimental observations in previous published studies (Sivapathasundaram and Mahendran, 2018, Liu et al., 2023), the resistance of the screw in tension failed by pull-out limit state increases linearly until reaching the ultimate capacity. It is reasonable to assume that the deformation in the red-square region develops linearly until the occurrence of pull-out failure, thereby calculating the final stiffness of Axial-type connector by:

$$k_{\mathrm{t}} = \frac{1}{1/k_{\mathrm{st}} + R_{\mathrm{ou}}/\Delta_{\mathrm{fth}}} \tag{36}$$

where Δ_{fth} is calculated by Eq. (33).

Consequently, the failure deformation of screw in tension can be calculated by:

$$\Delta_{\mathrm{ft}} = R_{\mathrm{ts}} / k_{\mathrm{t}} \tag{37}$$

Expressions for all parameters shown in Figure 46 defining the Axial-type connector for screw in tension have now been obtained, as per Eqs. (27) to (37).

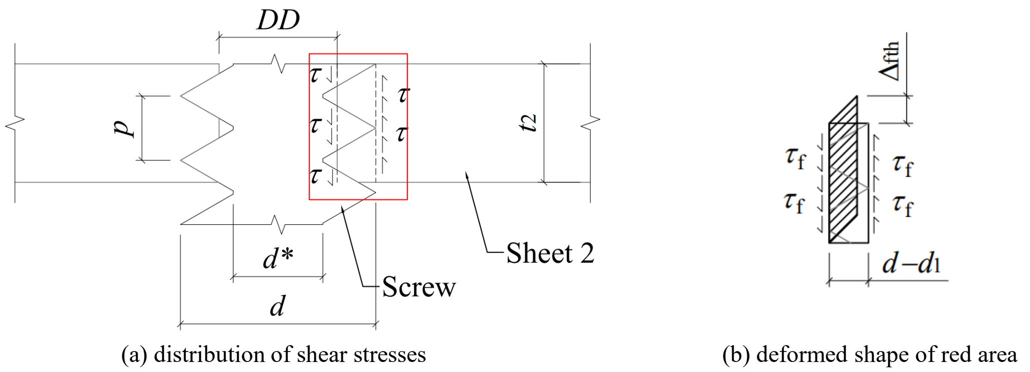

Figure 48. Schematic of stress and strain distribution

Axial-type connector for Screw in shear

Screw in shear fails by tilting (bearing) or shear failure, and the resistance (R_{s}) is defined as the minimum capacity of the two limit states, which is

$$R_{\mathrm{s}} = \min\left(R_{\mathrm{ti}}, R_{\mathrm{ss}}\right) \tag{38}$$

where R_{ti} is the tilting (bearing) resistance; and R_{ss} is the shear resistance of screw.

Based on the provision of AS4600 (2018), the equation of tilting (bearing) resistance depend on the ratio of t_1/t_2. For $t_2/t_1 \leq 1.0$, the tilting (bearing) resistance is taken as the following:

$$R_{\mathrm{ti}} = \min\begin{cases} 4.2\sqrt{t_2^3 d_{\mathrm{f}}}\, f_{\mathrm{u2}} \\ C t_1 d_{\mathrm{f}} f_{\mathrm{u1}} \\ C t_2 d_{\mathrm{f}} f_{\mathrm{u2}} \end{cases} \tag{39}$$

where C is the bearing factor, calculated as:

$$C = \begin{cases} 2.7 & \text{For } d_{\mathrm{f}} / t < 6 \\ 3.3 - 0.1\left(d_{\mathrm{f}} / t\right) & \text{For } 6 \leq d_{\mathrm{f}} / t \leq 13 \\ 2.0 & \text{For } d_{\mathrm{f}} / t > 13 \end{cases} \tag{40}$$

For $t_2/t_1 \geq 2.5$, the tilting (bearing) resistance is taken as:

$$R_{\mathrm{ti}} = \min\begin{cases} C t_1 d_{\mathrm{f}} f_{\mathrm{u1}} \\ C t_2 d_{\mathrm{f}} f_{\mathrm{u2}} \end{cases} \tag{41}$$

For $1.0 < t_2/t_1 < 2.5$, R_{ti} shall be determined by linear interpolation between the minimum values obtained from Eqs. (39) and (41).

The shear resistance of a screw is determined by multiplying the ultimate shear stress by the shear area which is equal to the nominal stress area of the screw:

$$R_{ss} = \tau_{us} A_f = \frac{1}{\sqrt{3}} f_{us} A_f \tag{42}$$

where τ_{us} is the ultimate shear stress, which is taken as 1/√3 times the engineering tensile stress (i.e. τ_{us}/f_{us} = 1/√3) (Teh and Uz, 2015).

The shear stiffness of the screw is influenced by shearing, bending, and bearing effects, all of which contribute to determining the overall initial stiffness. The model that incorporates these three components is represented by three springs arranged in series. According to experimental observations by Cai and Yuan (2023), the screw in shear exhibits a brittle failure mode, with resistance increasing linearly up to failure. Consequently, the initial stiffnesses related to shearing, bending, and bearing are calculated based on the screw's elastic behaviour. Figure 49 illustrates the free-body diagram of a screw under shear. Both ends of the screw are flexible, except where the contact surface restricts the rotation of the screw head or washer. The screw can be idealised as an elastic beam with a roller support, and the shear force and bending moment diagrams are presented in Figure 49. It is important to note that the deformation of the screw in shear differs between Sheet 1 and Sheet 2 due to the unique load distribution each sheet experiences. Accordingly, the stiffnesses related to shear force and bending moment for the screw in Sheet 1 (denoted k_{sf1} and k_{bm1}, respectively) and that within Sheet 2 (denoted k_{sf2} and k_{bm2}, respectively) are calculated as follows:

$$k_{sfi} = \frac{2A_f G}{t_i} \tag{43}$$

$$k_{bm1} = \frac{24EI}{5t_1^3 + 6t_1^2 t_2} \tag{44}$$

$$k_{bm2} = \frac{24EI}{8t_1^2 t_2 + 12t_1 t_2^2 + 3t_2^3} \tag{45}$$

where i=1 or 2 for different part of screw i.e. Sheet 1 or 2, respectively; G is the shear modulus $=E/(1+\upsilon)$; υ is the Poisson's ratio =0.3 for steel; and I is the moment of inertia for screw = $\pi d_f^4/64$.

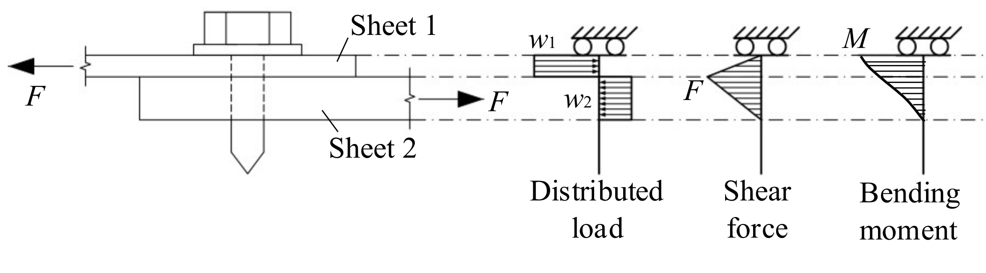

Figure 49. Load, shear force and bending moment diagrams of screw in shear

The schematic representation of bearing deformation for the screw in Sheets 1 (Δ_{br1}) and 2 (Δ_{br2}) is illustrated in Figure 50. The greatest deformation occurs at the interface between Sheet 1 and Sheet 2. The bearing deformation Δ_{bri} , where i=1 or 2 for each part of the screw) can be determined based on the stress distribution along the shaded long fibre shown in Figure 50(b). This stress distribution, within the infinitesimally thin and narrow section of the shaded fibre (with thickness dt and width dw), is depicted in Figure 51. Since dw is infinitesimally small, it is reasonable to assume a uniform stress distribution in the dw-direction. The shear stress distribution along the d_f-direction is typically represented by a parabolic profile, as is common in engineering beam theory (Renton, 1991, Charney et al., 2005). The maximum shear stress (τ_{max}) occurs at the neutral axis, while the stress diminishes to zero at the section ends, as shown in Figure 51(a). Here, F_t and F_b represent the shear forces for the top and bottom circular cross-sections, rather than the forces acting along the shaded fibres. The shear stress distributions along the top and bottom surfaces of the shaded long fibre are expressed as:

$$\tau_{\mathrm{j}}\left(x\right)=\frac{4F_{\mathrm{j}}}{3A_{\mathrm{f}}}-\frac{16F_{\mathrm{j}}}{3A_{\mathrm{f}}{d_{\mathrm{f}}}^{2}}x^{2} \quad (46)$$

where “j” represents either “t” or “b”, corresponding to the top and bottom surfaces, respectively.

Based on the equilibrium, the bearing stress is calculated by:

$$\sigma_{\mathrm{br}}=\frac{dw\left|\int_{-d_{\mathrm{f}}/2}^{d_{\mathrm{f}}/2}\tau_{\mathrm{t}}dx-\int_{-d_{\mathrm{f}}/2}^{d_{\mathrm{f}}/2}\tau_{\mathrm{b}}dx\right|}{dw\cdot dt}=\frac{8}{9}\frac{1}{dt}\frac{d_{\mathrm{f}}}{A_{\mathrm{f}}}\left|F_{\mathrm{t}}-F_{\mathrm{b}}\right|=\frac{8}{9}\frac{1}{dt}\frac{d_{\mathrm{f}}}{A_{\mathrm{f}}}dF\left(t\right) \quad (47)$$

where $dF(t)$ is the force increment for the whole circular cross-section along the screw length direction = $|F_{\mathrm{t}} - F_{\mathrm{b}}|$ related to the infinitesimal thickness (dt) of shaded area, according to the shear force diagram in Figure 49.

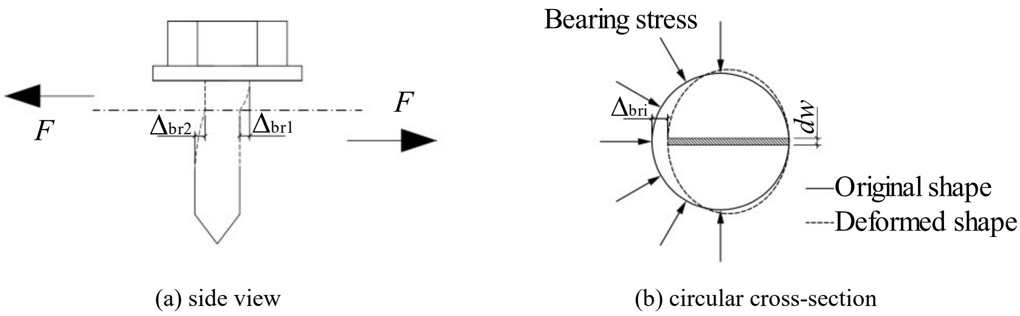

Figure 50. Bearing deformation of the screw

With the bearing and shear stresses distribution in hand, the compression force diagram is shown in Figure 51(b) and is expressed as:

$$CF\left(x,t\right)=dw\cdot dt\cdot\sigma_{\mathrm{br}}-dw\int_{-d_{\mathrm{f}}/2}^{x}\tau dx=dw\left(\frac{8}{9}\frac{dF\left(t\right)d_{\mathrm{f}}}{A_{\mathrm{f}}}-\int_{-d_{\mathrm{f}}/2}^{x}\tau dx\right)=\frac{4}{3}\frac{dF\left(t\right)}{A_{\mathrm{f}}}\left(\frac{d_{\mathrm{f}}}{3}+\frac{4x^{3}}{3{d_{\mathrm{f}}}^{2}}-x\right)dw \quad (48)$$

The compression strain for the small fibre along d_{f} direction is calculated by

$$\varepsilon_{\mathrm{c}}\left(x,t\right)=\frac{\sigma_{\mathrm{c}}\left(x,t\right)}{E}=\frac{CF\left(x,t\right)}{E\cdot dw\cdot dt}=\frac{4}{3}\frac{1}{dt}\frac{dF\left(t\right)}{EA_{\mathrm{f}}}\left(\frac{d_{\mathrm{f}}}{3}+\frac{4x^{3}}{3{d_{\mathrm{f}}}^{2}}-x\right) \quad (49)$$

where σ_{c} is the compression stress along the x direction.

Then, the total bearing deformation for either Sheet 1 or Sheet 2 is

$$\Delta_{\mathrm{bri}}=\int_{0}^{t_{\mathrm{i}}}\left(\int_{-d_{\mathrm{f}}}^{d_{\mathrm{f}}/2}\varepsilon_{\mathrm{c}}\left(x,t\right)dx\right)dt=\frac{8}{9}\frac{Ft_{\mathrm{i}}}{E\pi} \quad (50)$$

The stiffness of screw in bearing for each sheet can be calculated by the shear force (F) divided by the bearing deformation of screw within each sheet (Δ_{bri}):

$$k_{\mathrm{bri}}=\frac{9\pi E}{8t_{\mathrm{i}}} \quad (51)$$

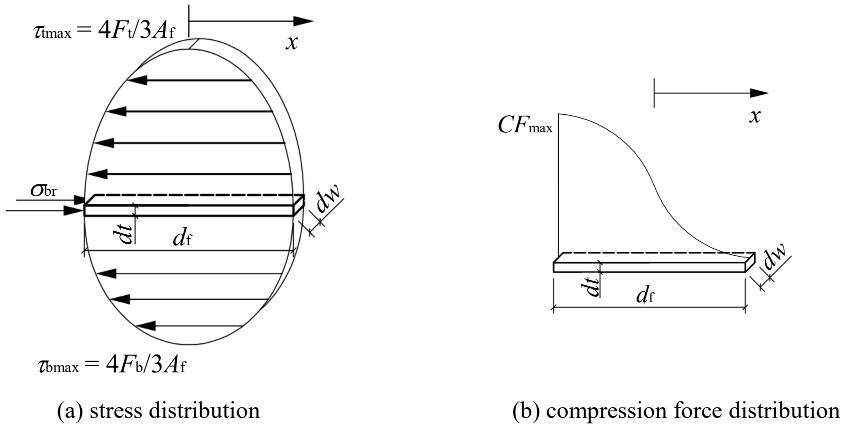

Figure 51. Stress of compression force distributions of the shaded area

The total stiffness of screw in shear within each sheet is calculated by:

$$k_{si} = \frac{1}{1/k_{sfi} + 1/k_{bmi} + 1/k_{bri}} \qquad (52)$$

The fracture displacements for the Axial-type connector for the screw in shear within each sheet is calculated by:

$$\Delta_{fsi} = R_{ssi} / k_{si} \qquad (53)$$

Expressions for all parameters shown in Figure 46 defining the Axial-type connector for screw in screw have now been obtained, as per Eqs. (38) to (53).

A.3 Parametric study of screwed clip angle connections

Connection under tension

Since the effect of the screw drilling direction is negligible, the *specimen out-out* configuration was selected as the benchmark for connection in tension (BMT) in the following parametric study. This study includes 26 specimens with varying geometries, as detailed in Table 9, aimed at investigating the pull-out capacity of the connections and identifying the key influencing factors. The parameters varied in this study include the horizontal leg length (l), out-of-plane length (l_{out}), height (h), thickness (t), number of screws (sn), and screw locations. All screws used were 8-gauge, with an engineering ultimate stress of 800 MPa. In all configurations, four screws were placed on the vertical leg to ensure that failure occurred via pull-out, with a screw pitch set at 20 mm.

To investigate the effect of above-mentioned seven parameters, the models are divided into six categories:

- The level-arm at horizontal leg ranges from 30 mm to 70 mm with 10 mm intervals, and the corresponding models are denoted as T-l-30, T-l-40, T-l-60, and T-l-70.
- The l_{out} ranges from 30 mm to 70 mm with 10 mm intervals, and the corresponding model are denoted as T-lout-30, T-lout-40, T-lout-60, and T-lout-70.
- The h ranges from 30 mm to 70 mm with 10 mm intervals, and the corresponding model are denoted as T-h-30, T-h-40, T-h-60, and T-h-70.
- Four thicknesses of clip angle, 0.75mm, 1.5mm, 2mm and 2.4mm, are investigated to assess the impact of angle thickness, denoted as T-t-0.75, T-t-1.5, T-t-2.0, and T-t-2.4.
- The number of two and three screw numbers are investigated, denoted as sn-2 and sn-3.
- The case of three different screw locations is investigated, denoted as T-sl-2, T-sl-3 and T-sl-4. Note that the BMT is regarding to T-sl-1 in this category.

All specimens exhibited pull-out failure. The ultimate resistance (F) and corresponding deformation (Δ) are presented in Table 9. The ultimate resistance is normalised by pull-out capacity (R_{po}). The Δ is defined as the vertical displacement of the loading plate. Figure 52 illustrates the results of the parametric study in terms of ultimate resistance and corresponding deformation for each parameter. The mean ratio of FE-to-pull-out-ratio for the 26 connections is 1.02 with a CoV of 0.08, indicating that variations in the geometry of the clip angle have a minor effect on the connection's pull-out resistance.

Table 9. Geometries and FE results for all connections in tension

Model	l (mm)	l_{out} (mm)	h (mm)	t (mm)	e_2 (mm)	p_1 (mm)	p_2 (mm)	Screw number	F/R_{po}	Δ (mm)
BMT	50	50	50	1	20	20	20	4	1.03	37.9
T-l-30	30	50	50	1	20	20	20	4	1.09	26.0
T-l-40	40	50	50	1	20	20	20	4	1.17	32.9
T-l-60	60	50	50	1	20	20	20	4	0.96	43.4
T-l-70	70	50	50	1	20	20	20	4	1.03	49.2
T-lout-30	50	30	50	1	20	20	20	4	1.03	37.9
T-lout-40	50	40	50	1	20	20	20	4	1.03	37.9
T-lout-60	50	60	50	1	20	20	20	4	1.03	37.9
T-lout-70	50	70	50	1	20	20	20	4	1.00	38.1
T-h-30	50	50	30	1	20	20	20	4	1.02	34.2
T-h-40	50	50	40	1	20	20	20	4	1.03	36.3
T-h-60	50	50	60	1	20	20	20	4	1.03	37.8
T-h-70	50	50	70	1	20	20	20	4	1.00	38.1
T-t-0.75	50	50	50	0.75	20	20	20	4	1.09	38.3
T-t-1.5	50	50	50	1.5	20	20	20	4	1.04	38.3
T-t-2	50	50	50	2	20	20	20	4	0.94	38.3
T-t-2.4	50	50	50	2.4	20	20	20	4	0.78	37.8
T-sn-2	50	50	50	1	30	40	40	2	1.03	38.3
T-sn-3	50	50	50	1	25	25	25	3	1.03	37.8
T-sl-2	50	50	50	1	14	24	24	4	0.96	38.6
T-sl-3	50	50	50	1	26	16	16	4	0.96	38.6
T-sl-4	50	50	50	1	14	14	44	4	1.03	38.7
								Mean	1.02	
								CoV	0.08	

Figure 52(a) illustrates that the ductility of the connection improves as the level-arm of the horizontal leg increases. This enhancement is attributed to the longer level-arm reducing the screw's constraint on the angle, thereby enhancing ductility.

Figure 52(b) depicts the influence of l_{out} on the connection's ultimate resistance and ductility. The nearly flat curves across the l_{out} range indicate that this parameter has minimal effect on both characteristics.

Figure 52(c) indicates a slight increase in ductility as the level-arm of the vertical leg increases. Similar to the horizontal leg, a longer level-arm reduces the screw's constraint on the angle leg, thereby improving ductility.

Figure 52(d) highlights the effect of clip angle thickness, revealing that the FE-to-pull-out ratio decreases with increasing thickness. This reduction is attributed to the heightened prying force generated within the clip angle's horizontal leg as thickness increases, which diminishes the FE-to-pull-out ratio.

Figure 52(e) shows the impact of screw number on ultimate resistance and ductility. Resistance increases linearly with the number of screws, while ductility remains unaffected.

Figure 52(f) presents the effect of screw placement on connection resistance and ductility. The four different screw arrangements exhibit similar resistance and ductility, which can be attributed to the higher stiffness of the screws relative to the thin sheet (clip angle leg). This allows each screw configuration to fully constrain the plastic hinge near the screw centreline, resulting in consistent resistance and ductility across the configurations.

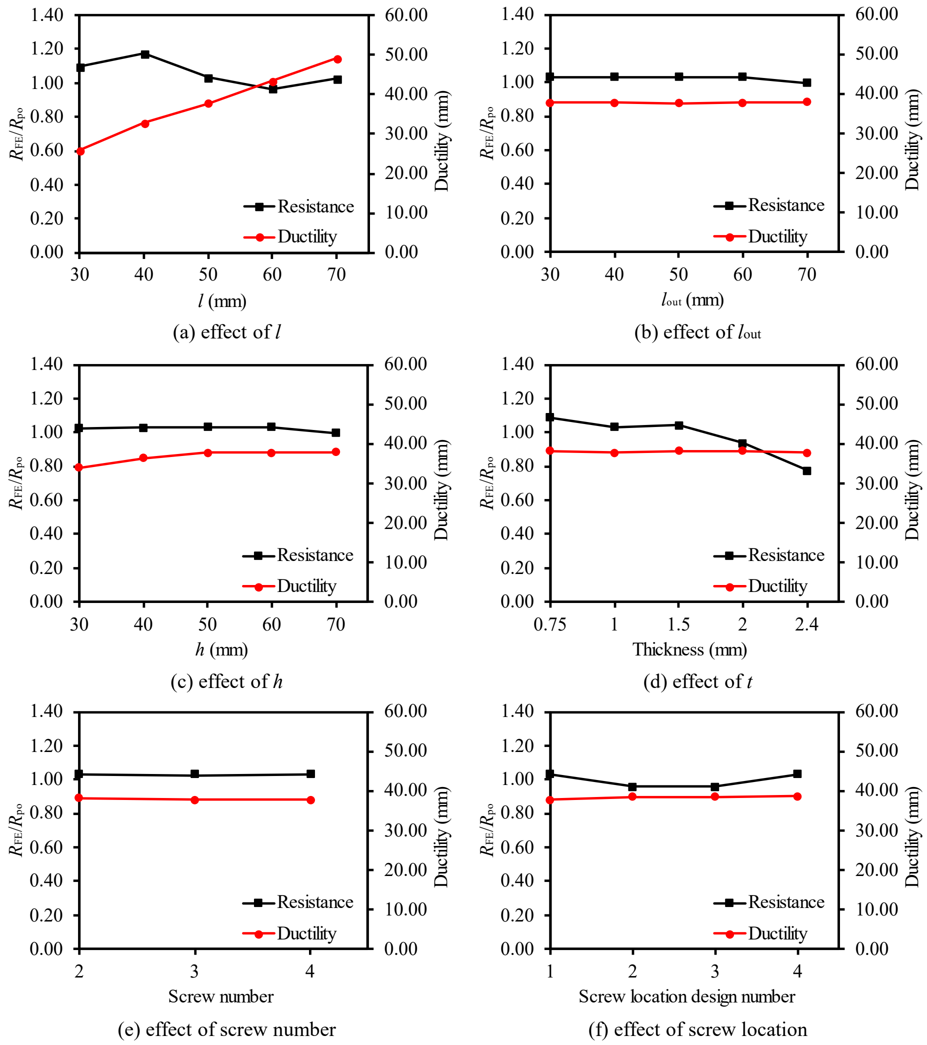

Figure 52. Parametric study results of all connections in tension

Connection under shear

CFS screwed connection under shear forces fails as a result of screw shear rupture and clip angle buckling. The study investigates the effect of clip angle geometry on both limit states in the following two sections.

Connections failed by screw shear failure

The parametric study of CFS screwed connection with clip angle in shear failed by screw shear failure encompasses 16 specimens with varying geometries, as listed in Table 10, aimed to investigate the resistance and ductility of connections and their influencing factors, in which the definitions of geometry parameters are shown in Figure 53. The anchored and loading plates are treated as rigid body, referred to as Plate 1 and Pate 2, respectively. Angle legs contact with Plate 1 and Plate 2 are referred to as Leg 1 and Leg 2, respectively. To isolate the deformation of clip angle and screws, the boundary condition of Plate 1 is set as a fully fixed, while that of Plate 2 is set as a roller, as shown in Figure 53. For all specimens, the length of Leg 1, that of Leg 2, and width of clip angle are 100 mm, 150 mm and 150 mm, respectively. Both plates 1 and 2 have the thickness of 3 mm. Two 8-gauge screws with the engineering ultimate stress of 800 MPa are used in each leg of clip angle.

The parameters to be varied include the a_1, a_2, e_2 (i.e. e_{2t} and e_{2b}) and thickness (t), in which the definitions of all parameters are shown in Figure 53. The benchmark specimen, referred to as BMSs, features an a_1 of 50 mm, a_2 of 75 mm, e_{2t} = e_{2b} of 50 mm and t of 1mm. Excluding BMSs, the specimens are divided into four categories:

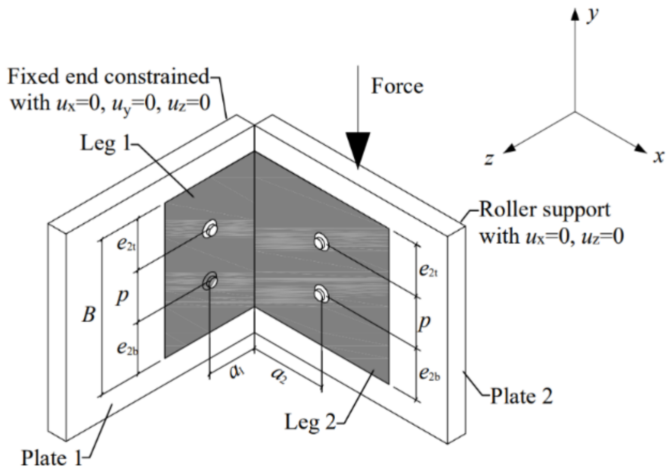

Figure 53. Definitions of geometry parameter for connection in shear

- The a_1 ranges from 30 mm to 70 mm with 10 mm intervals, and the corresponding model are denoted as Ss-a1-30, Ss-a1-40, Ss-a1-60 and Ss-a1-70.
- The a_2 ranges from 35 mm to 65 mm with 10 mm intervals, and the corresponding model are denoted as Ss-a2-35, Ss-a2-45, Ss-a2-55 and Ss-a2-65.
- Four values of e_2 are considered: e_{2t} = e_{2b} = 30 mm, e_{2t} = e_{2b} = 35 mm, e_{2t} = e_{2b} = 40 mm, and e_{2t} = e_{2b} = 45 mm, and the corresponding models are denoted as Ss-e2-30, Ss-e2-35, Ss-e2-40 and Ss-e2-45, respectively.
- Four thicknesses, 1.5mm, 2mm and 2.4mm, are investigated to assess the impact of angle thickness, denoted as Ss-t-1.5, Ss-t-2.0, and Ss-t-2.4.

All specimens exhibited screw shear failure. The ultimate resistance (F) and ductility (defined as complete failure deformation, Δ) are presented in Table 10. The ultimate resistance values were normalised by the screw shear capacity (R_{ss}) calculated using Eq. (42). The deformation was measured as the vertical displacement of rigid Plate 2. Figure 54 illustrates the results of the parametric study, showing the ultimate resistance and ductility for each parameter.

Figure 54(a) depicts the effect of a_1 on connection resistance and ductility. Buckling was first observed at the bottom of Plate 2 near the angle root, causing a brief reduction in resistance. After this initial drop, resistance continued to increase, eventually reaching its peak value, which marked the onset of shear failure. However, due to the buckling, which led to an uneven shear force distribution among the screws, the connections did not achieve the full shear capacity of the screws, with F/R_{ss} ratios around 0.7 for all specimens in this category. Regarding ductility, specimens with longer a_1 provided additional deformation space for the clip angle, resulting in enhanced ductility.

Figure 54(b) illustrates the effect of varying a_2 on connection resistance and ductility. Resistance decreased as a_2 increased, attributed to changes in shear force distribution across the screws. Specimens with shorter a_2 exhibited a more uniform shear force distribution compared to those with longer a_2. Buckling of the clip angle was not observed until a_2 exceeded 55 mm. The ductility across all five specimens showed minimal variation, suggesting that for optimal clip angle design, a_2 should not exceed 55 mm.

Figure 54(c) shows that both the resistance and ductility of the connection decreased as the screw edge distance (e_2) increased. Screws positioned near the edge effectively restrained clip angle deformation, preventing buckling. Therefore, specimens with shorter e_2 exhibited a more uniform shear force distribution compared to those with longer e_2.

Table 10. Geometries and FE results for all connections failed by screw shear failure

Model	a_1 (mm)	a_2 (mm)	e_{2t} (mm)	e_{2b} (mm)	t (mm)	p (mm)	F/R_{ss}	Δ (mm)
BMSs	50	75	50	50	1	50	0.72	1.82
Ss-a1-30	30	75	50	50	1	50	0.70	1.73
Ss-a1-40	40	75	50	50	1	50	0.71	1.78
Ss-a1-60	60	75	50	50	1	50	0.72	1.95
Ss-a1-70	70	75	50	50	1	50	0.73	2.61
Ss-a2-35	50	35	50	50	1	50	0.94	1.63
Ss-a2-45	50	45	50	50	1	50	0.95	1.87
Ss-a2-55	50	55	50	50	1	50	0.92	2.04
Ss-a2-65	50	65	50	50	1	50	0.81	1.87
Ss-e2-30	50	75	30	30	1	90	0.99	2.59
Ss-e2-35	50	75	35	35	1	80	0.88	2.06
Ss-e2-40	50	75	40	40	1	70	0.82	1.93
Ss-e2-45	50	75	45	45	1	60	0.75	1.87
Ss-t-1.5	50	75	50	50	1.5	50	0.68	0.46
Ss-t-2	50	75	50	50	2	50	0.67	0.40
Ss-t-2.4	50	75	50	50	2.4	50	0.66	0.34

Figure 54(d) demonstrates the effect of clip angle thickness, showing a significant reduction in ductility as thickness increases, while resistance remains relatively constant. This behaviour is attributed to the limited deformation capacity of thicker clip angles, where most of the deformation is concentrated within the screw itself. Since shear failure in screws typically follows a brittle mode, increasing the clip angle thickness leads to a direct reduction in the overall deformation capacity of the connection.

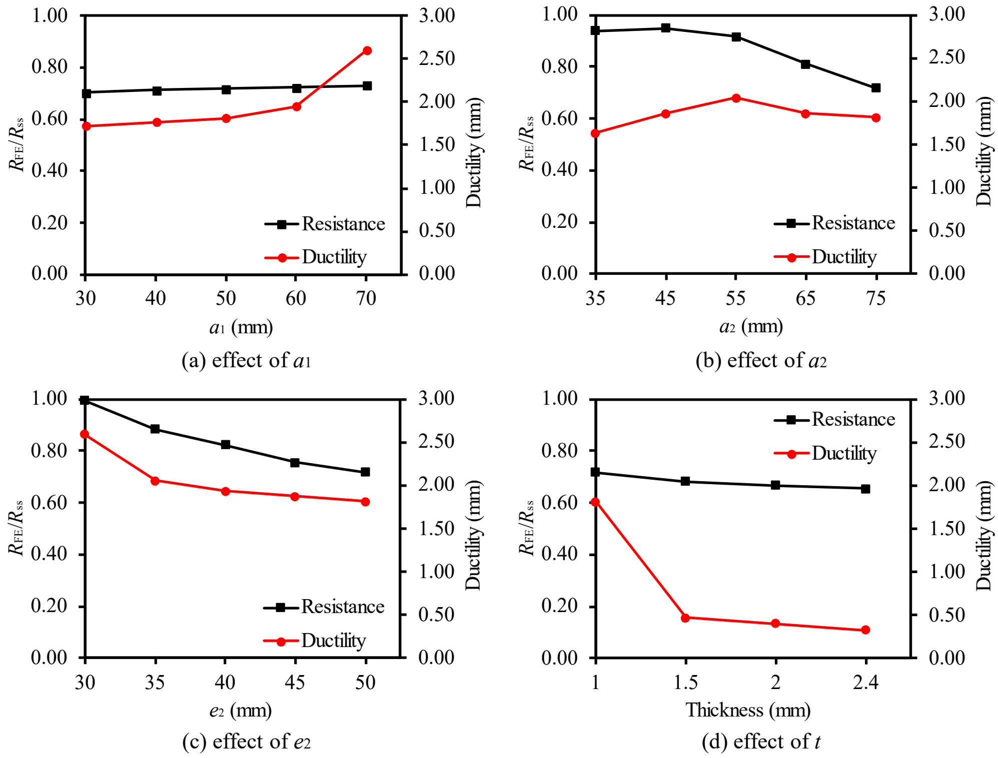

Figure 54. Parametric study results of all connections failed by screw shear failure

Connections failed by clip angle buckling

The parametric study of CFS screwed connection with clip angle failed by clip angle buckling encompasses 16 specimens with varying geometries, as listed in Table 11, aimed to investigate the resistance and ductility of connections and their influencing factors, in which the definitions of geometry parameters are shown in Figure 55. All specimens utilised 8-gauge screws with an ultimate stress of 2000MPa to make sure that the specimen fails by clip angle buckling.

The parameters to be varied include the a_1, a_2, e_2 (i.e. e_{2t} and e_{2b}) and screw number and/or location. The benchmark specimen, BMSb, whose geometry is same as the one used in Section 0. Excluding BMSb, the specimens are divided into four categories:

- The a_1 ranges from 30 mm to 70 mm with 10 mm intervals, and the corresponding model are denoted as Sb-a1-30, Sb-a1-40, Sb-a1-60 and Sb-a1-70.
- The a_2 ranges from 35 mm to 65 mm with 10 mm intervals, and the corresponding model are denoted as Sb-a2-35, Sb-a2-45, Sb-a2-55 and Sb-a2-65.
- Four values of e_{2t} and e_{2b} are considered: e_{2t} = e_{2b} = 30 mm, e_{2t} = e_{2b} = 35 mm, e_{2t} = e_{2b} = 40 mm, and e_{2t} = e_{2b} = 45 mm, and the corresponding models are denoted as Sb-e2-30, Sb-e2-35, Sb-e2-40 and Sb-e2-45, respectively.
- To investigate the effect of screw number and/or location, clip angles featuring either three or four screws per leg were considered. Figure 55 shows the specific screw location for each configuration. Specifically, the specimen with three screws per leg has the same e_{2t} and e_{2b} of 50 mm, and p of 25 mm, referred to as Sb-sn-3. Two four screws specimens with a p of 25 mm are conducted: the one with an e_{2t} of 25 mm and e_{2b} of 50 mm, and another with an e_{2t} of 50 mm and e_{2b} of 25 mm, referred to as Sb-sn-4a and Sb-sn-4b, respectively.

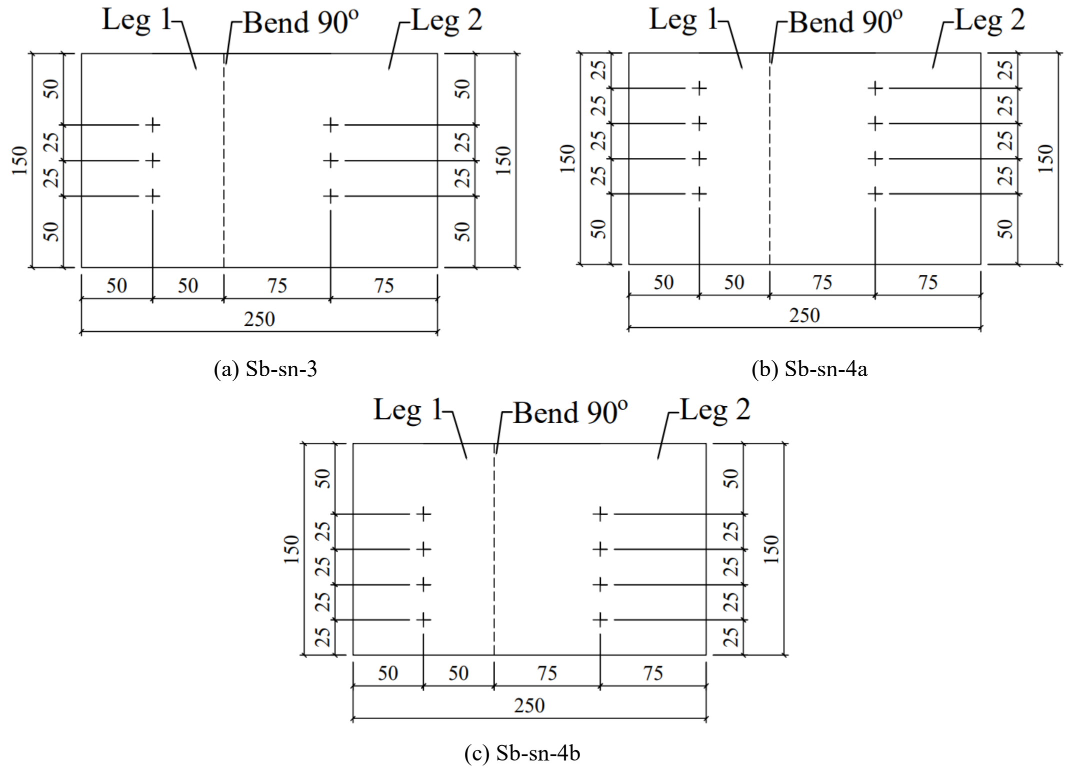

Figure 55. Screw locations for specimens investigating the effect of screw number and/or location

Figure 56(b) displays the effect of varying a_2 on the resistance and ductility of connection, while Figure 57(b) shows their failure modes. The resistance and ductility of specimen decreases as the a_2 increases. The specimen with longer a_2 is slenderer, which buckles easier than the one with short a_2, resulting in lower resistance and worse ductility. As shown in Figure 57(b), the buckling occurs in the comparative slender leg. As evidenced by the specimen with $a_1 > a_2$, i.e. Sb-a2-35 and Sb-a2-45, the buckling occurs in Leg 1. In contrast, for the specimen with $a_1 < a_2$, i.e. Sb-a2-65 and BMb, the buckling occurs in Leg 2. For specimen Sb-a2-55, $a_1 = a_2$, both legs buckles, but Leg 2 has more significant out of plane deformations.

All specimens exhibited clip angle buckling as anticipated. The ultimate resistance (F) and corresponding deformation (Δ) are presented in Table 11, with deformation defined as the vertical displacement of Plate 2. Figure 56 summarises the parametric study results, illustrating ultimate resistance and ductility for each parameter, while Figure 57 depicts the out-of-plane deformation of the two legs at ultimate resistance (failure mode).

Figure 56(a) shows the influence of a_1 on connection ductility and resistance. Both curves remain relatively flat across the full range of a_1. Furthermore, the failure mode, clip angle buckling at Leg 2, was consistent across all specimens with varying a_1, as seen in Figure 57(a), indicating that a_1 does not affect the buckling resistance of Leg 2.

Figure 56(b) highlights the effect of varying a_2 on connection resistance and ductility, with Figure 57(b) illustrating their corresponding failure modes. Both resistance and ductility decrease as a_2 increases. Specimens with longer a_2 are slender and thus buckle more easily than those with shorter a_2, resulting in reduced resistance and lower ductility. As illustrated in Figure 57(b), buckling occurs in the more slender leg: for specimens where $a_1 > a_2$ (e.g. Sb-a2-35 and Sb-a2-45), buckling occurs in Leg 1, while for specimens where a1<a2a_1 < a_2a1<a2 (e.g. Sb-a2-65 and BMb), buckling occurs in Leg 2. For the specimen where $a_1 = a_2$ (Sb-a2-55), both legs buckle, but Leg 2 exhibits more significant out-of-plane deformations.

Figure 56(c) demonstrates that both the resistance and ductility of the connection decrease as the screw edge distance increases. For specimens Sb-e2-30 and BMb, the FE stress contours of Leg 2 are illustrated in Figure 58. The shear-stressed area in specimen Sb-e2-30 is noticeably larger than that in BMb. As a result, Sb-e2-30 has a greater effective shear area width, contributing to its higher resistance.

Table 11. Geometries and FE results for connections failed by clip angle buckling

Model	a_1 (mm)	a_2 (mm)	e_{2t} (mm)	e_{2t} (mm)	t (mm)	p (mm)	F (kN)	Δ (mm)
BMSb	50	75	50	50	1	50	7.87	1.90
Sb-a1-30	30	75	50	50	1	50	7.63	1.81
Sb-a1-40	40	75	50	50	1	50	7.74	1.87
Sb-a1-60	60	75	50	50	1	50	7.88	2.13
Sb-a1-70	70	75	50	50	1	50	7.85	2.22
Sb-a2-35	50	35	50	50	1	50	11.15	3.50
Sb-a2-45	50	45	50	50	1	50	11.36	3.58
Sb-a2-55	50	55	50	50	1	50	10.40	3.54
Sb-a2-65	50	65	50	50	1	50	8.74	2.04
Sb-e2-30	50	75	30	30	1	90	11.31	3.80
Sb-e2-35	50	75	35	35	1	80	10.64	3.53
Sb-e2-40	50	75	40	40	1	70	9.87	3.41
Sb-e2-45	50	75	45	45	1	60	8.73	3.38
Sb-sn-3	50	75	50	50	1	25	9.86	1.02
Sb-sn-4a	50	75	25	50	1	25	14.19	1.26
Sb-sn-4b	50	75	50	25	1	25	12.54	1.33

Figure 56(d) illustrates the impact of screw number and placement. As noted earlier, specimens with a wider effective shear area generally exhibit higher resistance. For example, specimen Sb-sn-4a demonstrates greater resistance than Sb-sn-4b, indicating that the top screw with a shorter edge distance imposes a stronger constraint on the clip angle compared to the bottom screw with the same edge distance. Additionally, while e_{2t} and e_{2b} are identical for Sb-sn-3 and BMb, Sb-sn-3 exhibits approximately 25% higher resistance than BMb. This difference is attributed to the three screws in Sb-sn-3, spaced at a 25 mm pitch, providing more restraint to the clip angle than the two screws in BMb with a 50 mm pitch. As a result, BMb develops a narrower effective shear area, resulting in reduced resistance.

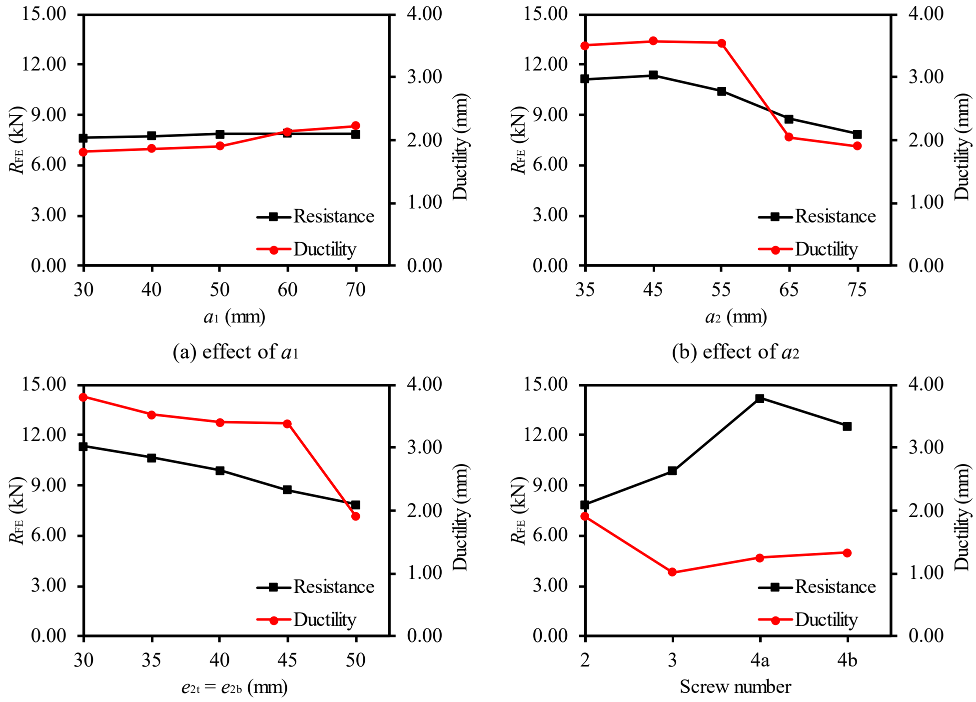

(a) effect of a_1 (b) effect of a_2

(c) effect of e_2 (d) effect of screw number and/or location

Figure 56. Parametric study results of connections failed by clip angle buckling

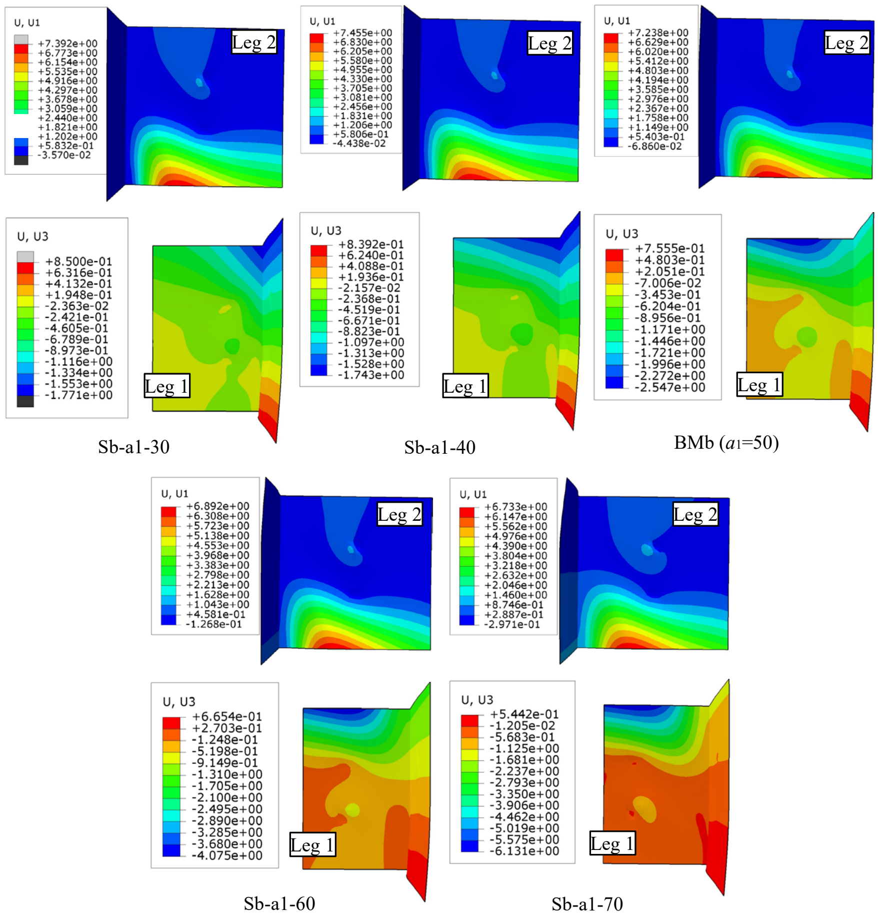

(a) effect of a_1

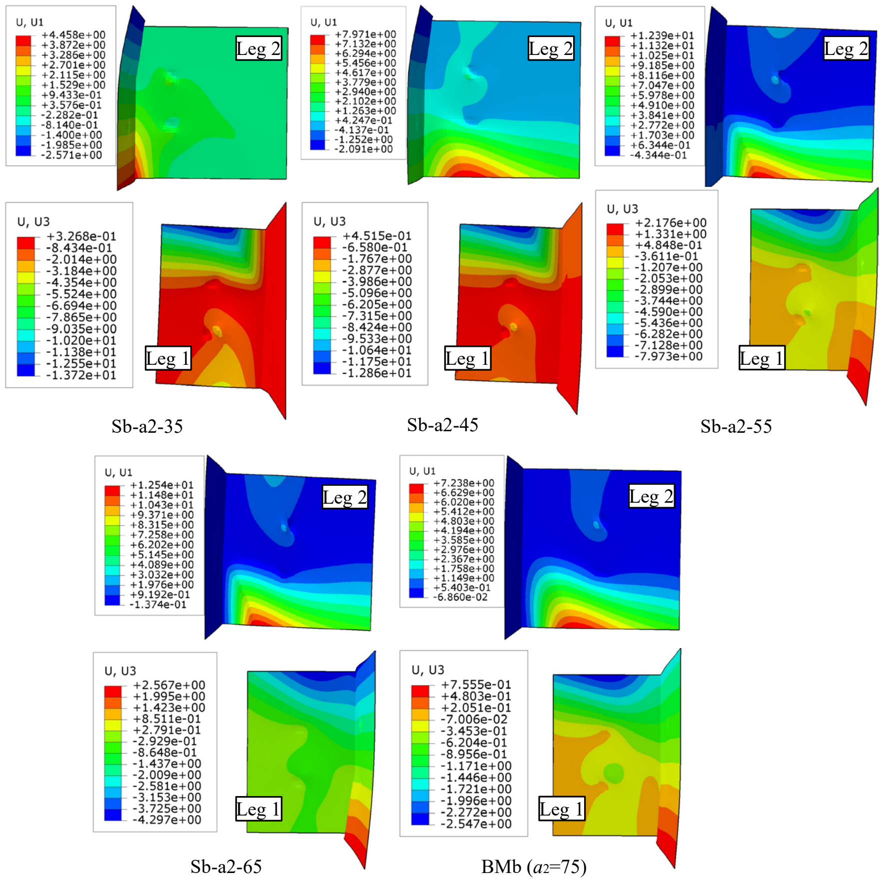

(b) effect of a_2

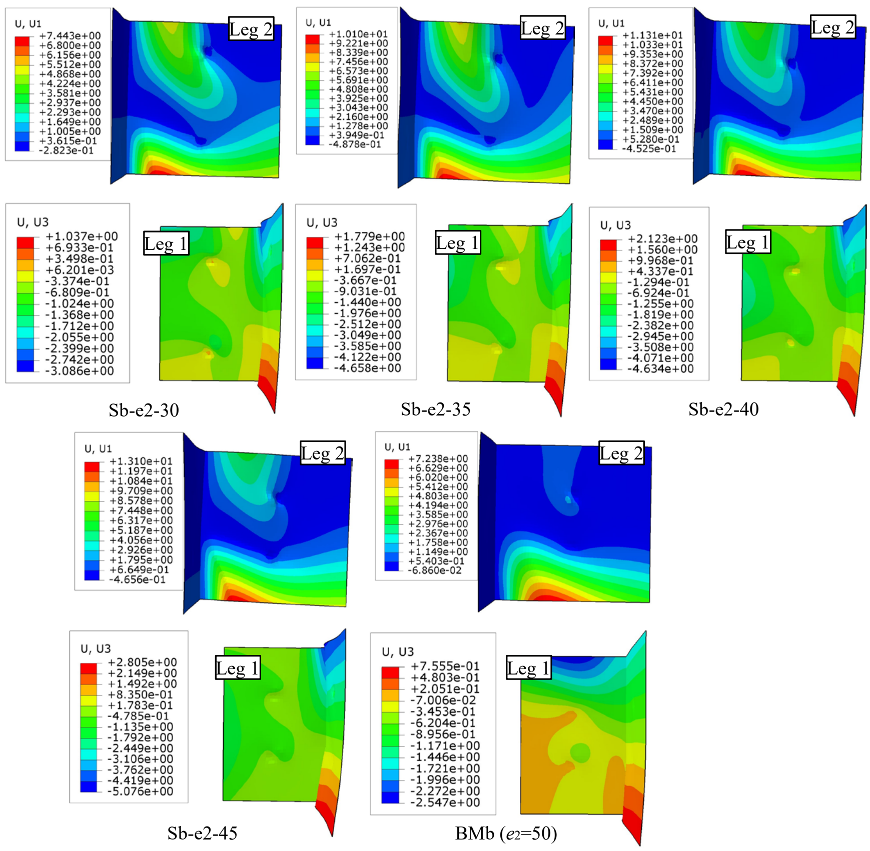

(c) effect of e_2

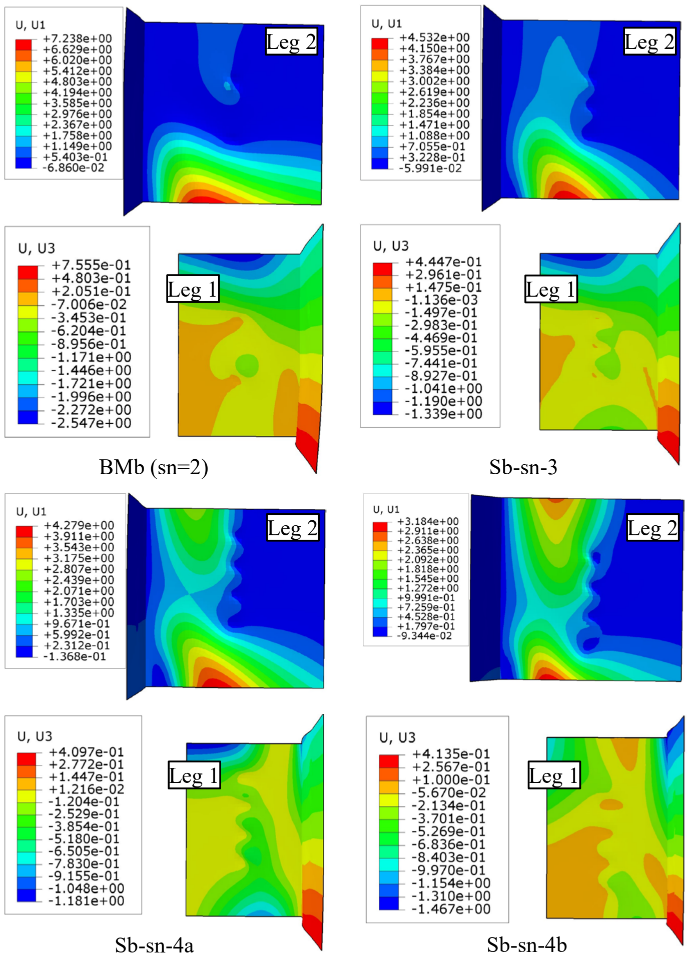

(d) effect of screw number and/or location

Figure 57. Failure modes of connections failed by clip angle buckling

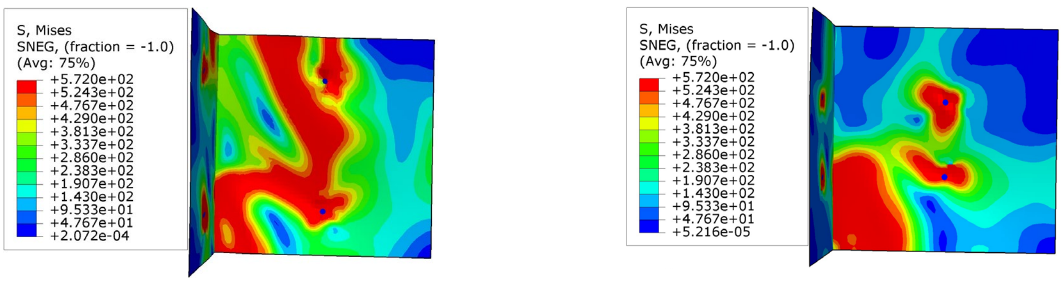

(a) Sb-e2-30 (b) BMb

Figure 58. FE stress contour of Leg 2 for Sb-e2-30 and BMb

APPENDIX B ADDITIONAL INFORMATION FOR SECTION 4

B.1 Parametric study of sub-assembly test

The parametric study encompasses 19 specimens with varying configurations of JBPC, aimed to investigate its behaviour and influencing factors. The detailed characteristics of the specimens are listed in Table 12. The benchmark specimen, referred to as PBM, features as a standard configuration for comparison. Figure 59(a) shows the definitions of BP's geometry parameters. Specifically, the pitch distance along length direction is consistently set at 30 mm, except for the distance between the screw in the joist flange and the screw in the ledger flange, set at 60 mm. Each variable changes solely to isolate its effect, dividing into seven categories:

- The MP fills the gap between BP and joist flange but requires additional material. Therefore, in this category, the specimen PMPN, featuring as no MP, is used to investigate the effect of removing the MP on the specimen's behaviour.
- The screw number in BP controls the limit state of connection, either plate in tension or screw in shear. Four cases are considered with screw number ranging from 4 to 10 with intervals of two, referred to as PS4, PS6, PS8 and PS10, respectively.
- Three widths of BP, W, are considered: 65 mm (PW65), 70 mm (PW70), and 80 mm (PW80).
- The case of three thickness (t), t = 1 mm, t = 2 mm, and t = 3 mm, are investigated to assess the impact of BP thickness, denoted as Pt1, Pt2, and Pt3, respectively.
- Two screw numbers in ledger flange are considered, 2 and 0, referred to as PSL2 and PSL0, respectively.
- Two values of distance between two first screw rows at two sides of BP are considered to investigate the effect of stud size, *i.e.* g = 160 mm (Pg160) and g = 360 mm (Pg360).
- As shown in Figure 59(b), the end ledger deforms horizontally under significant membrane force, F_m, leading to the horizontal displacement at the infection point of joist. The effects of the horizontal displacement are investigated in this category by introducing an axial connector with a stiffness of k_{BC} into the FE model, as shown in Figure 60(a). Given the strong studs in mid- to high-rise buildings, it is reasonable to assume that studs constrain the displacement of ledger, effectively creating a pin boundary condition at the ledger web, as shown in Figure 59(b). Assuming that the ledger undergoes only elastic deformation, its stiffness can be calculated based on Euler-Bernoulli beam theory (Beer, 2012, Bauchau and Craig, 2009) as

$$k_{\mathrm{BC}} = \frac{F_{\mathrm{m}}}{\Delta_{\mathrm{l}}} = \frac{48EI}{P^3} \tag{54}$$

in which Δ_l is the horizontal deformation of ledger under membrane force, E is the Young's modulus =207,000 MPa, I is the moment of inertia of ledger, and P is the spacing of stud.

Given a P of 300 mm, the k_{BC} are calculated for two sizes of ledgers. The weak ledger, a C purlin with a height of 102 mm, a width of 51 mm, and a thickness of 1.5 mm, has a stiffness of 20 kN/mm. The strong ledger, a C purlin with a height of 254 mm, a width of 76 mm, and a thickness of 2.4 mm, has a stiffness of 178 kN/mm. To simplify the FE model and make sure the analysis covers a practical range of k_{BC}, three k_{BC} values of 10 kN/mm, 100 kN/mm, and 200 kN/mm are adopted, referred to as PBC10, PBC100, and PBC200, respectively.

Table 12. Geometries and FE results for parametric study of proposed JBPC.

Specimen	L_{BP} (mm)	W (mm)	g (mm)	t (mm)	Screws at ledger	Screws in BP	k_{BC} (kN/mm)	R_u (kN)	Δ_u (mm)	F_{mu}/N_t
PBM	680	75	260	2.4	4	12	∞	14.4	36.4	1.01
PMPN	680	75	260	2.4	4	12	∞	13.7	25.3	1.02
PS4	380	75	260	2.4	4	4	∞	9.2	75.8	0.49
PS6	500	75	260	2.4	4	6	∞	13.4	66.5	0.75
PS8	560	75	260	2.4	4	8	∞	17.8	69.6	0.99
PS10	620	75	260	2.4	4	10	∞	16.3	53.7	1.00
PW65	680	65	260	2.4	4	12	∞	12.1	29.3	1.02
PW70	680	70	260	2.4	4	12	∞	13.3	32.4	1.02
PW80	680	80	260	2.4	4	12	∞	16.6	43.5	1.01
Pt1	680	75	260	1.0	4	12	∞	6.75	47.6	1.01
Pt2	680	75	260	2.0	4	12	∞	12.8	42.9	1.01
Pt3	680	75	260	3.0	4	12	∞	18.2	34.3	1.02
PSL2	740	75	260	2.4	2	12	∞	14.6	36.0	1.01
PSL0	800	75	260	2.4	0	12	∞	14.6	38.6	1.01
Pg160	580	75	160	2.4	4	12	∞	14.9	36.3	1.01
Pg360	780	75	360	2.4	4	12	∞	15.1	38.5	1.02
PBC10	680	75	260	2.4	4	12	10	21.7	99.4	1.04
PBC100	680	75	260	2.4	4	12	100	15.8	45.0	1.02
PBC200	680	75	260	2.4	4	12	200	15.1	40.6	1.02

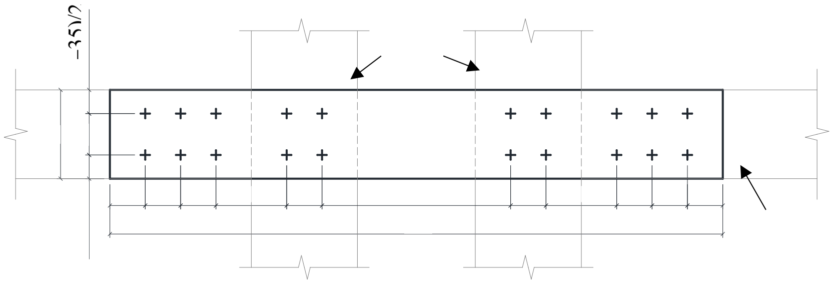

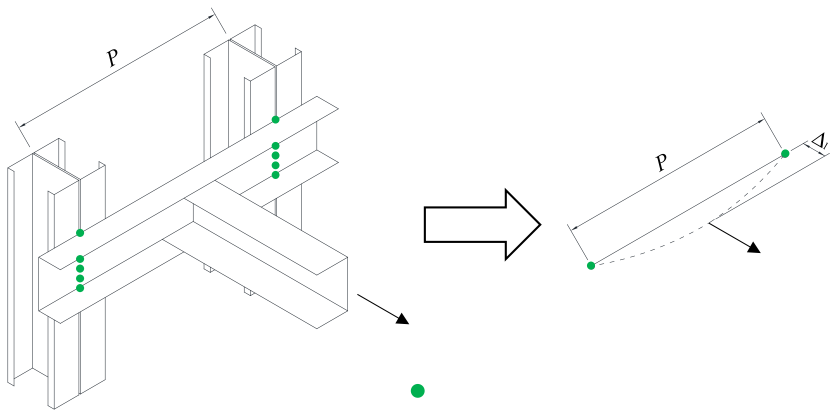

Figure 59. Schematic of BP and end ledger

B.2 FE model for parametric study of sub-assembly test

FE model has been built to specifically isolate the effects of BP, as shown in Figure 60(a). Accordingly, a very strong end LJC is built, *i.e.* employing "Tie" constraint to connect angle legs to either ledger web or joist web. The studs, which are buckled at an early stage and do not affect the capacity, are not modelled to simplify the FE model. Only one pair of joists is modelled with out-of-plane deformations restricted by constraining ledger sides in the *x*-direction. For the two middle LJCs, top flanges of ledger and joist are connected through two screws aligned with the joist length direction, and a Type-1 web connection is adopted, assembling through 7 screws on the joist web and 6 on the ledger web. The length of each joist is set at 1500 mm. MP is employed across all specimens, except for PMPN, to fill the gap between BP and joist flange. All members are assumed to be made from a G450 CFS, and 12-gauge screws are utilised in all specimens.

The irregular geometry of BP in specimen PMPN could not be directly generated in the FE model. To address this, an additional FE model was created to simulate the screw assembling process. The resultant geometry and stress contour, Figure 60(b), were then imported into the main model as depicted in Figure 60(a).

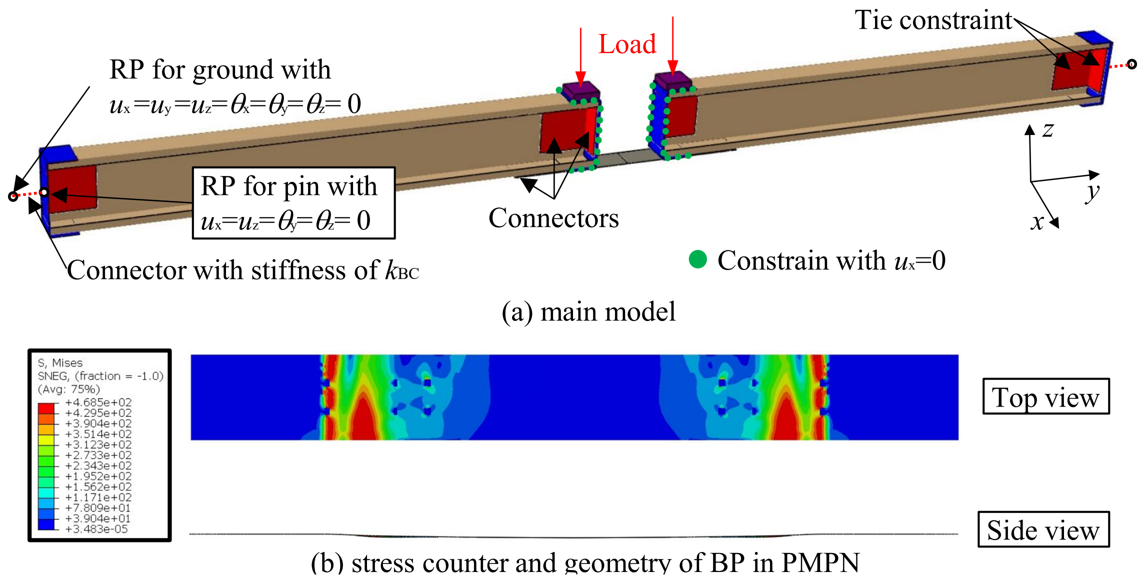

Figure 60. FE model of parametric study for new connection

APPENDIX C ADDITIONAL INFORMATION FOR SECTION 5

C.1 Design of archetype building

In the design, only vertical gravity and wind (leeward) loads are considered, with both determined as per AS1170 (2002). As extreme events occur abruptly, lateral loads, such as wind loads, do not significantly affect the behaviour of the building, which are not considered in the design. The applied live, Q, and dead loads, G, for different area types are concluded in Table 13. The building is located in the city of Melbourne; therefore, the corresponding Wind region is A5, and Terrain category is TC4. The average time interval between exceedances of the wind speed is chosen as 50 years, leading to a maximum wind load, W_u, of 0.31 kPa on the external wall at leeward. The design load is calculated based on the least of 1.35G, 1.2G + 1.5Q, and 1.2G + W_u + ψ_c Q, in which ψ_c = 0.4.

Table 13. Dead load and live load for different area types

Area type	Live load (kPa)	Dead load (kPa)
General	1.5	0.72
Roof	0.25	0.42
Corridors, subjected to wheeled vehicles	5.0	0.72

Floor and roof joists

The floor and roof joists were designed as simple-span members subjected to distributed loads. Figure 25(b) shows the joist bridging and blocking details. The design of joist considers section moment capacity, member moment capacity and shear capacity of web, as depicted in AS 4600 (2018). Two potentially critical joists, referred to as J1 and J2, are analysed, as shown in Figure 61. The design moments of J1 and J2 are 4.8 kNm and 3.4 kNm, respectively, making J1 as the critical joist for bending moment design. The applied shear forces of J1 and J2 are 3.9 kN and 5.3 kN, respectively, making J2 as the critical joist for shear force design. The joist with the greater cross-section is applied to all joists in the building. Based on the applied loads, C20019 joists are selected for both floor and roof joists, spaced at 0.5 m. TN20719 is selected for the ledger to match the size of the joists. Both the joists and ledger are made from G450 steel.

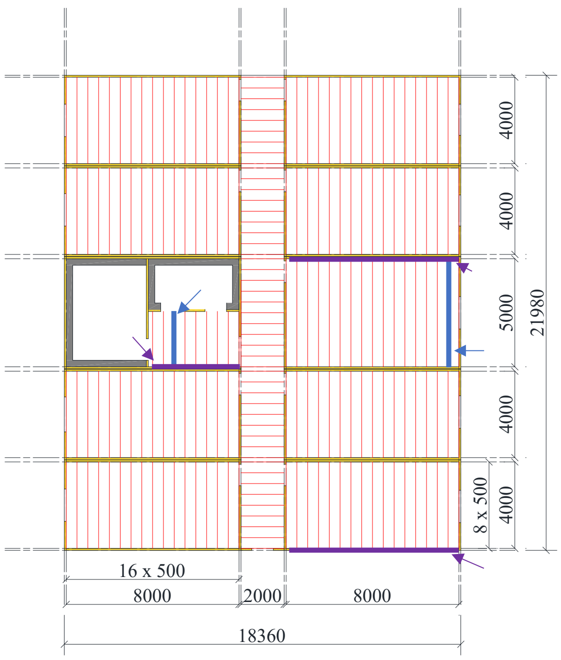

Figure 61 Locations of designed joists and load-bearing walls

Load-bearing walls

Load-bearing walls are present along all wall lines surrounding door and window openings. The studs are sheathed with 16 mm thick gypsum plasterboard on both sides of single walls and on the exterior sides of double walls. The stud-to-board screws are 10-gauge self-drilling screws, spaced at 300 mm intervals. The doors are designed with dimensions of 1 m in width and 2 m in height. Windows are centrally located on the walls and have dimensions of 1.5 m in width and 1.5 m in height. Non-structural load-bearing walls were not designed, as they do not significantly affect the robustness of the building. However, their weight is considered in the design of structural load-bearing walls, with an assumed equivalent load of 0.5 kPa.

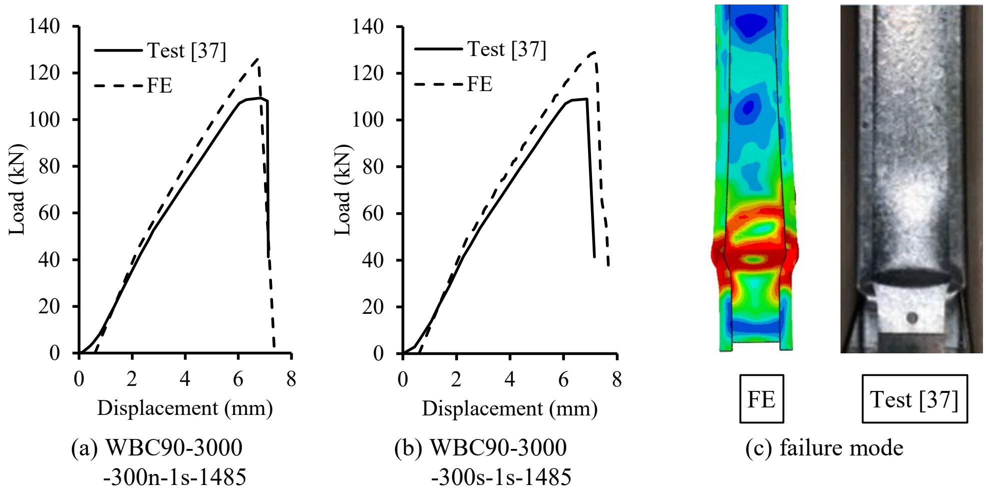

Figure 62. Load-displacement curves and failure modes obtained from tests and FE models

Three potential critical stud walls, referred to as SW1, SW2, and SW3, are analysed, as shown in Figure 61. Based on the wind load, applied loads on joists, and the self-weights of both structural and non-structural members, the applied compression loads (required axial force resistance) for SW1, SW2, and SW3 are calculated as 32.3 kN, 20.9 kN, and 42.5 kN, respectively. SW3 is chosen as the design stud wall, and its size is applied uniformly across the entire level.

The design capacity of stud is increased significantly by the plasterboard (Vy and Mahendran, 2022), leading to potential underestimations in the provisions of AS 4600 (2018). To address this, FE modelling is conducted to calculate the design axial force strength of the stud (N^*) while incorporating the effects of plasterboard, following the method proposed in Vy and Mahendran (2022), and detailed in next section. Note that the boundary conditions of the two stud ends are idealised as pinned. Based on the loads, WBC90×1.00 is selected for Story 1, WBC90×0.75 for Stories 2 and 3, and WBC90×0.55 for Stories 4 to 8. Built-up I-sections, consisting of two channel sections assembled back-to-back, are used for each stud. Studs are spaced at 0.5 m intervals at the midspan between two joists. All studs are made from G550 steel. Additionally, jamb studs, cripple studs, head and sill track framing members used in window and door openings are assumed to be rigid.

Stud capacity calculation

The FE model is built to calculate the design axial force capacity of stud with the effects of plasterboard, following the method proposed in Vy and Mahendran (2022). Two specimens were analysed to validate the FE model, as shown in Figure 62, in which the specimens have plasterboard on both sides of stud. The FE results show a good agreement with the test observations, indicating that the model can be used to calculate the design capacity of stud with effects of plasterboard. The results show an average of 17% overestimation of ultimate capacity; therefore, a reduction factor, ϕ_r, of 0.83 is applied to the capacity of stud.

The critical wall, SW3, is double wall, which is sheathed with plasterboard on single side. Therefore, the constraint is only built for one side of stud flange in FE model. All studs with width of 90 mm are analysed, including WBC90×0.55, WBC90×0.75, WBC90×1.0, WBC90×1.2 and WBC90×1.6. All studs are made by G550 cold-formed steel, except WBC90×1.6 which made by G450 cold-formed steel. The geometries of each stud are concluded in Table 14. The gypsum plasterboard with size of 1200 mm × 3000 mm is used in the designing. Following the method proposed in Vy and Mahendran (2022) with the screw diameter of 4.7 mm, steel Young's modulus of 200000 MPa, i of 0.3 and initial in-plane bowing of (Stud length)/1000, the design axial force capacity, N^*, of all studs are concluded in the last column of Table 14, calculated as

$$N^* = \phi_c \phi_r N_{FE} \quad (55)$$

in which N_{FE} is the capacity of stud calculated by FE model, and ϕ_c = 0.85 according to AS 4600 (2018).

Table 14. Geometry and design resistance of each stud with plasterboard on single side

Stud	Size (depth × flange width × lip width × thickness, unit: mm) of individual stud	Steel grade	N^* (kN)
WBC90×0.55	90×35×8×0.55	G550	20.9
WBC90×0.75	90×35×8×0.75	G550	38.0
WBC90×1.0	90×35×8×1.0	G550	59.8
WBC90×1.2	90×35×8×1.2	G550	77.7
WBC90×1.6	90×35×8×1.6	G450	117.5

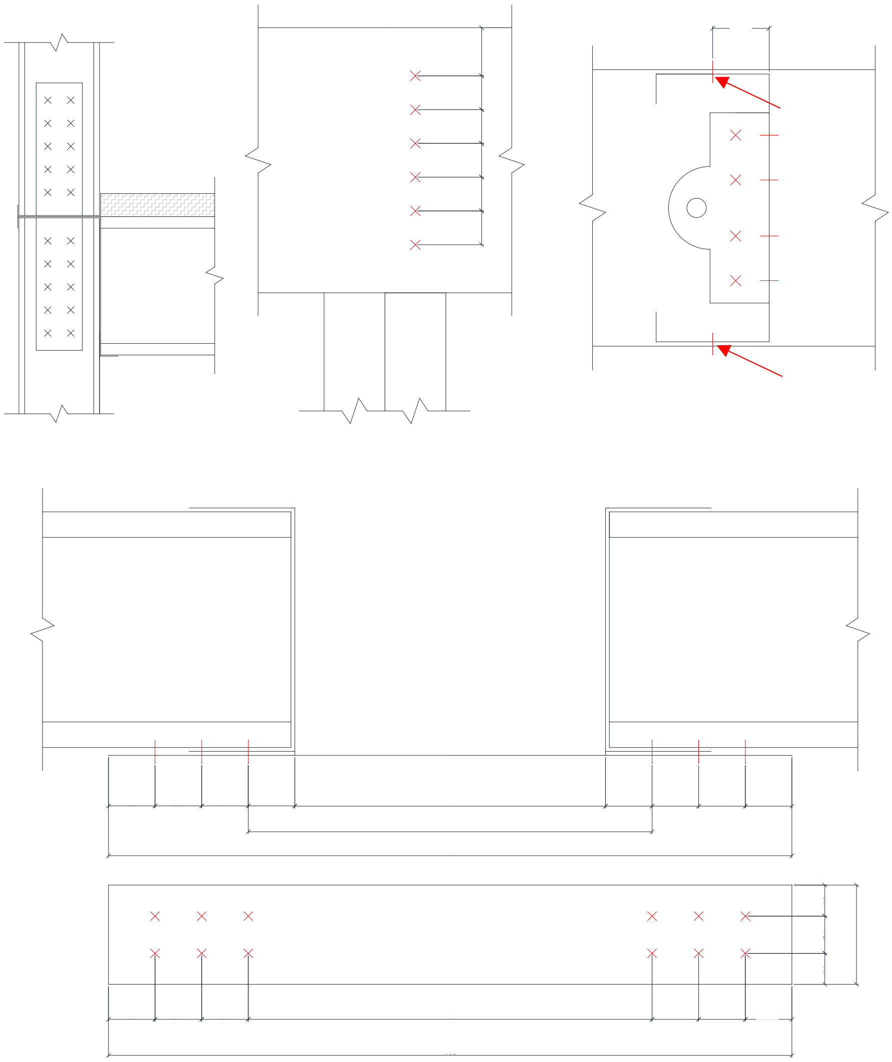

Figure 63. Schematic of each type of connection

Connections

The stud-to-track connection is designed to transfer compression loads from the top to the bottom and is assumed to behave rigidly, as it is the strongest connection among all types of connections. Other connection types are detailed in Figure 63. All connections use 12-gauge self-drilling screws, each with a shear strength of 10.6 kN and a tensile strength of 17.2 kN, as used in Section 4. The SSC4.25 (2023) is used to connect joists and ledgers. The bottom plate in joist-to-joist bottom plate connection is made from G450 steel with a thickness of 1.9 mm, following the design method proposed in Section 4. The L_{eff} is considered as half of the greater of the distances between the centres of walls supporting any two adjacent floor spaces in the joist length direction.

C.2 Simplified FE modelling method

Stud-to-track connection

The stud-to-track connection, shown in Figure 63(a), is designed to transfer loads from one stud to another. The connection is the strongest among all connections, as it is intended to transfer all applied vertical loads. Given that conventional vertical connections are strong enough to resist the increased vertical forces after extreme events (Bae et al., 2008), it is reasonable to assume that the stud-to-track connection behaves rigidly. This can be modelled using a connector element between the two studs, defining as Cartesian and Rotation with rigid translational and rotational responses in all six degrees of freedom.

Ledger-to-stud connection

The ledger and stud are typically connected using multiple screws, as shown in Figure 63(b), resulting in low ductility. Therefore, it is reasonable to assume that this connection exhibits rigid rotational behaviour and infinite stiffness for tension and shear forces up to an ultimate capacity R_{ls}, calculated as

$$R_{\mathrm{ls}} \le n_{\mathrm{sc}} R_{\mathrm{sc}} \tag{56}$$

in which n_{sc} is the number of screws in ledger-to-stud connection; and R_{sc} is the ultimate tensile or shear capacity of a single screw.

Both the rotational and translational behaviours of the connection are modelled using a connector element. The rigid rotational and translational behaviours are defined as Rotation and Cartesian with rigid responses in all six degrees of freedom, incorporating ultimate capacities as per Eq. (56) for tension along the screw length direction and shear in the two directions perpendicular to the screw length direction. The similar method can be found in the modelling of the moment-rotation response of cold-formed steel joist-to-ledger connections (Castaneda and Peterman, 2021).

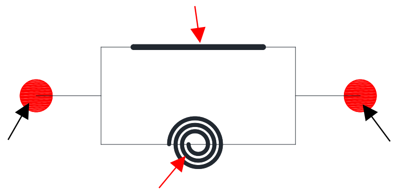

Figure 64. Schematic of simplified model of ledger-to-joist connection

Ledger-to-joist connection

The connector element is also used to model the ledger-to-joist connection, as shown in Figure 63(c). The effects of axial and shear deformations are negligible due to the large ratio between the joist's length (l_j) and height (h_j) (Shi et al., 2008), with a minimum value of 20 for the archetype building. Therefore, the translational behaviour is defined as Cartesian with rigid responses in all three degrees of freedom, as shown in Figure 64. The major-axis rotational behaviour is defined as Rotation with a nonlinear response in the major-axis direction and rigid responses in the other two rotational directions. The moment-rotational behaviour in the major-axis direction can be directly extracted from the FE model with shell elements, following the method proposed in Zhou et al. (2025a). The built FE model should be dominant by bending moment rather than shear force. According to Eurocode 3 (2005), the shear force is considered negligible for the design bending moment resistance of the cross-section if the condition in Eq. (57) is satisfied:

$$V_{\mathrm{Ed}} \le \eta_{\mathrm{V}} V_{\mathrm{Rd}} \tag{57}$$

where η_V = 0.5; V_{Ed} is the applied shear force on cross-section; and V_{Rd} is the shear force resistance of cross-section. The study assumes that the connection follows the same condition as the cross-section, *i.e.* the effects of shear force on the moment-rotation curve of the connection are negligible if

$$V_{\mathrm{c,Ed}} \le \eta_{\mathrm{V}} V_{\mathrm{c,Rd}} \tag{58}$$

where $V_{c,Ed}$ is the applied shear force on connection when connection fails; and $V_{c,Rd}$ is the shear force resistance of connection. Thus, the built FE model, which generates the moment-rotation curve of the connection, must satisfy the condition in Eq. (58).

Joist-to-joist bottom plate connection

In the JBPC connection, a connector element is used to model the behaviours of the bottom plate. The bottom plate is positioned at the bottom flange of the joist, with the effects of the joist and ledger heights incorporated using a rigid bar of length equal to half the height of the ledger web, as shown in Figure 65. A connector element with rigid translational and rotational

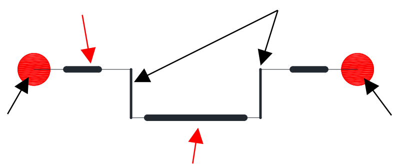

Figure 65. Schematic of simplified model of JBPC

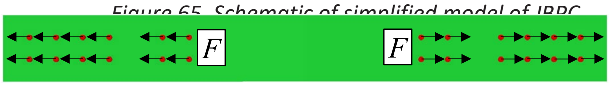

behaviours is applied to connect the rigid bar and joist, defined with rigid Cartesian and Rotation responses in all six degrees of freedom. Additionally, only axial force is transferred through the connection or bottom plate, and the behaviours of the connector element is therefore designed as a nonlinear translational type of Axial.

The load-displacement response for Axial connector element could be obtained using a semi-theoretical method. The horizontal deformation of connection, Δ, includes the deformation of bottom plate (sum of the bearing deformation of screw hole and elongation of plate), Δ_{bp}, bearing deformation of joist flange, Δ_b, and shear deformation of screws, Δ_s, thereby calculating Δ through

Figure 66. FE model for bottom plate

$$\Delta = \Delta_{\mathrm{bp}} + \Delta_{\mathrm{b}} + \Delta_{\mathrm{s}} \tag{59}$$

The relationship between force, F, and Δ_{bp} is directly extracted from the FE model of bottom plate using shell elements, as shown in Figure 66. For a given value of F, Δ_b is calculated by Eq. A.52 in Eurocode 3 (2024):

$$\Delta_{\mathrm{b}} = d\left(\frac{F\sqrt{30}+\sqrt{126\mathrm{n}\,d\;t\,f_{\mathrm{u}}F}}{126\mathrm{n}\,d\;t\,f_{\mathrm{u}}F-30F}\right)^2 \tag{60}$$

where d is the effective diameter of screw; t is the thickness of joist flange; and f_u is the ultimate stress of joist material. Δ_s is calculated as

$$\Delta_{\mathrm{s}} = F / k_{\mathrm{s}} \tag{61}$$

where k_s is shear stiffness of screws, derived based on Eq. A.42 in Eurocode 3 (2024), calculated as

$$k_{\mathrm{s}} = \sum \frac{8\,d^2 f_{\mathrm{ub}}}{d_{\mathrm{M16}}} \tag{62}$$

Members

Beam elements are used for all members, with 2-node linear open-section beam in space elements (B31OS) for open sections, and 2-node linear beam in space elements (B31) for closed sections. The build-up stud is modelled as one single member with a “Generalised” cross-section profile, accounting for the geometric properties of the two C-channels.

The use of beam elements effectively reduces the computational efforts and is also applied to model the stud. However, beam elements cannot capture localised deformations, such as the direct localised effects of plasterboards and shear walls on the stud flanges. To address this limitation, a simplified FE model is proposed to incorporate the effect of both plasterboards and shear walls, as shown in Figure 67(a).

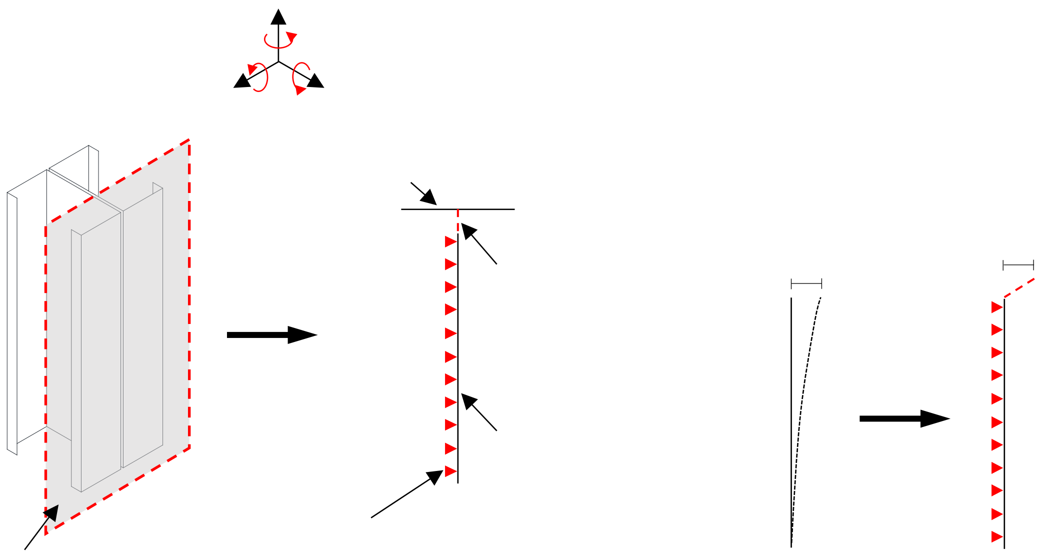

Figure 67. Simplified FE method of modelling stud

In this model, all deformations and capacities of the stud are represented by the connector element at the stud end, except for the displacement in the d_z direction caused by axial force. Hence, stud displacements in the d_x and d_y directions are restrained, as indicated by red triangles in Figure 67(a), while the displacement in d_z direction is allowed. The deformations of studs in all directions, except d_z, are modelled using the Cartesian and Rotation connector element. The function of connector element is illustrated in Figure 67(b), where the deformation of the stud in any specific direction, d_{st}, is modelled by the deformation of connector element in the same direction. Since the displacement of the stud in the d_z direction is captured by the beam element itself, infinite stiffness is assigned to the connector element in the d_z direction. This configuration allows that the joist or ledger moves consistently with the stud displacement in the d_z direction.

Plasterboards and shear walls provide appreciable restraints to the stud in the d_x, r_y and r_z directions (Vy and Mahendran, 2022). Thus, it is reasonable to neglect deformations in these directions by assigning infinite stiffnesses to the connector elements for those degrees of freedom. In contrast, the effects of plasterboards and shear walls in d_y and r_x directions are finite (Vy and Mahendran, 2022), and their influence is neglected to simplify the modelling method. Both deformations can be captured by the elastic deformation of the stud in its major axis direction (d_y). Therefore, infinite stiffness is applied to the r_x direction of the connector element, while the stiffness value of k_{stud} is assigned to the d_y direction. The stiffness k_{stud}, representing the elastic deformation of the stud in its major axis, is calculated as follows, assuming two fixed ends due to the strong stud-to-track connections:

$$k_{\text{stud}} = \frac{12EI}{L^3} \tag{63}$$

in which E is the Young's modulus = 200000 MPa (2018); I is the moment of inertia of major axis of stud; and L is the length of the stud.

Since the restraints on studs eliminate flexural and torsional buckling, and the beam element cannot capture local or distortional buckling or the combination thereof, the ultimate capacity of the stud is also modelled using the connector element. The design axial force capacity N^* is applied to the d_z direction, with value provided in Appendix. In summary, for the connector element, infinite stiffness is assigned to the connector element in the r_x, r_y, r_z, d_x and d_z directions, the ultimate capacity of N^* is set in the d_z direction, and the stiffness of k_{stud} is applied in the d_y direction.

FE analysis results of all four cases

Cases 1 and 2

The nomenclatures of studs in Cases 1 and 2 are shown in Figure 68. The vertical displacement at the location of "Displacement", marked in Figure 68, is shown in Figure 69(a, c).

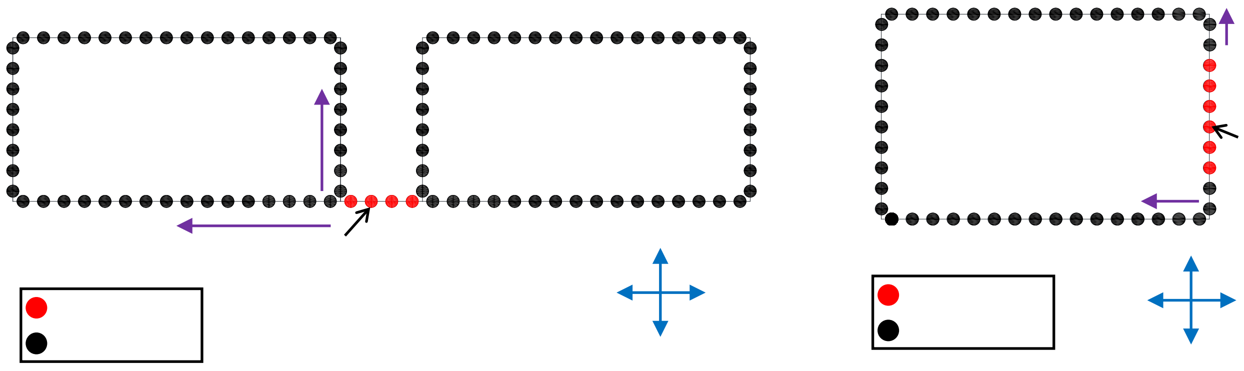

Figure 68. Nomenclature of studs in Cases 1 and 2

The load redistribution can be expressed by the axial forces in the studs surrounding the removed ones, as shown in Figure 69(b,d). The axial forces of studs changed abruptly when the time is 1 s due to the failure of stud walls and then stabilised after a period of oscillation. For both cases, the first stud adjacent to the removed ones shows the maximum increase in axial forces, which are 15.6 kN and 16.2 kN for studs C1SL1 and C2SL1, respectively.

The effects of the removed studs on the stud wall perpendicular to the removed ones are shown in Figure 70, where the overall influence is minimal. It is observed that the second stud adjacent to the removed one experiences minimal change in axial force. This indicates that most of the load carried by the removed stud is transferred directly to its nearest adjacent stud.

The component-action of archetype building is classified as force-controlled, as the cold-formed steel used shows a brittle behaviour. Therefore, the axial force of the critical stud is used to define the dynamic increase factor (DIF). The dynamic affected area is defined as the deformed joists adjacent to the removed stud or wall. Following the general procedures for defining DIF (Possidente et al., 2024), DIFs of 1.63 and 1.77 is calculated for Cases 1 and 2, respectively.

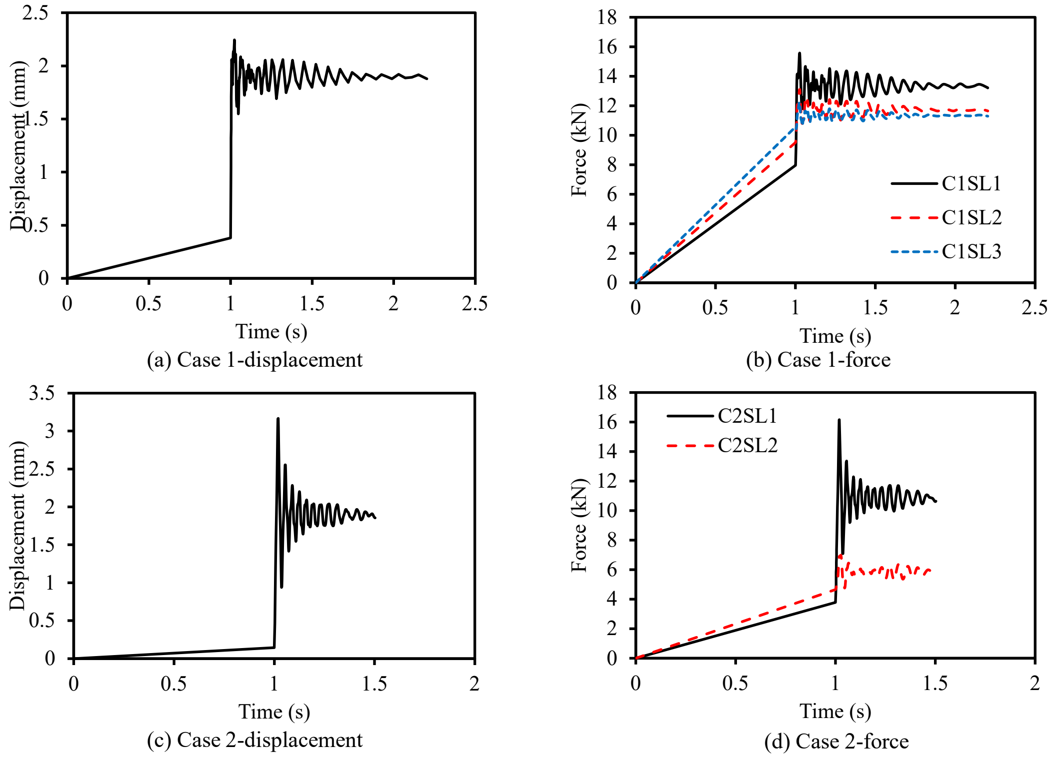

Figure 69. Vertical displacements of the location of "Displacement" and load for Cases 1 and 2

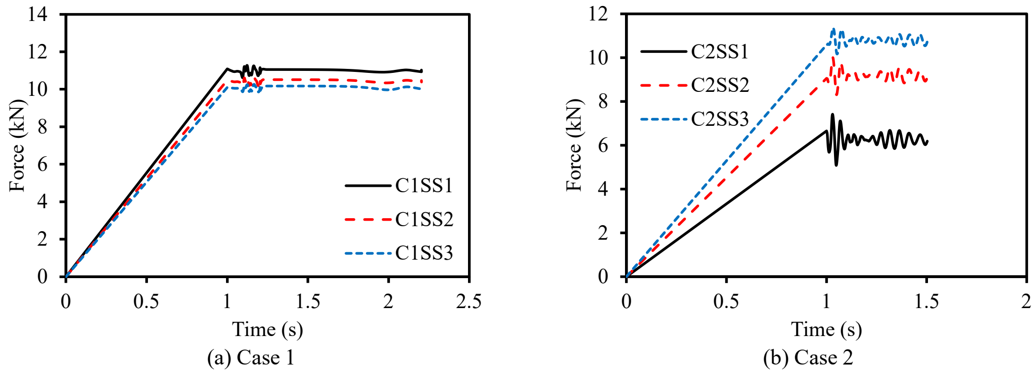

Figure 70. Forces of studs perpendicular to the removed ones for Cases 1 and 2

Case 3

The nomenclature of studs in Case 3 are shown in Figure 71. The vertical displacement at the location of "Displacement", marked in Figure 71, is shown in Figure 72(a).

The load redistribution can be expressed by the axial forces in the studs surrounding the removed ones, as shown in Figure 72(b, c, d). The axial forces of studs changed abruptly when the time is 1 s due to the failure of stud walls and then stabilised after a period of oscillation. On both west and east directions, the first studs adjacent to the removed ones (C3W11W1 and C3W11E1) shows the maximum increase in axial forces, whose maximum forces are 52.8 kN and 52.7 kN, respectively.

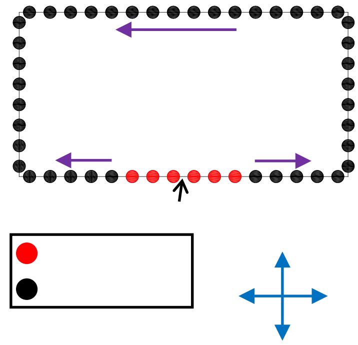

Figure 71. Nomenclature of studs in Case 3

Figure 72(d) shows the force in the stud wall on the opposite side of the joist adjacent to the removed stud. All studs show a similar response, with a force increase of 2.8 kN, which is sufficiently small to be considered negligible. This indicates that the load originally carried by the removed stud is primarily redistributed to the stud directly adjacent to it.

The component-action of archetype building is classified as force-controlled, and hence, a DIF of 1.81 is calculated for Case 3.

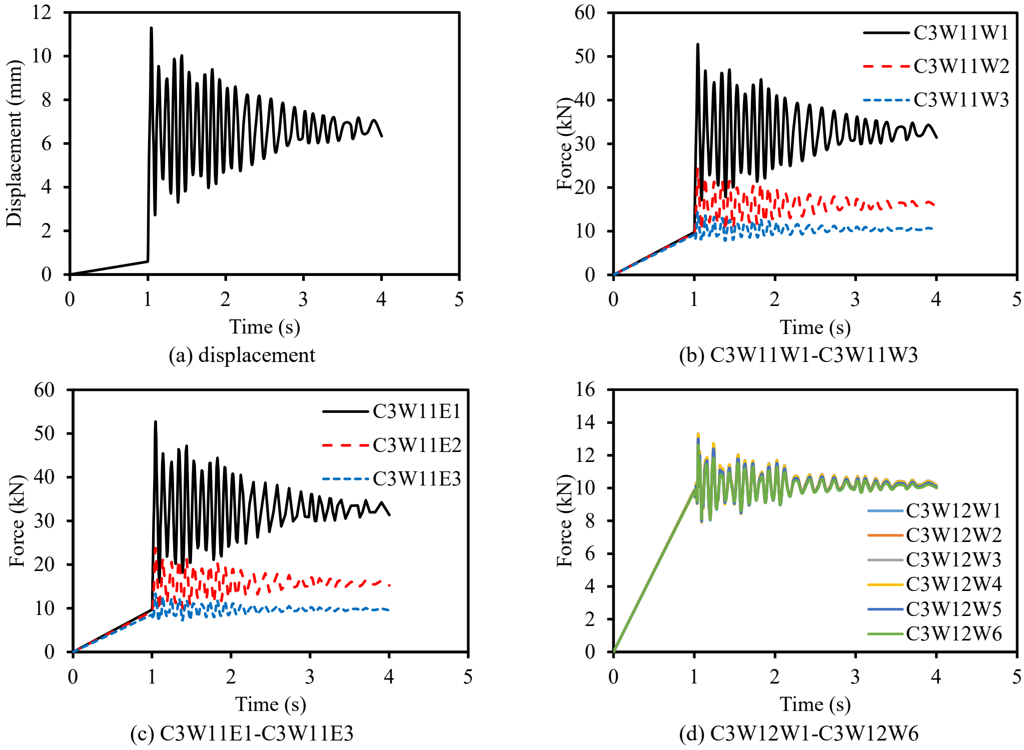

Figure 72. Forces of studs in Case 3

Case 4

The nomenclature of studs in Case 4 are shown in Figure 73. The vertical displacement at the location of “Displacement”, marked in Figure 73, is shown in Figure 74(a). The vertical displacement continuously increases due to the progressive failure of all studs surrounding the removed studs. To investigate the load redistribution, the capacity of the affected studs was assumed to be infinite, resulting in the oscillatory behaviour of the building shown in Figure 74(b).

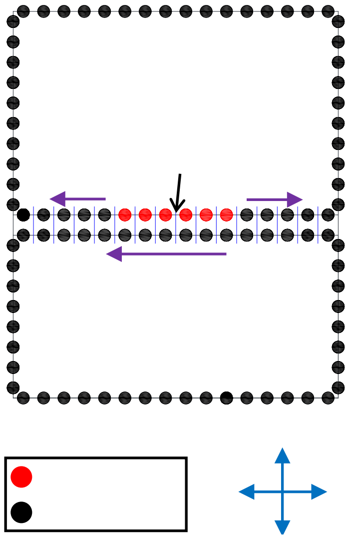

Figure 73. Nomenclature of studs in Case 4

The load redistribution in the case of infinite stud capacity is shown by the axial forces in the studs surrounding the removed ones (C4W3W1-C4W3W3 and C4W3E1-C4W3E3), as shown in Figure 75(a, b). The axial forces in studs C4W3W1 and C4W3E1 increase significantly, reaching maximum values of 65.2 kN and 65.1 kN, respectively. These forces exceed the design capacity of the studs (59.8 kN), leading to failure propagation throughout the entire building. Consistent with the other three cases, the load is primarily redistributed to the studs directly adjacent to the removed ones, as indicated by the relatively smaller increases of 18.0 kN and 5.9 kN in C4W3E2 and C4W3E3, respectively. Moreover, Figure 75(c) shows that the two walls in the double-wall system function independently, as evidenced by the unaffected axial forces in the studs of wall (C4W2W1-C3W2W6) after the time of 1 s.

The component-action of archetype building is classified as force-controlled, and hence, a DIF of 1.80 is calculated for Case 4.

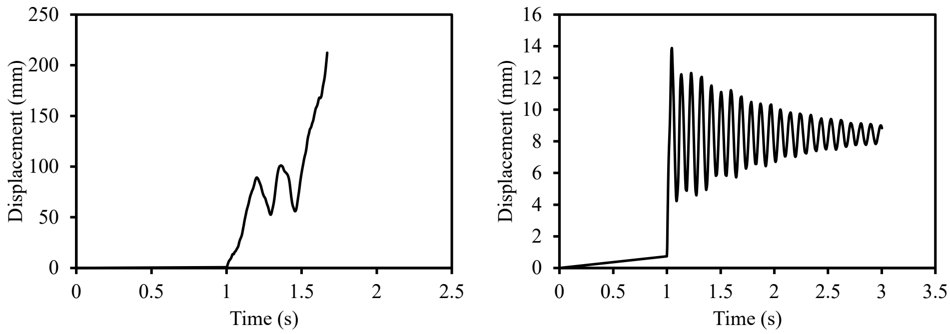

(a) limit capacity of stud (b) infinity capacity of stud

Figure 74. Vertical displacements of the location of "Displacement" for Case 4

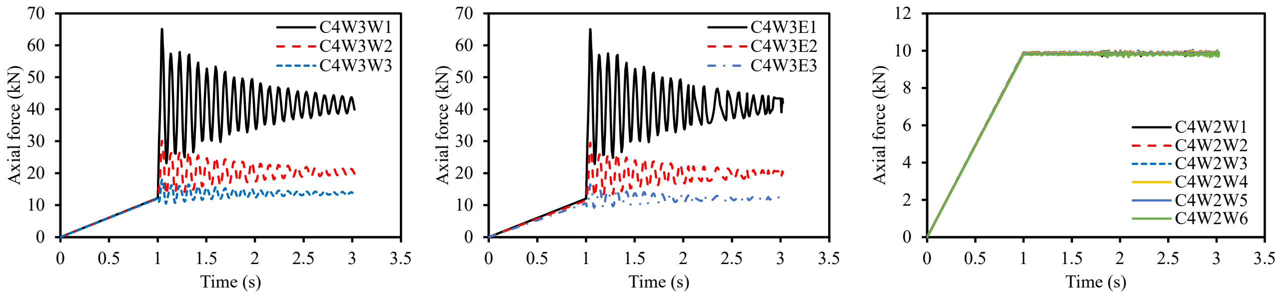

(a) axial forces in C4W3W1-C4W3W3 (b) axial forces in C4W3E1-C4W3E3 (c) axial forces in C4W2W1-C4W2W6

Figure 75. Force of studs for Case 4

C.3 FE analysis method for floor and plasterboard

Figure 76(a) shows the FE model with REDtongue as flooring. The Young's modulus and yield stress of floor are defined as 3000 MPa and 21 MPa, respectively. Each yellow dot represents the location of screw. The response of screw under tension and shear is modelled by the method provided in Zhou et al. (2025a).

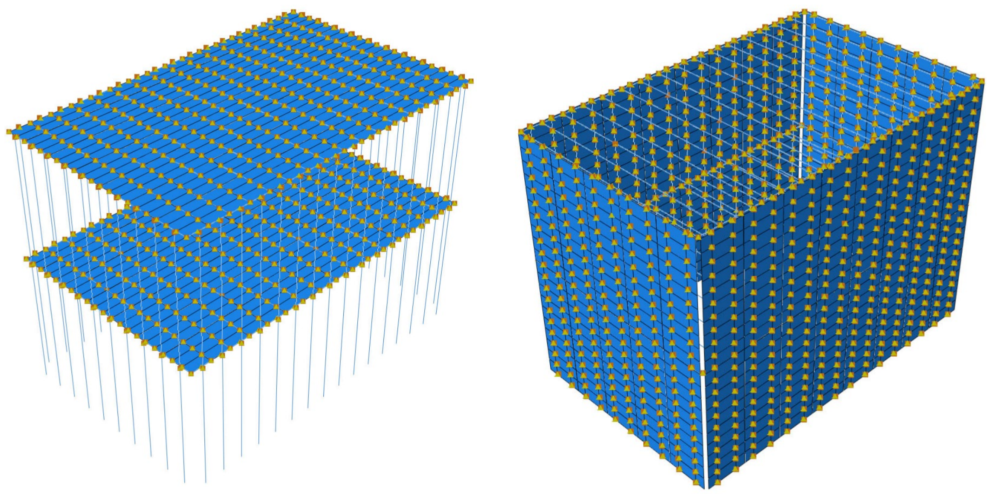

(a) floor (b) plasterboard

Figure 76. FE models with floor and plasterboard

Figure 76(b) shows the finite element (FE) model with a 32 mm plasterboard. The Young's modulus and yield stress of the floor are set as 1750 MPa and 2.25 MPa, respectively (Cramer et al., 2003). Due to the brittle behaviour of plasterboard, bearing failure commonly occurs, as shown in Figure 77(a) (Abeysiriwardena et al., 2021). The nonlinear behaviour of screws under bearing loads is documented by Abeysiriwardena et al. (2021) and depicted in Figure 77(b). To simplify the analysis, a bilinear curve, shown by the black line in Figure 77(b), is used. Similar to the FE model of the floor, each yellow dot represents the location of a screw.

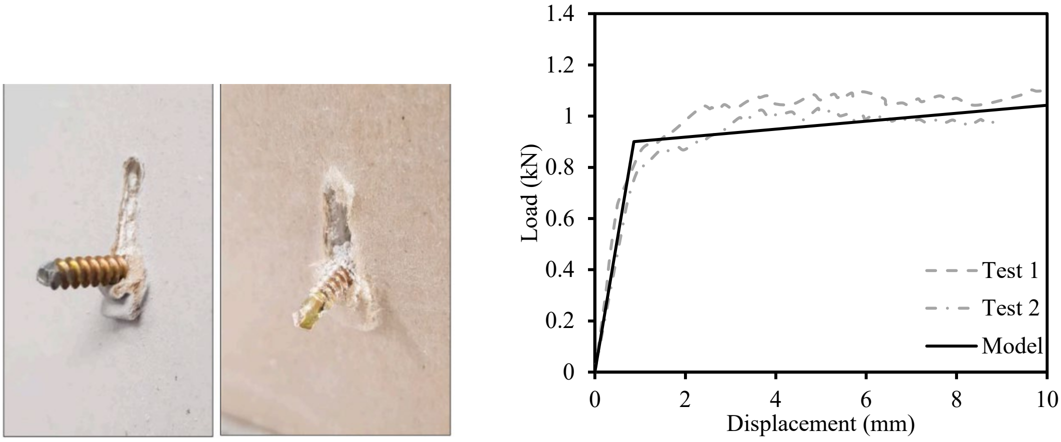

(a) bearing behaviour (Abeysiriwardena et al., 2021)　　(b) bearing response (Abeysiriwardena et al., 2021)

Figure 77. Bearing behaviour of screws in plasterboard

info@building40crc.org
www.building4pointzero.org
/building-4-0-crc